

**ENERGY STORAGE USING SODIUM-ION  
BATTERIES**

**ASHISH RUDOLA**  
*(B.Eng. (Hons.), NUS)*

**A THESIS SUBMITTED  
FOR THE DEGREE OF DOCTOR OF PHILOSOPHY  
DEPARTMENT OF MECHANICAL ENGINEERING  
NATIONAL UNIVERSITY OF SINGAPORE**

**2015**

***“Necessity is the mother of invention”***


***- Unknown***

## **Declaration**

I hereby declare that the entire work described in this thesis was undertaken while I was a Ph.D. student at the Department of Mechanical Engineering, National University of Singapore under the supervision of Associate Professor Palani Balaya.

Any results mentioned in this thesis which were not my own have been duly cited.

I also declare that all the experiments and results described herein are my own and this thesis has not been previously submitted for any degree at this or any other university in the world.

 29/07/2015  
**Ashish Rudola**

## **Acknowledgements**

First and foremost, I am extremely grateful to my supervisor, Assoc. Prof. Palani Balaya, for giving me the valuable opportunity to carry out research in his laboratory. He has always given me complete freedom to conduct research, yet also cautioning me when I strayed too far off-topic. His guidance has, hence, resulted in sound direction for my research, something which is crucial in the very new field of sodium-ion batteries where all research avenues are still relatively unexplored, enabling me to complete this thesis. I would also like to thank him for his support towards enhancing my research experience by encouraging me to travel for conferences, initiating collaborations with other research groups worldwide and for recommending me for the prestigious NUS President's Graduate Fellowship.

I would like to express my heartfelt gratitude to the Department of Mechanical Engineering for accepting me as a Ph.D. student and providing me with the NUS Research Studentship and the NUS Research Scholarship and nominating me for the NUS President's Graduate Fellowship at different stages of my Ph.D. Having studied as an undergraduate in this Department as well, I have spent eight fruitful years here which will always be treasured. I would like to thank all the ME Professors under whom I have studied countless modules over the years. Finally, I would like to thank Ms. Teo Lay Tin Sharen and Ms. Thong Siew Fah for helping me deal with all the administrative matters in the course of my Ph.D. degree.

I would like to acknowledge the important role of my mentor, Dr. Saravanan Kuppan, who provided me with the working knowledge and his immense practical research experience in batteries in my first two years of Ph.D. His mentorship enabled me to start research in sodium-ion batteries straightaway after starting my Ph.D degree, even though I had no prior research experience in these batteries before my Ph.D. My special thanks also go to Dr. Sappani Devaraj for very useful discussions on

electrochemistry, the kind that would not be readily found in books, to Dr. Satyanarayana Reddy Gajjela for his sound advice about Ph.D. life in general and also on synthesis of titanates, Dr. Srirama Hariharan for his patient advice and ever-ready willingness to have a discussion, Dr. Mangayarkarasi Nagarathinam for putting up with many random chemistry related questions and giving thought-provoking answers often at the expense of her own time, to Dr. Sunil Kumar for helping me understand the basics of SAED and HRTEM and to Dr. D.H. Nagaraju who mentored me briefly during my first two months of Ph.D. and introduced me to the general world of alkali-ion batteries. I would like to thank my group members- Dr. Vishwanathan Ramar, Mr. Markas Law Lee Lam, Dr. Rajesh Desapogu, Mr. Manikandan Balasundaram and Mr. Wang Chen- for making the lab a pleasant place to conduct research. My sincere gratitude goes to the following previous group members who always helped me whenever I approached them: Mr. Chad W. Mason, Mr. Girish Salian, Dr. Wong Kim Hai, and Dr. Lee Hwang Sheng. I would also like to thank the undergraduate/intern students whom I mentored- Mr. Fillarry T. Susanto, Ms. Maude Hoffmann, Mr. Chew Bo Wei Dominic, Mr. Ahmad “Ace” Haidrey, Mr. Rathin Bector, Mr. Sergio Hidalgo and Mr. Akshay Srivastava- for their willingness to learn and conduct experiments and to the following former intern/undergraduate students who were always very cooperative: Mr. Phang Qiuyuan Eugene, Mr. Huang Zhi Xiang, Mr. Chiam Fu Song, Mr. Loo Hong Zhi, Mr. Ong Jin Yuan Malcolm, Mr. Clement Kwok and Mr. Liu Bin.

My Ph.D. research experience was made enjoyable by many helpful laboratory technologists. In particular, I would like to express my deep appreciation to Mr. Chew Yew Lin, Mr. Yeo Khee Ho and Mrs. Hung-Ang Yan Len for always keeping order in the labs and processing payments for all chemicals/components I had to order, to Ms. Roslina Bte Abdullah for her support in case anything goes wrong in the office space, to Ms. Tan Tse Ying Zing and Mdm. Leng Lee Eng in Chemistry for promptly

conducting the TGA/DSC experiments, to Mdm Teng Jar Pang in Physics for accommodating last minute requests to conduct XRD during the summer of 2013 and to Mdm. Toh Soh Lian in Chemistry for help in running some XRD experiments. I would also like to thank Dr. Zhang Jixuan for performing the TEM measurements on my samples and being patient till I was satisfied with the quality of the pictures and to Dr. Yuan Ze Liang for conducting the XPS measurements.

It is important to maintain focus throughout the candidature length of a Ph.D. I have no doubt that my research quality would have suffered had I not been concurrently training in the martial arts of Muay Thai and Brazilian Jiu-Jitsu (BJJ) at Evolve MMA in Singapore. By giving me alternate goals to focus on and by helping me completely forget about my research struggles, the training sessions would never fail to re-energize me and give me fresh impetus to think from different perspectives. I would like to sincerely thank all the World Champion instructors at Evolve MMA for teaching me various techniques and making the training sessions fun. In particular, I would like to thank Kru Attachai Fairtex (“Kru Att”) for providing me my first taste of Muay Thai, to Kru Orono Wor Petchpool (“Kru No”), Kru Namsaknoi Yudthagarngamtorn (“Kru Must”), Kru Nonthachai Sit O (“Kru Non”) and Kru Att for being my constant Muay Thai instructors for the past three years, to Professor Takeo Draculino Tani for getting me interested in BJJ and to Professor Bruno (“Puccibull”) Pucci for keeping it real during the BJJ training over the past two years. Finally, huge thanks you to all my training partners for countless injuries, chokes and fun sparring sessions over the past few years.

Apart from training, it is important for me to look after my nutrition so as to work as efficiently as possible during lab hours. In this regard, I would like to thank my usual eating joints in NUS over the past few years- the Indian and Western food stall at Business canteen, the Japanese, Indian and Vegetarian food stalls at Engineering canteen- for consistently cooking the food that I like to eat. Special thanks to Mr.

Krishan Bisht at Food on Fire who would provide me wraps late at night after trainings, often refusing to take any money, when all restaurants would stop serving food and to Good News Café at Engineering for being the source of my coffee needs.

I would like to thank all my friends for their incredible support throughout my entire Ph.D. Without their amusing and entertaining company, these past four years would have been extremely difficult. In particular, I would like to thank Mr. Jordan “the familyman” Tee for guiding me in my undergraduate thesis presentation which gave me the confidence and self belief to pursue my passion, to Mr. 15 “Michael Loh” 05 for always reminding me how important mathematics is, to Ms. Nithya Ramesh for introducing me to new food places and for her forever mature advice, to Mr. Siddhesh Narayanan and Mr. Gopal Kumar for all the adventurous adventures and to Mr. Rahul Reddy, Mr. Anshul Bhushan and Ms. Saiher Malhotra for making my trips to New Delhi always enjoyable. I would like to thank Mr. Mrinal Jagirdar, Mr. Vivek Prem and Mr. Yannick Ng for being friendly companions throughout our Ph.D. journeys. I would also like to acknowledge the important role of Captain Planet and the Planeteers in getting me interested in the need for action against climate change at a very young age; had this exposure not been there, I may not have chosen to pursue research in the field of renewable energy. Finally, I would like to thank all my cousins and relatives for their never-ending support.

Lastly, and most importantly, I would like to thank my loving family for always keeping my best interests at heart and putting my needs first over theirs. I would definitely not have been able to complete my Ph.D. without their support. My father, Mr. Devendra Kumar Rudola and my mother, Mrs. Sunanda Rudola, have always given me immense motivation and advice throughout my life, especially during the tough times. Special thanks are also reserved for my overachieving sister, Ms. Richa Rudola, for always overshadowing me throughout life which gave me the drive I needed to pursue and finish my Ph.D.

# Table of Contents

Declaration.....	iii
Acknowledgements.....	iv
Table of Contents.....	viii
Executive Summary.....	xiii
Research Highlights of this Thesis.....	xv
List of Tables.....	xvii
List of Figures.....	xviii
List of Abbreviations.....	xxi
List of Publications/Patents/Presentations.....	xxiii
Copyright Permission.....	xxvi

## Chapter 1 | Introduction and Literature Review.....1

1.1 Preface to Chapter 1.....	2
1.2 Introduction.....	3
1.3 Working Knowledge of NIBs.....	6
1.3.1 Principle of Operation.....	6
1.3.2 Factors Determining the Voltage of a NIB.....	7
1.3.2.1 Nernst Equation.....	7
1.3.2.2 Gibbs Phase Rule.....	8
1.3.2.3 Polarization.....	9
1.3.3 Performance Metrics of a NIB.....	10
1.3.3.1 Specific Capacity.....	10
1.3.3.2 Specific Energy Density.....	11
1.3.3.3 Round Trip Energy Efficiency (RTEE).....	11
1.3.3.4 Definition of C rate and Rate Performance.....	12



1.3.4 Half Cell Evaluation of Cathode/Anode.....	12
1.3.5 Types of Sodium Storage Mechanisms.....	13
1.3.5.1 Insertion Reaction Mechanism.....	13
1.3.5.2 Conversion Reaction Mechanism.....	14
1.3.5.3 Alloy Reaction Mechanism.....	14
1.4 Literature Review on NIB Research.....	15
1.4.1 Half Cell Results of NIB Cathodes and Anodes.....	15
1.4.2 The Solid Electrolyte Interphase in NIBs.....	17
1.4.3 Current State-of-the-Art Full Cell Results.....	18
1.5 Objective of the Thesis’s Research.....	19
1.6 Structure of the Thesis.....	19

**Chapter 2 | Na<sub>2</sub>Ti<sub>6</sub>O<sub>13</sub>: a Potential Anode for Frequency Regulation Grid Storage Sodium-ion Batteries.....21**

2.1 Preface to Chapter 2.....	22
2.2 Introduction.....	23
2.3 Experimental Section.....	24
2.3.1 Synthesis.....	24
2.3.2 Synthesized Powder Characterization.....	24
2.3.3. Electrochemical Characterization.....	25
2.4 Results and Discussion.....	26
2.4.1 As-synthesized Powder Characterization.....	26
2.4.2 Sodium Storage Mechanism.....	29
2.4.3 Electrochemical Cycling Performance.....	31
2.4.4 Application to Full Cells.....	36
2.4.5 Stability of Sodiated Na <sub>2</sub> Ti <sub>6</sub> O <sub>13</sub> .....	37
2.5 Summary.....	38

## Chapter 3 | The $\text{Na}_2\text{Ti}_3\text{O}_7 \rightleftharpoons \text{Na}_4\text{Ti}_3\text{O}_7$ Sodium Storage Pathway.....41

3.1 Preface to Chapter 3.....	42
3.2 Introduction.....	43
3.3 Experimental Section.....	44
3.3.1 Synthesis.....	44
3.3.1.1 Solid-state Synthesis.....	44
3.3.1.2 Solvothermal Synthesis.....	45
3.3.2 Synthesized Powder Characterization.....	45
3.3.2.1 Solid-state Synthesized $\text{Na}_2\text{Ti}_3\text{O}_7$ .....	45
3.3.2.2 Solvothermal Synthesized $\text{Na}_2\text{Ti}_3\text{O}_7$ .....	46
3.3.3 Electrochemical Characterization.....	46
3.3.3.1 Solid-state Synthesized $\text{Na}_2\text{Ti}_3\text{O}_7$ .....	46
3.3.3.2 Solvothermal Synthesized $\text{Na}_2\text{Ti}_3\text{O}_7$ .....	47
3.4 Results and Discussion.....	48
3.4.1 Solid-state $\text{Na}_2\text{Ti}_3\text{O}_7$ Powder Characterization.....	48
3.4.2 Electrochemical Properties of Solid-state $\text{Na}_2\text{Ti}_3\text{O}_7$ .....	53
3.4.2.1 First Cycle Irreversibility.....	53
3.4.2.2 Long Term Cycling and Rate Performance.....	55
3.4.2.3 Effect of Ball-milling on Cycling Performance.....	57
3.4.2.4 Effect of Voltage Window on Cycling Performance.....	58
3.4.2.5 Study on Sodium Insertion and Extraction Kinetics.....	60
3.4.3 Solvothermal $\text{Na}_2\text{Ti}_3\text{O}_7$ Powder Characterization.....	62
3.4.4 Solvothermal $\text{Na}_2\text{Ti}_3\text{O}_7/\text{C}$ Cycling Performance.....	65
3.5 Summary.....	67

**Chapter 4 | Understanding the Role of the Sodium CE in Half Cell Evaluation in Sodium Batteries.....69**

4.1 Preface to Chapter 4.....	70
4.2 Introduction.....	71
4.3 Experimental Section.....	72
4.3.1 Synthesis.....	72
4.3.2 Synthesized Powder Characterization.....	72
4.3.3 Electrochemical Characterization.....	72
4.4 Results and Discussion.....	73
4.4.1 As-synthesized Powder Characterization.....	73
4.4.2 Reproduction of the Voltage Step Phenomenon.....	74
4.4.3 Three-electrode Cycling Studies.....	76
4.4.4 Impedance Studies.....	77
4.4.5 Voltage Step Phenomenon in Full Cells.....	79
4.4.6 High Polarization of the Sodium CE.....	80
4.5 Summary.....	82

**Chapter 5 | A 0.2 V Earth-abundant Sodium-ion Battery Anode: the Na<sub>2</sub>Ti<sub>3</sub>O<sub>7</sub> to Na<sub>3-x</sub>Ti<sub>3</sub>O<sub>7</sub> Sodium Storage Pathway.....85**

5.1 Preface to Chapter 5.....	86
5.2 Introduction.....	87
5.3 Experimental Section.....	88
5.3.1 Synthesis of Na <sub>3</sub> V <sub>2</sub> (PO <sub>4</sub> ) <sub>2</sub> F <sub>3</sub> /C.....	88
5.3.2 Electrochemical Characterization.....	88
5.3.3 <i>Ex-situ</i> XRD Characterization.....	91
5.4 Results and Discussion.....	91

5.4.1 $\text{Na}_2\text{Ti}_3\text{O}_7 \rightleftharpoons \text{Na}_{3-x}\text{Ti}_3\text{O}_7$ Sodium Storage Pathway.....	91
5.4.2 Understanding the $\text{Na}_2\text{Ti}_3\text{O}_7 \rightarrow \text{Na}_{3-x}\text{Ti}_3\text{O}_7 \rightarrow \text{Na}_4\text{Ti}_3\text{O}_7$ Transition.....	95
5.4.3 Safety of $\text{Na}_2\text{Ti}_3\text{O}_7 \rightleftharpoons \text{Na}_{3-x}\text{Ti}_3\text{O}_7$ Pathway.....	100
5.4.4 $\text{Na}_2\text{Ti}_3\text{O}_7 \rightleftharpoons \text{Na}_{3-x}\text{Ti}_3\text{O}_7$ Anode Application to NIBs.....	101
5.4.5 Potential of the $\text{Na}_2\text{Ti}_3\text{O}_7 \rightleftharpoons \text{Na}_{3-x}\text{Ti}_3\text{O}_7$ Pathway in Grid Storage NIBs.....	105
5.5 Summary.....	106

**Chapter 6 | Conclusions and Future Research Directions.....109**

6.1 Conclusions.....	110
6.2 Future Research Directions.....	114

**References.....117**

## Executive Summary

Energy storage is crucial for integrating intermittent renewable energy sources into the electricity grid. Lithium-ion batteries (LIBs) will be ill-suited for this application owing to scarce lithium resources. Sodium-ion batteries (NIBs), based on globally abundant sodium resources, would be ideal candidates for grid storage batteries. Over the past four years, some NIB cathodes have been reported with performance rivalling LIB cathodes. No suitable anode has been shown to exhibit all qualities expected of a grid storage battery electrode material. These are primarily low cost, followed by a high degree of safety, long cycle life (in excess of 4,000 cycles) and high efficiency. Energy density is a secondary factor. The objective of this thesis, hence, is to develop such NIB anodes.

The sodium storage performance of the earth-abundant sodium titanate family is explored in this thesis. In particular, the phases  $\text{Na}_2\text{Ti}_6\text{O}_{13}$  and  $\text{Na}_2\text{Ti}_3\text{O}_7$  were chosen.  $\text{Na}_2\text{Ti}_6\text{O}_{13}$ , synthesized in high yield by an inexpensive solution-based method, is shown to fulfill all requirements expected of a grid storage NIB anode: long cycle life (exceeding 5,000 cycles), high degree of safety (till 500 °C) and high efficiency. A 2.5 V NIB was fabricated with  $\text{Na}_2\text{Ti}_6\text{O}_{13}$  as proof-of-concept displaying very stable cycling. Its sodium storage mechanism is discussed to explain such good performance. While this material does not suffer from any drawbacks with grid storage batteries in mind, its storage capacity of 50 mAh/g can always be improved.

Sodium storage in  $\text{Na}_2\text{Ti}_3\text{O}_7$  was hence investigated. Solid-state synthesis of  $\text{Na}_2\text{Ti}_3\text{O}_7$ , resulting in micrometre sized particles, demonstrated theoretical capacity of 178 mAh/g (storing two moles of sodium per mole of  $\text{Na}_2\text{Ti}_3\text{O}_7$ ) at very low average voltage of 0.3 V vs Na/Na<sup>+</sup>. However, it displayed poor cycling stability as well as inadequate high rate performance. Kinetic studies revealed a relatively high sodium chemical diffusion coefficient for this material. To exploit this, a unique

solvothermal synthesis was employed to synthesize sub-micrometre  $\text{Na}_2\text{Ti}_3\text{O}_7$  particles embedded in a carbon matrix. This morphology resulted in excellent high rate performance up to 40 C (1.5 min response), though the cycling stability was not improved.

It was discovered that if  $\text{Na}_2\text{Ti}_3\text{O}_7$  is allowed to store  $\leq$  one mole of sodium (resulting in 89 mAh/g of capacity), the resulting  $\text{Na}_2\text{Ti}_3\text{O}_7 \rightleftharpoons \text{Na}_{3-x}\text{Ti}_3\text{O}_7$  sodium storage pathway displayed excellent efficiency, very fast response of 80 C (45 s), a long cycle life (1,500 cycles) and good stability until a safe temperature of 376 °C. More importantly, this pathway led to the lowest ever reported voltage for any non-carbon based NIB anode at 0.2 V vs Na/Na<sup>+</sup>. Its utilization in a full NIB in the coin cell format is shown to result in the highest voltage plateau (4.0 – 3.7 V) for any non-carbon based NIB reported thus far, with excellent stability, efficiency and rate performance. Hence, it is believed that this anode pathway may be a stellar choice resulting in high energy density grid storage NIBs.

In the course of sodium storage evaluation of these materials, some observations were made which furthered understanding of sodium batteries. It was found that sodium metal is a good reference electrode but not a good counter electrode. This is because it can exhibit extremely high polarization (as much as 0.2 V vs Na/Na<sup>+</sup>). Furthermore, depending on the electrolyte used, it may lead to a peculiar voltage step. These factors make data interpretation of the working electrode difficult in a two-electrode electrochemical experimental configuration. It is, hence, recommended that three-electrode cells be used to evaluate the sodium storage properties of electrode materials in NIB research.

## Research Highlights of this Thesis

The following are the most significant findings of this thesis:

1. The sodium storage performance of the anode  $\text{Na}_2\text{Ti}_6\text{O}_{13}$  has been thoroughly investigated for the first time through various techniques. An inexpensive and high yield water-ethanol based synthesis was devised which resulted in  $\text{Na}_2\text{Ti}_6\text{O}_{13}$  nanorods capable of demonstrating an outstanding cycle life of 5,000 cycles for the first time for sodium-ion battery anodes.
2. A new phenomenon in sodium batteries has been discovered which relates to a voltage step in the galvanostatic profiles of flat-potential electrode materials. This voltage step is actually not caused by the working electrode, but instead arises due to an increased polarization of the sodium metal serving as the counter electrode.
3. It was discovered that sodium metal may be a good reference electrode, but it is not a good counter electrode. Apart from the voltage step phenomenon, its polarization in general can be very high such that it does not operate close to  $0.0 \text{ V vs Na/Na}^+$  but could operate higher than  $0.2 \text{ V vs Na/Na}^+$ , depending on the  $C$  rate. The use of three-electrode cells for the evaluation of cathodes/anodes meant for sodium-ion batteries is highly encouraged. Such results seem to be unique to sodium batteries as corresponding processes have not been reported in lithium batteries.
4. For the first time, a completely new intermediate phase of  $\text{Na}_{3-x}\text{Ti}_3\text{O}_7$  has been discovered and isolated through galvanostatic cycling studies of the known anode  $\text{Na}_2\text{Ti}_3\text{O}_7$ . If this newly discovered  $\text{Na}_2\text{Ti}_3\text{O}_7 \rightleftharpoons \text{Na}_{3-x}\text{Ti}_3\text{O}_7$  pathway is allowed to operate as an anode, then this pathway results in the lowest voltage redox activity at  $0.2 \text{ V vs Na/Na}^+$  ever reported for any non-carbon based sodium-ion battery anode along with negligible polarization,

excellent high rate performance with response times of 45 s (80 C rate) and long cycle life of 1,500 cycles at 1 C rate.

5. The performance of the  $\text{Na}_2\text{Ti}_3\text{O}_7 \rightleftharpoons \text{Na}_{3-x}\text{Ti}_3\text{O}_7$  pathway in a full sodium-ion cell coupled with the high voltage cathode  $\text{Na}_3\text{V}_2(\text{PO}_4)_2\text{F}_3$  was found to be extremely stable highlighted by the highest voltage plateau for any non-carbon based sodium-ion battery ever reported between 4.0 – 3.7 V resulting in high energy density.



## List of Tables

<b>Table 2.1</b>   Phase purity of the as-prepared $\text{Na}_2\text{Ti}_6\text{O}_{13}$ samples for different molar ratio of the Na and Ti sources, as determined from Rietveld refinement of PXRD data.....	27
<b>Table 2.2</b>   Lattice parameters obtained for the as-prepared $\text{Na}_2\text{Ti}_6\text{O}_{13}$ samples, as determined from Rietveld refinement.....	27
<b>Table 2.3</b>   Refined crystallographic data for the as-prepared $\text{Na}_2\text{Ti}_6\text{O}_{13}$ samples, as determined from Rietveld refinement.....	28
<b>Table 2.4</b>   Refined crystallographic data for the rutile $\text{TiO}_2$ impurity in the as-prepared $\text{Na}_2\text{Ti}_6\text{O}_{13}$ samples, as determined from Rietveld refinement.....	28
<b>Table 3.1</b>   Rietveld refinement parameters for $\text{Na}_2\text{Ti}_3\text{O}_7$ calcined at 750 °C for 20 h.....	49
<b>Table 3.2</b>   XPS results for the as-synthesized $\text{Na}_2\text{Ti}_3\text{O}_7$ powder.....	52

# List of Figures

## Chapter 1 | Introduction and Literature Review

**Figure 1.1** | Illustration of how energy storage can help in load levelling operations for the grid.....5

**Figure 1.2** | Schematic illustration of the operation mechanism within a sodium-ion battery.....7

## Chapter 2 | Na<sub>2</sub>Ti<sub>6</sub>O<sub>13</sub>: a Potential Anode for Frequency Regulation Grid Storage Sodium-ion Batteries

**Figure 2.1** | Crystal structure of Na<sub>2</sub>Ti<sub>6</sub>O<sub>13</sub> when viewed along the *b*-axis.....23

**Figure 2.2** | Evaluation of the phase purity of the as-prepared Na<sub>2</sub>Ti<sub>6</sub>O<sub>13</sub> from the soft-template method.....26

**Figure 2.3** | Morphology characterization of the as-prepared Na<sub>2</sub>Ti<sub>6</sub>O<sub>13</sub> from the soft-template method.....28

**Figure 2.4** | Evaluation of Na<sub>2</sub>Ti<sub>6</sub>O<sub>13</sub> nanorod by TEM analysis.....29

**Figure 2.5** | Evaluation of sodium storage mechanism of Na<sub>2</sub>Ti<sub>6</sub>O<sub>13</sub>.....30

**Figure 2.6** | Effect on lattice parameters of Na<sub>2</sub>Ti<sub>6</sub>O<sub>13</sub> by sodium incorporation as evaluated from *ex-situ* XRD data.....31

**Figure 2.7** | Cycling performance of pure Na<sub>2</sub>Ti<sub>6</sub>O<sub>13</sub> electrode.....32

**Figure 2.8** | Cycling performance of Na<sub>2</sub>Ti<sub>6</sub>O<sub>13</sub>/CB composite electrode.....34

**Figure 2.9** | Cycling performance of Na<sub>2</sub>Ti<sub>6</sub>O<sub>13</sub>/graphite composite electrode.....35

**Figure 2.10** | Long term cycling of Na<sub>2</sub>Ti<sub>6</sub>O<sub>13</sub> with conductive additives at a fast 20 C (3 min charge/discharge) rate.....36

**Figure 2.11** | Illustration of Na<sub>2</sub>Ti<sub>6</sub>O<sub>13</sub> being used as anode in a full NIB.....37

**Figure 2.12** | Stability of sodiated Na<sub>2</sub>Ti<sub>6</sub>O<sub>13</sub>.....38

## Chapter 3 | The Na<sub>2</sub>Ti<sub>3</sub>O<sub>7</sub> ⇌ Na<sub>4</sub>Ti<sub>3</sub>O<sub>7</sub> Sodium Storage Pathway

**Figure 3.1** | Crystal structure of Na<sub>2</sub>Ti<sub>3</sub>O<sub>7</sub> when viewed along the *b*-axis demonstrating its layered structure.....43

<b>Figure 3.2</b>   Comparison of PXRD patterns with different calcination temperatures and times using NaOH and anatase-TiO <sub>2</sub> as precursors.....	48
<b>Figure 3.3</b>   Rietveld Refinement of the PXRD Data for the Na <sub>2</sub> Ti <sub>3</sub> O <sub>7</sub> sample sintered at 750 °C for 20 h.....	49
<b>Figure 3.4</b>   PXRD patterns obtained for the CH <sub>3</sub> COONa precursor at different calcination temperatures and times.....	50
<b>Figure 3.5</b>   FESEM images of Na <sub>2</sub> Ti <sub>3</sub> O <sub>7</sub> calcined at 750 °C for 20 h.....	51
<b>Figure 3.6</b>   Morphology characterization of the as-prepared Na <sub>2</sub> Ti <sub>3</sub> O <sub>7</sub> from the solid-state method.....	51
<b>Figure 3.7</b>   High resolution spectra for Ti 2p of as-prepared Na <sub>2</sub> Ti <sub>3</sub> O <sub>7</sub> powder.....	52
<b>Figure 3.8</b>   FESEM examination along with elemental mapping (EDX) for the elements Na, Ti and O for the as-synthesized Na <sub>2</sub> Ti <sub>3</sub> O <sub>7</sub> .....	53
<b>Figure 3.9</b>   Investigation into the ICL during the first cycle of a Na <sub>2</sub> Ti <sub>3</sub> O <sub>7</sub> /CB composite electrode.....	55
<b>Figure 3.10</b>   Cycling of Na <sub>2</sub> Ti <sub>3</sub> O <sub>7</sub> electrode with 20% carbon black and 10% binder at 0.1 C rate showing charge-discharge curves for cycles 2, 25, 75 and 90 in the voltage window of 0.01 – 2.5 V.....	56
<b>Figure 3.11</b>   Long term cycling and rate performance of a Na <sub>2</sub> Ti <sub>3</sub> O <sub>7</sub> /CB composite electrode at various rates.....	57
<b>Figure 3.12</b>   Effect of ball-milling on cycling performance.....	57
<b>Figure 3.13</b>   Effect of ball-milling on reducing the active material particle size.....	58
<b>Figure 3.14</b>   Effect of voltage window on cycling profile and performance.....	59
<b>Figure 3.15</b>   Cyclic voltammetry curves illustrating the effect of voltage window...60	60
<b>Figure 3.16</b>   Evaluation of the sodium storage kinetics using cyclic voltammetry...61	61
<b>Figure 3.17</b>   Evaluation of the sodium chemical diffusion coefficient during the insertion of Na <sup>+</sup> ions into Na <sub>2</sub> Ti <sub>3</sub> O <sub>7</sub> using GITT.....	62
<b>Figure 3.18</b>   Na <sub>2</sub> Ti <sub>3</sub> O <sub>7</sub> /C powder characterization through XRD and TGA.....	63
<b>Figure 3.19</b>   Na <sub>2</sub> Ti <sub>3</sub> O <sub>7</sub> /C powder's morphology characterization.....	64
<b>Figure 3.20</b>   Na <sub>2</sub> Ti <sub>3</sub> O <sub>7</sub> /C powder's surface area and pore size characterization.....	64
<b>Figure 3.21</b>   Cycling performance of Na <sub>2</sub> Ti <sub>3</sub> O <sub>7</sub> /C prepared by the solvothermal synthesis.....	66

## Chapter 4 | Understanding the Role of the Sodium CE in Half Cell Evaluation in Sodium Batteries

<b>Figure 4.1</b>   Material characterization of the as-prepared NTP.....	74
<b>Figure 4.2</b>   Reproduction of the voltage step phenomenon in NTP.....	75
<b>Figure 4.3</b>   Three-electrode cycling of NTP to understand the cause of the voltage step phenomenon.....	76
<b>Figure 4.4</b>   EIS studies on uncycled cells.....	77
<b>Figure 4.5</b>   EIS studies while cycling along with implications of the voltage step on full NIBs.....	78
<b>Figure 4.6</b>   Illustration of the increase in Na CE's polarization during galvanostatic cycling at different C rates in alkyl carbonate solvents based solutions.....	81
<b>Figure 4.7</b>   Illustration of the possibility of erroneous data interpretation in sodium half cells of low voltage NIB anodes caused by increased Na CE's polarization.....	82

## Chapter 5 | A 0.2 V Earth-abundant Sodium-ion Battery Anode: the $\text{Na}_2\text{Ti}_3\text{O}_7$ to $\text{Na}_{3-x}\text{Ti}_3\text{O}_7$ Sodium Storage Pathway

<b>Figure 5.1</b>   Illustration of the $\text{Na}_2\text{Ti}_3\text{O}_7 \rightleftharpoons \text{Na}_{3-x}\text{Ti}_3\text{O}_7$ pathway. ....	92
<b>Figure 5.2</b>   Long term cycling of the $\text{Na}_2\text{Ti}_3\text{O}_7 \rightleftharpoons \text{Na}_{3-x}\text{Ti}_3\text{O}_7$ pathway in a sodium half cell over 1,500 cycles between 0.10 – 2.5 V.....	94
<b>Figure 5.3</b>   Rate performance of the $\text{Na}_2\text{Ti}_3\text{O}_7 \rightleftharpoons \text{Na}_{3-x}\text{Ti}_3\text{O}_7$ pathway in a sodium half cell from C/5 to 80 C.....	95
<b>Figure 5.4</b>   EIS analysis into the cause for the significant difference in polarization witnessed in the two pathways of sodium storage in $\text{Na}_2\text{Ti}_3\text{O}_7/\text{C}$ .....	97
<b>Figure 5.5</b>   Structural changes occurring during the $\text{Na}_2\text{Ti}_3\text{O}_7 \rightarrow \text{Na}_{3-x}\text{Ti}_3\text{O}_7 \rightarrow \text{Na}_4\text{Ti}_3\text{O}_7$ transition.....	98
<b>Figure 5.6</b>   Illustration of the high degree of safety exhibited by the $\text{Na}_2\text{Ti}_3\text{O}_7 \rightleftharpoons \text{Na}_{3-x}\text{Ti}_3\text{O}_7$ sodium storage pathway.....	101
<b>Figure 5.7</b>   Sodium storage performance of $\text{Na}_3\text{V}_2(\text{PO}_4)_2\text{F}_3/\text{C}$ cathode in a sodium half cell.....	101
<b>Figure 5.8</b>   Sodium storage performance of a full cell employing the $\text{Na}_2\text{Ti}_3\text{O}_7 \rightleftharpoons \text{Na}_{3-x}\text{Ti}_3\text{O}_7$ sodium storage pathway in a three- electrode cell.....	102
<b>Figure 5.9</b>   Calculated Ragone plot if the $\text{Na}_2\text{Ti}_3\text{O}_7 \rightleftharpoons \text{Na}_{3-x}\text{Ti}_3\text{O}_7$ pathway were to be paired with the $\text{Na}_2\text{Fe}_2(\text{SO}_4)_3$ cathode in a full NIB.....	104
<b>Figure 5.10</b>   Comparison of the first cycle coulombic efficiency ( $\text{CE}_{\text{ff}}$ ) with different binders (CMC or PVDF).....	105

## List of Abbreviations

BET	: Brunauer-Emmett-Teller
BJH	: Barrett-Joyner-Halenda
CB	: Carbon black
CE	: Counter electrode
CE <sub>ff</sub>	: Coulombic efficiency
CMC	: Sodium salt of carboxymethyl cellulose
CTAB	: Hexadecyl-trimethyl-ammonium bromide
CV	: Cyclic voltammetry
DSC	: Differential scanning calorimetry
EC	: Ethylene carbonate
EDX	: Energy-dispersive X-ray spectroscopy
EIS	: Electrochemical impedance spectroscopy
FESEM	: Field emission scanning electron microscopy
HRTEM	: High resolution transmission electron microscopy
LIB	: Lithium-ion battery
NIB	: Sodium-ion battery
NMP	: N-methyl pyrrolidone
NTP	: NaTi <sub>2</sub> (PO <sub>4</sub> ) <sub>3</sub>
NVP	: Na <sub>3</sub> V <sub>2</sub> (PO <sub>4</sub> ) <sub>3</sub>

NVPF :  $\text{Na}_3\text{V}_2(\text{PO}_4)_2\text{F}_3$

OCV : Open circuit voltage

PC : Propylene carbonate

PVDF : Polyvinylidene fluoride

PXRD : Powder X-ray diffraction

RE : Reference electrode

SAED : Selected area electron diffraction

SEI : Solid electrolyte interphase

TEM : Transmission electron microscopy

TGA : Thermogravimetric analysis

XPS : X-ray photoelectron spectroscopy

XRD : X-ray diffraction

WE : Working electrode

# List of Publications/Patents/Presentations

## Publications

1. Introducing a 0.2 V Sodium-ion Battery Anode: The  $\text{Na}_2\text{Ti}_3\text{O}_7$  to  $\text{Na}_{3-x}\text{Ti}_3\text{O}_7$  Pathway

**A. Rudola**, N. Sharma and P. Balaya

Electrochemistry Communications, 2015, 61, p10-13

DOI: 10.1016/j.elecom.2015.09.016

Impact Factor: 4.847

Number of Citations: 0

2. A New Phenomenon in Sodium Batteries: Voltage Step Due to Solvent Interaction

**A. Rudola**, D. Aurbach and P. Balaya

Electrochemistry Communications, 2014, 46, p56-59

DOI: 10.1016/j.elecom.2014.06.008

Impact Factor: 4.847

Number of Citations: 7

3.  $\text{Na}_2\text{Ti}_6\text{O}_{13}$ : A Potential Anode for Grid-Storage Sodium-ion Batteries

**A. Rudola**, K. Saravanan, D. Sappani, H. Gong, P. Balaya

Chemical Communications, 2013, 49, p7451-7453

DOI: 10.1039/C3CC44381G

Impact Factor: 6.834

Number of Citations: 38

4.  $\text{Na}_2\text{Ti}_3\text{O}_7$ : An intercalation based anode for sodium-ion battery application

**A. Rudola**, K. Saravanan, C. W. Mason, P. Balaya

Journal of Materials Chemistry A, 2013, 1, p2653-2662

DOI:10.1039/C2TA01057G

Impact Factor: 7.443

Number of Citations: 98

5. The first report on excellent cycling stability and superior rate capability of  $\text{Na}_3\text{V}_2(\text{PO}_4)_3$  for Sodium-ion batteries

K. Saravanan, C. W. Mason, **A. Rudola**, K. H. Wong, P. Balaya

Advanced Energy Materials, 2013, 3, 4, p444-450

DOI: 10.1002/aenm.201200803

Impact Factor: 16.146

Number of Citations: 116

**Total Number of Citation: 259**

## **Patents**

1. Formation of  $\text{Na}_3\text{Ti}_3\text{O}_7$  by Electrochemical, Chemical and Mechanical Means and its Application in Batteries, Electrochromic Windows, Water Splitting and Catalytic Reactions

P. Balaya and **A. Rudola**

US Provisional Application No.: 62/120,463

Date: 12/03/2015

## **Oral Presentations**

1.  $\text{Na}_2\text{Ti}_3\text{O}_7$ : An Attractive Anode for Sodium-ion Battery Application

**A. Rudola**, N. Sharma, H. Brand, J. Christian and P. Balaya, 8<sup>th</sup> *International Conference on Materials for Advanced Technologies (ICMAT 2015)*, Singapore, July 2015

2. Sodium Titanates as Viable Anode Material for Sodium-ion Battery Applications

**A. Rudola** and **P. Balaya**, 11<sup>th</sup> *International Conference on Ceramic Materials and Components for Energy and Environmental Applications (CMCEE 2015)*, Vancouver, Canada, June 2015



3. Sodium Titanate Anodes for Sodium-ion Battery Applications

**A. Rudola** and P. Balaya, *1<sup>st</sup> International Symposium on Engineering Science, Singapore, May 2015*

4. Optimization of Electrodes and Electrolytes for High Performance Sodium Batteries

P. Balaya, **A. Rudola** and M. Law, *55<sup>th</sup> Battery Symposium in Japan, Kyoto, Japan, November 2014*

## **Poster Presentations**

1. A New Phenomenon in Sodium Batteries: Voltage Step Due to Solvent Interaction

**A. Rudola** and P. Balaya, *39<sup>th</sup> International Conference and Expo on Advanced Ceramics and Composites (ICACC 2015), Daytona Beach, Florida, USA, January 2015.*

2. Na<sub>2</sub>Ti<sub>6</sub>O<sub>13</sub>: A Potential Anode for Grid-Storage Sodium-ion Batteries

**A. Rudola**, K. Saravanan, D. Sappani, H. Gong and P. Balaya, *7<sup>th</sup> International Conference on Materials for Advanced Technologies (ICMAT 2013), Singapore, July 2013.*

3. High Rate and Long Cycle Life of Na<sub>2</sub>Ti<sub>6</sub>O<sub>13</sub> in a Sodium Battery

**A. Rudola**, K. Saravanan, D. Sappani, H. Gong and P. Balaya, *Lithium Battery Discussions (LIBD 2013), Arcachon, France, June 2013.*

4. Na<sub>2</sub>Ti<sub>3</sub>O<sub>7</sub>: An intercalation based anode for sodium-ion battery application

**A. Rudola**, K. Saravanan, C.W. Mason and P. Balaya, *International Conference of Young Researchers on Advanced Materials (ICYRAM 2012), Singapore, July 2012.*

5. Na<sub>2</sub>Ti<sub>3</sub>O<sub>7</sub>: An intercalation based anode for sodium-ion battery application

**A. Rudola**, K. Saravanan, C.W. Mason and P. Balaya, *16<sup>th</sup> International Meeting on Lithium Batteries (IMLB 2012), Jeju, Korea, June 2012.*

## Copyright Permission

All figures used in this thesis have been originally created by me. Most figures have been published in various journals as indicated at the beginning of each chapter and hence, the copyright is held by their respective publishers: Royal Society of Chemistry (RSC) and Elsevier B.V. However, both these publishers have stated<sup>1, 2</sup> that it is permissible for authors to re-use the figures/entire manuscript text published in their journals if intended for inclusion in a thesis and that no written permission is actually required for this purpose as this is a retained right of an author publishing with these publishers. Hence, I would like to acknowledge the actual copyright of the various figures used in this thesis held by RSC and Elsevier B.V.

<sup>1</sup> <http://www.rsc.org/journals-books-databases/journal-authors-reviewers/licences-copyright-permissions/#reuse-permission-requests> (for RSC).

<sup>2</sup> <http://www.elsevier.com/about/company-information/policies/copyright/personal-use> (for Elsevier B.V.).

## **Chapter 1 | Introduction and Literature Review**

## **1.1 Preface to Chapter 1**

A concise background of the place of sodium-ion batteries in helping usher in the age of renewable sources of energy is firstly provided. Next, a few fundamentals in NIBs are given with an emphasis on providing a good balance between theoretical concepts and working knowledge such that even an inexperienced reader who is not familiar with batteries can grasp the major results of this thesis. This will be followed by a comprehensive literature review which will present the most significant research conducted in this field. Finally, the objectives of the thesis will be stated, followed by a description of how this thesis is structured.

## 1.2 Introduction

The role of mankind in climate change has been firmly established over the past few years.<sup>1</sup> There is an urgent need to shift our dependence on energy from dirty fossil fuels to environmentally friendly and sustainable sources, more out of a desire to halt this global warming trend than out of fear of the fossil fuel reserves from extinguishing. In this regard, renewable sources of energy, such as solar, wind or tidal, would play a major role. These renewable sources of energy, unfortunately, suffer from a major drawback of exhibiting an inherent nature of intermittent availability. Hence, if these sources are to be successfully applied to the grid, an efficient and cost-effective storage system would be needed.<sup>2, 3</sup> Electrochemical energy storage devices, or batteries, are seen to be the most favourable candidate owing to a host of different factors: high energy densities, ability to demonstrate flexible response times, portability, pollution-free operation, long cycle life with low maintenance and high efficiency.<sup>2, 3</sup> The rechargeable lithium-ion battery (LIB) has emerged as the leading battery technology in terms of the above mentioned performance metrics over the past two decades. Owing to their high energy densities, LIBs are already dominant in the consumer electronics sector and now are primed to be widely used in electric vehicles.<sup>2-4</sup>

However, there have been concerns regarding the limited availability of lithium in the world. Upon widespread adoption of LIBs, it has been reported that the demand and hence future cost of lithium will likely increase.<sup>5</sup> This problem will be compounded if the burden of grid storage is also borne by LIBs. In essence, we would trade dependency on fossil fuels with that on lithium. Fortunately, the performance metrics for grid storage batteries are different from that required for electric vehicles and consumer electronics. Low operation and maintenance costs, high Round-Trip Energy Efficiency (RTEE- defined in section 1.3.3.3), long cycle life (at least up to 4,000

deep discharge cycles) and a high degree of safety are the desired qualities of a battery to be employed in the grid.<sup>3</sup> A high capacity and energy density are secondary factors. Even within grid storage, there can be specific applications that may favour certain performance qualities over others. For example, two important applications of grid storage are frequency regulation and load levelling. The former is used to regulate the alternating frequency of the grid and hence, fast response times within minutes (*i.e.* high power of a battery) and long cycle life are favoured over how long each cycle can last (*i.e.* over the capacity of a battery). On the other hand, load levelling deals with storing the excess energy generated by renewable sources of energy (such as during strong winds in the early morning) and using it to meet peak energy demands (such as during office hours).<sup>3</sup> This situation is illustrated in Fig. 1.1. In this way, the power plants do not have to be scaled to handle peak power periods (which may only last for a short time) and hence, over-sizing of power plants is avoided. Such an approach reduces redundancy and ensures all components of the grid are functioning at peak efficiency.<sup>2</sup> Regardless of the application, cost is the predominant factor for a grid storage battery. It would, hence, make tremendous sense to use a battery technology that does not rely on lithium to meet the energy storage needs of the grid. Batteries based on globally abundant sodium would be natural candidates for this purpose.<sup>4</sup>

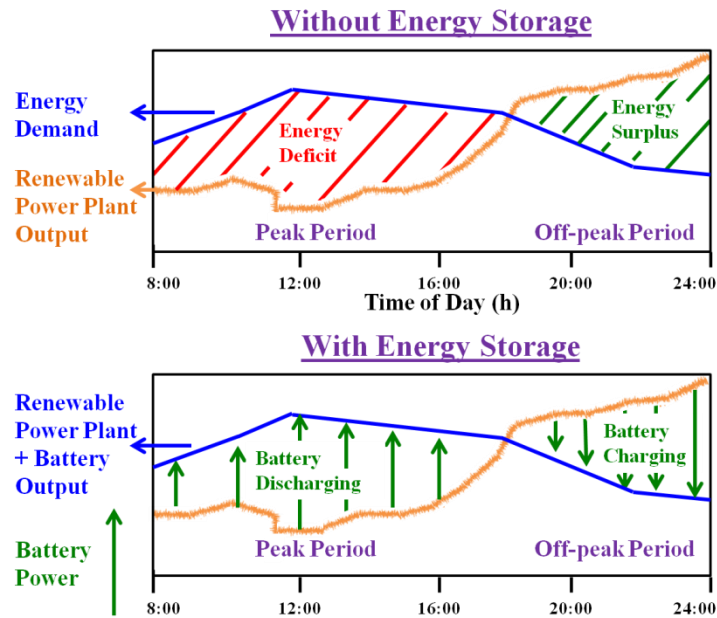


**Figure 1.1** | Illustration of how energy storage can help in load levelling operations for the grid. With storage, the renewable energy power plant’s capacity can be sized such that it does not have to generate according to the peak power demand; its capacity can be less, with the excess energy it generates during off-peak periods being stored, which would then be used during the peak power periods so as to adequately meet demand.

Sodium-based batteries are not a new technology; some have even been commercialized. High-temperature Na-S and Na-NiCl<sub>2</sub> (ZEBRA) batteries have been employed for grid storage in the past.<sup>3,4</sup> The Na-S battery, in particular, is regarded as a stellar candidate for grid storage batteries in terms of performance and economics, despite its high operation temperature of ~ 300 °C. However, its safety has been called into question especially after a recent fire incident involving them in Japan in the year 2011.<sup>4</sup> Sodium batteries operating at room temperature should alleviate such safety concerns. Room-temperature sodium-ion batteries (NIBs) have existed as early as the year 1980, soon after the discovery of LIBs.<sup>2,6</sup> However, further research in NIBs was suspended by the battery community in favour of developing LIBs due to the promise of higher energy densities. Over the past five years, interest in NIBs has been re-invigorated due to previously mentioned reasons for stationary applications for which footprint is not a serious concern. The similar working principles of NIBs and LIBs would mean that, at the very least, NIBs would be as safe as LIBs.<sup>4</sup> Before

outlining the state of research activities currently undergoing in the incipient field of NIBs and the scope of this thesis, it would be useful to gain the required working knowledge so as to better understand NIBs and the results of this thesis.

## **1.3 Working Knowledge of NIBs**

### **1.3.1 Principle of Operation**

A rechargeable room temperature NIB consists of two electrodes immersed in an electrolyte, as illustrated schematically in Fig. 1.2. Generally, the positive electrode, called the cathode, serves to provide sodium which is accepted by the anode, or the negative electrode. The electrolyte, which contains dissociated sodium salts in polar aprotic solvents, is a sodium ion conductor but electronic insulator. Hence, in travelling from the cathode to the anode or vice versa, the sodium is forced to travel as an ion ( $\text{Na}^+$ ), with the electrons travelling through the external circuit, thereby maintaining electro-neutrality. During discharging, sodium travels from the anode into the cathode, with the electrons travelling also from the anode to the cathode through the external circuit, doing the desired useful work. Simultaneously, the anode and cathode experience oxidation and reduction, respectively. The net result during the discharge process is the movement of sodium from the anode to the cathode. During charging, one needs to supply an external current such that the reverse process occurs: the sodium is forced to travel from the cathode to the anode. With this arrangement, a cathode can be any sodium compound which is capable of repeated sodium insertion/de-insertion. An anode can be any compound (not necessarily sodium based) similarly capable of sodium storage over many cycles.



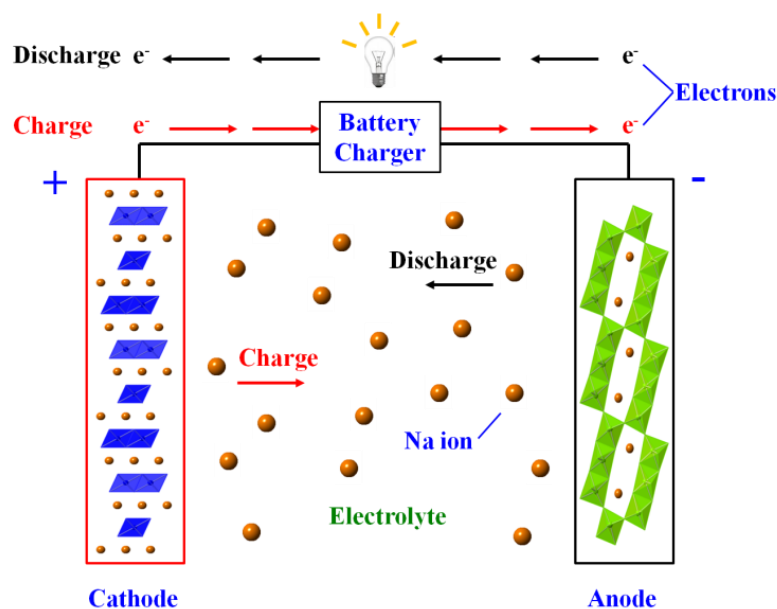


**Figure 1.2** | Schematic illustration of the operation mechanism within a sodium-ion battery. The motion of the sodium ions within the electrolyte and the electrons through the external circuit during charge and discharge has been emphasized.

### 1.3.2 Factors Determining the Voltage of a NIB

Similar to LIBs, NIBs display a rich variety of sodium storage mechanisms as dictated by the particular materials chosen for their cathodes and anodes. In this regard, some NIBs can deliver current at a fixed voltage, while some can do so with ever decreasing voltage values. To understand such differences better, a few fundamental guidelines and explanations are given below in this regard.

#### 1.3.2.1 Nernst Equation

The voltage delivered by any battery is dictated by thermodynamics. In any electrochemical cell, there are two opposing driving mechanisms: a chemical driving force and an electrostatic driving force. The chemical driving force across the cell is due to the difference in the standard Gibbs free energy change per mole of reaction,  $\Delta G_r$ . This is determined by the difference between the standard Gibbs free energies of formation of products and reactants in the virtual chemical reaction that would occur if the *electrically neutral* materials in the two electrodes were to react chemically (in

a NIB, it would be sodium).<sup>7</sup> The electrostatic energy per mole of an electrically charged species is  $-zFE$ , where  $E$  is the voltage between the electrodes, and  $z$  is the charge number of the mobile ionic species involved in the virtual reaction. The charge number is the number of elementary charges that they transport (hence,  $z = 1$  for  $\text{Na}^+$  ion).  $F$  is the *Faraday constant* (96,485.33 Coulombs per mole). Hence, these two driving forces are responsible for the cell potential and are related with equation (1.1):

$$\Delta G_r = -zFE \quad (1.1)$$

In a NIB, similar to the case of a LIB, the cell voltage changes with respect to the amount of sodium contained in the cathode and anode. This “amount of sodium in a phase” is captured by another thermodynamic quantity called the chemical potential,  $\mu$ . In turn, this chemical potential can be further simplified to another thermodynamic entity called the activity,  $a$ . The activity of a species is simply its effective concentration. For example, the activity of sodium,  $a_{\text{Na}}$ , in its pure metal form will be unity. It can be shown that the above equation (1.1) can be simplified in terms of the activities of sodium present in the cathode and anode, to give the Nernst Equation, as shown in equation (1.2).<sup>7</sup> Hence, the measured voltage of a NIB really depends on the activities of sodium contained within the two electrodes.

$$E = -\left(\frac{RT}{zF}\right) \ln \frac{a_{\text{Na}}(\text{Cathode})}{a_{\text{Na}}(\text{Anode})} \quad (1.2)$$

### 1.3.2.2 Gibbs Phase Rule

Some batteries supply current with ever decreasing voltage as the discharge proceeds, while other batteries do so at constant voltage. Apart from the Nernst equation, another useful thermodynamic equation to predict the shape of the voltage-composition curve is the application of the Gibbs Phase Rule depicted as shown by equation (1.3).<sup>7</sup>

$$F = C - P + 2 \quad (1.3)$$

In this equation,  $F$  is the number of degrees of freedom allowed to the system. Generally, independent and intensive thermodynamic parameters such as temperature, pressure and chemical potential of sodium are the most useful parameters for considering  $F$ . In most room-temperature NIBs, the temperature and pressure are constants.  $C$  represents the minimum number of constituents needed in order to describe completely the compositions of the phases present.  $C$ , could hence, be elements or molecules, as the case may be.  $P$  stands for the number of phases present in the system considered.<sup>7,8</sup> If a cathode/anode consists of two constituents ( $C=2$ ) and the sodiated phase is disparate from the de-sodiated phase ( $P = 2$ ), then,  $F = 2$ . In other words, if just two intensive properties of the cathode/anode are specified (such as temperature and pressure), then, the *residual degree of freedom* is zero. This means that no other intensive thermodynamic properties of the cathode/anode can change. Hence, it will discharge/charge at constant voltage. On the other hand, if the sodiated and de-sodiated phase is the same (one could be a solid-solution of the other), then application of the Gibbs Phase Rule will cause the voltage to vary with the state of discharge/charge.<sup>7</sup>

### 1.3.2.3 Polarization

If a battery delivers current at a voltage different from the theoretical voltage predicted by equation (1.2), then this phenomenon is called polarization. To overcome this polarization, the battery discharges at a voltage lower than the theoretical voltage and this difference is called the overvoltage,  $\eta$ . Likewise, during charging, one needs to supply current at a higher voltage. Polarization leads to a hysteresis between the charging and discharging voltage profiles, leading to energy inefficiency (more energy would be required to charge the battery than what it would be able to provide during discharge). Please note that there is often overlap in the

terminology with regards to polarization, overvoltage and voltage hysteresis. In this text, polarization would be generally used to refer to the difference between the charging and discharging voltages of a cathode/anode. To minimize polarization losses, a high electrode surface area ensuring adequate electrolyte wetting along with sufficient electrolyte conductivity and appropriately small particle size of the active material are quite helpful (assuming that the basic oxidation/reduction processes have sufficient kinetics and various components are compatible with each other).<sup>9</sup>

### **1.3.3 Performance Metrics of a NIB**

There are certain metrics that are quite commonly used to describe the performance of a battery. In this thesis, these metrics would be used as well. A brief definition of these terms is as follows.

#### **1.3.3.1 Specific Capacity**

The greater the sodium storage ability of a cathode or anode, the lighter the battery will be. Hence, the performance metric in a battery that accounts for the charge storage ability of a material is termed the “specific capacity” which is the amount of charge that a material can store per unit mass. The unit of specific capacity is  $Ah/g$  or  $mAh/g$ . The specific theoretical capacity of an electrode material would, hence, just indicate how many moles of sodium can be stored in the crystal structure of an electrode material, per mole of that material. The following formula can be used to compute the theoretical specific capacity of a material:

$$\text{Specific Theoretical Capacity (mAh/g)} = \left( \frac{F \times n}{M \times 3600} \right) \times 1000 \quad (1.4)$$

In this equation,  $F$  is the Faraday’s Constant,  $n$  refers to the number of moles of sodium stored per mole of the host material and  $M$  is the molecular weight of the host electrode material. Needless to say, the lighter is the host material and the greater is

the number of moles of sodium that it can store, the higher will be its theoretical specific capacity.

### 1.3.3.2 Specific Energy Density

The cathode operates at a higher voltage than the anode. Hence, the greater the potential difference in the redox (reduction-oxidation) voltages of the cathode and anode, the greater will be the voltage delivered by a NIB. For a given specific capacity, greater voltage will translate to higher energy stored. To capture the amount of energy that a battery can store, the most common metric used is that of the “specific energy density” whose relation with the specific capacity is shown below in equation (1.5).

$$\text{Specific Energy Density (Wh/kg)} = \text{Specific Capacity } \left( \frac{\text{mAh}}{\text{g}} \right) \times \text{Voltage (V)} \quad (1.5)$$

### 1.3.3.3 Round Trip Energy Efficiency (RTEE)

The RTEE is a product of the coulombic efficiency ( $CE_{ff}$ ) and the voltage efficiency ( $VE_{ff}$ ). Coulombic efficiency ( $CE_{ff}$ ) is defined as the ratio of the discharge capacity to the charge capacity, as demonstrated by equation (1.6) below:

$$\text{Coulombic Efficiency, } CE_{ff} = \left( \frac{\text{Discharge Capacity}}{\text{Charge Capacity}} \right) \quad (1.6)$$

The voltage efficiency ( $VE_{ff}$ ) is the ratio of the discharging voltage to that of the charging voltage, as illustrated by equation (1.7).

$$\text{Voltage Efficiency, } VE_{ff} = \left( \frac{\text{Discharge Voltage}}{\text{Charge Voltage}} \right) \quad (1.7)$$

The RTEE can, hence, be described as a percentage as displayed in equation (1.8) below:

$$RTEE = (CE_{ff} \times VE_{ff}) \times 100 \quad (1.8)$$

### 1.3.3.4 Definition of *C* rate and Rate Performance

Generally, during galvanostatic cycling (constant current cycling) of a battery, the norm is to specify the magnitude of the current not in terms of the actual units of current (*mA* or *A* for example), but in relative units scaled to the battery's capacity called the “*C* rate”. The “*C* rate”, hence, refers to the current that would result in complete charge/discharge within a time frame. For example, a current corresponding to *C*/10 rate would mean complete charge/discharge within 10 *h*, while a cycling current of 5 *C* would mean complete charge/discharge within 12 *min* (1/5 *h*). An ideal battery would deliver the same capacity (its theoretical capacity) irrespective of the *C* rate used (it would deliver the same capacity at a very slow *C*/100 rate or ultra-fast 100 *C* rate). To capture the battery's response to different current magnitudes, rate performance galvanostatic cycling tests are often conducted, where the battery would be subjected to different *C* rates in succession to gauge how much capacity it is able to deliver at each rate.

### 1.3.4 Half Cell Evaluation of Cathode/Anode

To evaluate the sodium storage properties of a cathode/anode, the most common practice in the field of NIBs (and correspondingly in LIBs for lithium storage studies) is to evaluate them against sodium metal in the so called “half cell” approach. In this way, the voltage registered by a cathode/anode would directly be *vs* Na/Na<sup>+</sup>. Making sodium metal as the counter and the reference electrode simultaneously, is hence, quite convenient. An important point to note while utilizing this half cell approach is that while studying electrode materials that would be anodes in NIBs, one needs to be wary of the meaning of the terms described in the previous section. This is because though the electrode studied has low voltage activity, its voltage will always be more

positive versus that of the  $\text{Na}/\text{Na}^+$  couple (*i.e.* with respect to sodium metal). Hence, in a half cell, an anode becomes a cathode. Therefore, the  $\text{CE}_{\text{ff}}$  of an anode studied in a half cell should be a ratio of the charge capacity to that of the discharge capacity, that is, the inverse of equation (1.6). The reason is that it is actually the charge process in a half cell for an anode (sodium de-insertion from the anode) that corresponds to the discharge process in a full cell (sodium leaving the anode and entering the cathode). Hence, all terms are defined/used keeping the full cell application in mind.

### **1.3.5 Types of Sodium Storage Mechanisms**

There are three major and distinct mechanisms whereby electrode materials can store sodium in NIBs.<sup>10, 11</sup> These mechanisms have direct correlation to all the performance metrics mentioned above, as well as on the shape of the galvanostatic cycling curves. Briefly, they are described below.

#### **1.3.5.1 Insertion Reaction Mechanism**

Sodium atoms are inserted within/extracted from the empty spaces (tunnels or layers, as the case may be) of the crystal structure of the anode/cathode. There can be two types of insertion reactions:

1. Solid-solution mechanism: The original electrode phase and the (de-)sodiated phase are essentially the same phase. Due to the Gibbs phase rule, such solid-solution reaction mechanisms result in sloping galvanostatic voltage profiles.
2. Two-phase mechanism: The original electrode phase and the (de-)sodiated phase are different. Application of the Gibbs Phase Rule results in these electrode materials storing sodium at constant voltages.

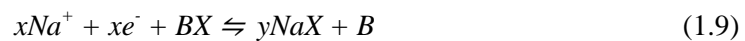
Examples: Very common among electrode materials, almost all cathode materials, all sodium titanate anodes, etc.

Major advantages: Less volume change upon sodium storage. Hence, they generally demonstrate long cycle life and less polarization.

Limitations: Capacity is typically moderate, not exceeding 250 *mAh/g*.

### 1.3.5.2 Conversion Reaction Mechanism

These involve significant bond breaking of the parent material phase. The general equation for conversion reactions can be summarized as equation (1.9) below.



where BX generally is a metal oxide such as MoO<sub>3</sub> or Fe<sub>2</sub>O<sub>3</sub>.

Examples: Generally binary transition metal oxide anodes operating at low voltages.

Major Advantages: Due to the possibility of storing many moles of sodium per mole of host material, capacity can be very high (300 – 1000 *mAh/g*).

Limitations: Generally display high polarization. Due to significant bond breaking of the host material, cyclability is an issue.

### 1.3.5.3 Alloy Reaction Mechanism

Sodium is stored by forming an alloy with the host material.

Examples: Exhibited by anodes exclusively, such as Sn, P, Sb etc.

Major advantages: Similar to conversion reactions, possibility of very high capacities (up to 1,800 *mAh/g* possible).

Limitations: Similar to conversion reactions, they display high polarization. Furthermore, enormous volume change (can be up to 300-400 % or possibly more) induced by storage of many moles of sodium (sometimes up to ten moles) per mole of host material can limit cyclability.



## 1.4 Literature Review on NIB Research

### 1.4.1 Half Cell Results of NIB Cathodes and Anodes

Interest in NIBs has increased exponentially over the past five years. There have been various reports of high energy density cathodes such as  $\text{Na}_3\text{V}_2(\text{PO}_4)_2\text{F}_3$ ,<sup>12-14</sup>  $\text{Na}_3\text{V}_2(\text{PO}_4)_3$ <sup>15</sup> and  $\text{Na}_2\text{Fe}_2(\text{SO}_4)_3$ .<sup>16</sup> The cathodes  $\text{R-Na}_{1.92}\text{Fe}[\text{Fe}(\text{CN})_6]$ ,<sup>17</sup>  $\text{Na}_{2-6}\text{MnFe}(\text{CN})_6$ ,<sup>18</sup>  $\text{P2-Na}_{2/3}[\text{Fe}_{1/2}\text{Mn}_{1/2}]\text{O}_2$ <sup>19</sup> and  $\text{Na}_{1.5}\text{VPO}_{4.8}\text{F}_{0.7}$ <sup>20</sup> have been shown to rival and even surpass the performance of current LIB cathodes suggesting that adopting NIBs may not necessarily mean a sacrifice of the energy density. While significant progress has already been achieved on the cathode in a short period of time, no single NIB anode has been shown to have a good combination of acceptable capacity with an attractive voltage profile. Please note that it may not be advisable to use sodium metal as an anode due to safety concerns owing to the possibility of dendrite formation and the much lower melting point of sodium metal (97.7 °C) vs that of lithium metal (180.5 °C).<sup>11, 21</sup> Hence, appropriate anode materials need to be discovered, especially considering the fact that sodium cannot intercalate in appreciable amount in graphite which is the state-of-the-art anode for LIBs.<sup>21</sup> However, since sodium does not alloy with aluminium, aluminium can be used as the current collector for both cathode and anode in NIBs and this precludes the use of heavy and expensive copper as current collector for the anode side.<sup>21</sup> This is expected to lead to significant cost and weight savings for NIBs with respect to LIBs as copper is used as the current collector for the anode in LIBs due to the fact that lithium alloys with aluminium.<sup>21, 22</sup>

The high capacity anode materials, such as those based on alloy and conversion reactions<sup>23-25</sup> or organic carboxylate-based materials,<sup>26, 27</sup> typically suffer from large polarization,<sup>28</sup> and/or huge volume change (which limits cyclability or lifetime). This large polarization will result in low RTEE in a full cell caused by low  $\text{VE}_{\text{ff}}$ . Carbon

based anodes, such as hard carbon,<sup>29</sup> are typically unstable in the sodiated state displaying an exothermic peak at low temperatures of around 100-150 °C.<sup>30, 31</sup> Furthermore, hard carbon's extremely low voltage plateau below 0.1 V vs Na/Na<sup>+</sup> can increase risks of sodium plating leading to an internal short-circuit, especially if used in NIBs being charged at a high C rate. These two factors would likely make hard carbon an unsuitable choice as an NIB anode in all applications requiring moderately fast or fast charging.

In light of these drawbacks with conversion, alloying and carbon based materials, most of the promising anodes have been shown to operate on an insertion based mechanism which favours long cycle life due to minimal volume changes to the material. In particular, many titanium based anodes have been shown to function well for NIB application. However, these anodes, such as NaTi<sub>2</sub>(PO<sub>4</sub>)<sub>3</sub>,<sup>32</sup> Li<sub>4</sub>Ti<sub>5</sub>O<sub>12</sub>,<sup>33</sup> anatase TiO<sub>2</sub>,<sup>34</sup> amorphous TiO<sub>2</sub>,<sup>35</sup> hollandite type- TiO<sub>2</sub>,<sup>36</sup> lepidocrocite-type Na<sub>0.8</sub>Ti<sub>1.73</sub>Li<sub>0.27</sub>O<sub>4</sub><sup>37</sup> and NaTi<sub>3</sub>O<sub>6</sub>(OH).2H<sub>2</sub>O<sup>38</sup> either suffer from a high operating voltage above 0.8 V vs Na/Na<sup>+</sup> and/or steep, sloping galvanostatic profiles which would decrease the energy densities of NIBs which may incorporate them. In any case, long term cycling has not been reported, effectively eliminating their utilization in grid storage batteries until such data can be conclusively shown.

The most promising anodes reported thus far have been P2-Na<sub>0.66</sub>[Li<sub>0.22</sub>Ti<sub>0.78</sub>]O<sub>2</sub><sup>39</sup> and Na<sub>2/3</sub>Co<sub>1/3</sub>Ti<sub>2/3</sub>O<sub>2</sub>.<sup>40</sup> These display good cycle life in excess of 1,200 and 3,000 cycles respectively at a desirable average voltage close to 0.80 V vs Na/Na<sup>+</sup>. However, their dependence on scarce lithium or toxic cobalt resources may not be ideal due to aforementioned reasons.<sup>4</sup> Furthermore, these two anodes display poor high rate performance with large polarization. While the usable capacity of P2-Na<sub>0.66</sub>[Li<sub>0.22</sub>Ti<sub>0.78</sub>]O<sub>2</sub> is 100 mAh/g at a slow rate of C/10 with a sloping charge plateau between 0.6 – 1.1 V, at 2 C rate, the capacity drops to just 62 mAh/g with the charge plateau between 0.7 – 1.25 V.<sup>39</sup> Na<sub>2/3</sub>Co<sub>1/3</sub>Ti<sub>2/3</sub>O<sub>2</sub>, on the other hand, was reported to

show 90 *mAh/g* at *C/5* with sloping charge plateau between 0.8 – 1.1 V, but at 10 *C*, the charge capacity dropped to just 35 *mAh/g* with the charging plateau now at a high voltage between 1.2 – 1.7 V.<sup>40</sup> The drawback in these materials from a performance point of view is not necessarily less capacity at high rates (capacity is just a secondary factor in grid storage batteries), but it is the increased polarization at high rates. Especially for frequency regulation, where anode materials may need to exhibit excellent high rate performance, this large polarization would really decrease RTEE in a NIB employing them as the anode. Hence, none of these materials have been demonstrated to be promising anode materials satisfying all qualities expected of electrode materials for grid storage batteries.

#### **1.4.2 The Solid Electrolyte Interphase in NIBs**

At low voltages close to 0.0 V *vs* Na/Na<sup>+</sup>, electrolyte decomposition occurs in NIBs, similar to the case of LIBs. At such reducing voltages, the alkylcarbonate solvents typically used in non-aqueous NIB electrolytes are reduced to form a passivating film on low voltage NIB anodes.<sup>29</sup> This passivating film, called the solid electrolyte interphase (SEI), is ionically conducting but electronically insulating. Hence, once formed, the SEI film on the anode prevents further electrolyte reduction (due to its electronically insulating character) yet promotes sodium ion diffusion into the anode which lies below this cationically conducting SEI layer.<sup>6, 21, 22</sup> Since charge is consumed to form this SEI, its formation leads to an irreversibility in the first cycle of low voltage anodes. This irreversible capacity loss (ICL) leads to low first cycle CE<sub>ff</sub> of such low voltage anodes which could be as low as 30 – 50 %.<sup>21, 22</sup> Typically, SEI formation takes a few cycles to be complete, however, the majority of SEI formation occurs in the first cycle. Hence, the CE<sub>ff</sub> of low voltage NIB anodes increases rapidly within the first few cycles and approaches 100 % thereafter (depending on the inherent reversibility of the NIB anode).

In the NIB field, SEI effects typically become noticeable below 0.8 V vs Na/Na<sup>+</sup> in terms of an observable amount of first cycle ICL. Since SEI formation is due to electrolyte reduction, it follows that high surface area anodes, which have a greater amount of electrochemically active surface area, would result in greater SEI formation (and hence, greater first cycle ICL). In this context, the lower cycling voltage limit of an anode, the surface area of the active material of an anode, the type of conductive additive used, the type of binder used and the nature of the electrolyte and electrolyte additives (if any) significantly affect the amount of this first cycle ICL caused by SEI formation as well as the cycle life of an anode.<sup>21, 22, 29</sup> While not many studies have been performed on SEI in NIBs, the results of a handful of studies conducted on NIB SEI indicate a key difference in the SEI formed in NIBs with that formed in LIBs, viz. the former is richer in inorganic species than the latter.<sup>41-43</sup> SEI effects plague all low voltage NIB anodes and hence, it is a systemic challenge in this field to engineer a stable SEI as it has direct implications on two very important performance factors for low voltage NIB anodes: the first cycle CE<sub>ff</sub> and its cycle life.

### 1.4.3 Current State-of-the-Art Full Cell Results

Most full cell studies reported thus far in the literature have utilized hard carbon as the anode. The use of hard carbon for grid storage batteries may not be attractive due to previously mentioned reasons. In light of this, the most significant demonstrated results of NIBs using insertion based cathodes and anodes are as follows. A full cell employing Na<sub>3</sub>V<sub>2</sub>(PO<sub>4</sub>)<sub>3</sub>/C as the cathode and Li<sub>4</sub>Ti<sub>5</sub>O<sub>12</sub> as the anode was shown to demonstrate an energy density ~ 114 Wh/kg (based on the weight of the cathode and anode active materials) at C/10 rate,<sup>33</sup> while a Na<sub>3</sub>V<sub>2</sub>(PO<sub>4</sub>)<sub>3</sub>/C // P2-Na<sub>0.66</sub>[Li<sub>0.22</sub>Ti<sub>0.78</sub>]O<sub>2</sub> full cell delivered ~ 87 Wh/kg at C/8 rate.<sup>39</sup> For both these full cells, cycling data was limited to 20 cycles and hence, accurate analysis on the viability of its use for grid storage batteries is inconclusive currently. Finally, an NIB using P2-Na<sub>0.8</sub>Li<sub>0.12</sub>Ni<sub>0.12</sub>Mn<sub>0.66</sub>O<sub>2</sub> as the cathode and the Na<sub>2</sub>Ti<sub>3</sub>O<sub>7</sub> ⇌ Na<sub>4</sub>Ti<sub>3</sub>O<sub>7</sub>

pathway as the anode exhibited about 137 Wh/kg energy density at C/10 rate with ~ 69 % capacity retention over 30 cycles.<sup>44</sup> It can be seen that previous reports on full cell performance in NIBs show a great deal of promise although long term cycling studies, required for accurate analysis for grid storage battery applications, have not been reported thus far.

## **1.5 Objective of the Thesis's Research**

It is clear that there is still not a suitable NIB anode that is composed of earth-abundant elements displaying all the performance requirements expected for an electrode material to be employed in grid storage NIBs. Hence, the work contained in this thesis aims to fill this void in the current state of affairs of NIBs. The desired qualities expected of such an anode are namely: utilization of earth-abundant elements which would keep costs low, having the potential to display long cycle life exceeding 4,000 cycles, demonstrating high RTEE brought about by high coulombic efficiencies and minimal polarization preferably even at high rates and excellent safety. Good high rate performance would be especially useful for grid storage batteries targeted at frequency regulation. In addition, it would be desirable for the anodes to possess decent capacity values and low voltage redox activities, though these may not be primary considerations. Keeping all these points in mind, the chosen materials for this thesis belong to the sodium titanate family. Apart from utilizing earth-abundant elements of Na, Ti and O, the sodium titanates have a rich chemistry with many phases, giving great flexibility for researchers to discover a high performance sodium storage phase(s).<sup>28</sup> Hence, the thesis aims to explore them as potential anode materials for grid storage NIBs.

## **1.6 Structure of the Thesis**

The thesis is structured as follows:

In **chapter 1** (present chapter), the basics of NIBs will be given such that a reader who is not very familiar with them will still be able to understand the results of the thesis and be able to judge the merit of the work, in relation with what exists in the literature thus far. In **chapter 2**, it will be shown that the sodium titanate,  $\text{Na}_2\text{Ti}_6\text{O}_{13}$ , displays all qualities expected of a grid storage NIB electrode material, highlighted by an ultra-long cycle life of 5,000 cycles. The only issue with this material is its relatively low capacity of 50 *mAh/g*. While capacity and energy density are not crucial factors for grid storage batteries, it will always be favourable to have materials which have higher values for these two metrics. With this in mind, **chapter 3** presents the sodium storage results on another sodium titanate phase,  $\text{Na}_2\text{Ti}_3\text{O}_7$ , which possesses a higher capacity (178 *mAh/g*) at low average voltage of 0.3 V vs Na/Na<sup>+</sup>. Efforts were made towards optimizing its performance; however, its high polarization and inadequate cycling stability were not resolved. In the course of understanding its sodium storage, two puzzling observations were made. One of these observations proved to be quite fundamental towards understanding the behaviour of electrode materials in sodium batteries. These results are contained in **chapter 4**. The understanding obtained from this work was very useful in understanding the second observation and it led to the results described in **chapter 5** which deals with a new sodium storage mechanism for  $\text{Na}_2\text{Ti}_3\text{O}_7$ . This mechanism, discovered for the first time in this work, results in a NIB anode having the potential to exhibit all qualities required of an anode meant for grid storage batteries highlighted by the lowest redox voltage plateau ever reported for any non-carbon based NIB anode. Its utilization as an anode in a full NIB using an appropriate cathode is shown to result in the highest voltage non-carbon based NIB existing thus far which holds great promise for high energy density grid storage batteries. **Chapter 6** states the conclusions of this thesis and opportunities for future research activities arising from these results.

## Chapter 2 | $\text{Na}_2\text{Ti}_6\text{O}_{13}$ : a Potential Anode for Frequency Regulation Grid Storage Sodium-ion Batteries

---

The results described in this chapter have been published/presented in the following journals/conferences:

1. **A. Rudola, K. Saravanan, S. Devaraj, H. Gong and P. Balaya, Chem. Commun., 2013, 49, 7451-7453**
2. 11<sup>th</sup> International Conference on Ceramic Materials and Components for Energy and Environmental Applications (**CMCEE 2015**), Vancouver, Canada, June 2015 → **Oral Presentation**
3. 1<sup>st</sup> International Symposium on Engineering Science, Singapore, May 2015 → **Oral Presentation**
4. 55<sup>th</sup> Battery Symposium in Japan, Kyoto, Japan, November 2014 → **Oral Presentation**
5. 7<sup>th</sup> International Conference on Materials for Advanced Technologies (**ICMAT 2013**), Singapore, July 2013 → **Poster Presentation**
6. Lithium Battery Discussions (**LIBD 2013**), Arcachon, France, June 2013 → **Poster Presentation**

## 2.1 Preface to Chapter 2

With the ultimate application to grid storage NIBs in mind,  $\text{Na}_2\text{Ti}_6\text{O}_{13}$  nanorods were synthesized in gram scale from a very inexpensive and easy-to-scale up solution route. The as-synthesized material was found to display an extremely long cycle life (in excess of 5,000 cycles) along with impressive high rate performance capable of response up to 30 C (2 min). *Ex-situ* XRD studies pointed to a solid-solution reaction mechanism for  $\text{Na}_2\text{Ti}_6\text{O}_{13}$ , which resulted in it displaying close to its theoretical capacity (50 mAh/g) at a low average voltage of 0.85 V vs Na/Na<sup>+</sup> with minimal volume changes (less than 1 %). Studies to evaluate the stability of the sodiated material resulted in excellent safety, till 500 °C. Its utilization in a full NIB was shown to produce a stable 2.5 V battery with excellent capacity retention even after 400 cycles. Such excellent full cell results are the first of its kind to be demonstrated in the field of NIBs. The combination of low materials and synthesis cost, long and stable cycle life with excellent efficiency, good high rate performance, high degree of safety and utilization of environmentally benign and abundant materials makes this anode a very attractive option for grid storage NIBs, especially for those meant for frequency regulation.



## 2.2 Introduction

The crystal structure of  $\text{Na}_2\text{Ti}_6\text{O}_{13}$  was solved in the early 1960's by Andersson and Wadsley.<sup>45</sup>  $\text{Na}_2\text{Ti}_6\text{O}_{13}$  has a monoclinic structure with the space group  $C2/m$ . It consists of an array of three  $\text{TiO}_6$  zig-zag octahedra that share edges to form a chain. The sodium ions reside in the inter-layer positions between the  $\text{TiO}_6$  slabs (refer to Fig. 2.1). This configuration leaves vacant tunnels along the  $b$ -axis, represented by beach balls in Fig. 2.1, where alkali ion intercalation is expected to take place.<sup>46</sup>

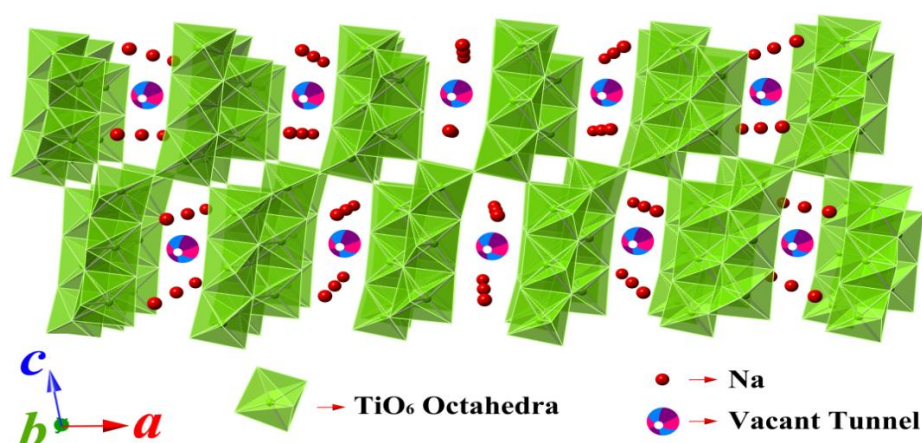


**Figure 2.1** | Crystal structure of  $\text{Na}_2\text{Ti}_6\text{O}_{13}$  when viewed along the  $b$ -axis. Large tunnels are evident along the  $b$ -axis, indicated by the beach balls. The  $b$ -axis is pointing perpendicularly out of the plane of the paper.

Indeed,  $\text{Na}_2\text{Ti}_6\text{O}_{13}$  was shown to be electrochemically active in a lithium cell.<sup>47</sup> Recently, it was reported to reversibly cycle less than half a mole of sodium per mole of  $\text{Na}_2\text{Ti}_6\text{O}_{13}$  when cycled at  $C/12$  in a sodium cell<sup>48</sup> (1 mole of charge storage corresponds to 49.5  $\text{mAh/g}$  of theoretical specific capacity, with  $1C$  corresponding to complete charge/discharge in 1  $h$ ). Though the material's reversible capacity was quite less, it displayed a plateau around 0.85 V, recognizing it as a safe anode material that would lead to a high voltage NIB if coupled with an appropriate high potential cathode material. In this work, we present the impressive storage performance of  $\text{Na}_2\text{Ti}_6\text{O}_{13}$  nanorods prepared by soft-template method. We demonstrate an excellent high rate response and ultra-long cycle life of this material. In addition, the feasibility

of this anode in a full NIB cell is shown. The mechanism of sodium insertion into  $\text{Na}_2\text{Ti}_6\text{O}_{13}$  is also discussed. Finally, the thermal stability of the sodiated  $\text{Na}_2\text{Ti}_6\text{O}_{13}$  material is investigated.

## **2.3 Experimental Section**

### **2.3.1 Synthesis**

$\text{Na}_2\text{Ti}_6\text{O}_{13}$  was synthesized by a soft-template method using sodium acetate and titanium isopropoxide as the sodium and titanium sources, respectively. 3.64 g of cationic surfactant, CTAB (hexadecyl-trimethyl-ammonium bromide) was dissolved in a mixture containing 30 mL milli-Q water and 90 mL ethanol. Appropriate molar ratio of the sodium and titanium sources were then added and stirred for 12 h. The solution was then dried using a rotor-evaporator. The obtained powder was then sintered in air at 800 °C for 6 h.

### **2.3.2 Synthesized Powder Characterization**

Powder X-ray Diffraction (PXRD) patterns were recorded using a Bruker D2 Phaser X-ray diffractometer equipped with Cu  $K\alpha$  radiation. The accelerating voltage and current were 40 kV and 40 mA, respectively. A step size of 0.02 ° was used with 0.2 s per step. The morphology of the product was examined using Field Emission Scanning Electron Microscopy, FESEM (model JEOL JSM-7000F), operated at 15 kV and 20 mA. A JEOL JEM-2010 instrument was used for obtaining High Resolution Transmission Electron Microscopy (HRTEM) images as well as Selected Area Electron Diffraction (SAED) patterns. For Transmission Electron Microscopy (TEM) studies, the powder was dispersed in ethanol and sonicated, before being loaded on a Cu grid and dried.

### 2.3.3 Electrochemical Characterization

For sodium storage studies without conductive additives, electrodes were fabricated with the active material and binder- polyvinylidene fluoride, PVDF (Kynar 2801)- in the weight ratio 90:10 using N-methyl pyrrolidone (NMP) as solvent. For the composite electrodes with conductive additives, the active material, Super P carbon black or graphite (Alfa Aesar), and binder were mixed in the weight ratio 70:20:10 using NMP as solvent. The obtained slurry was coated uniformly on a 15  $\mu\text{m}$  thick etched aluminium foil (Shenzhen Vanlead Technology) using a doctor blade and dried at 110  $^{\circ}\text{C}$  under vacuum for 12 *h*. The dried slurry was pressed using a twin roller of 37 *psi*. The active material loading was around 1.0  $\text{mg}/\text{cm}^2$  (in practice, thicker loadings of 2.6  $\text{mg}/\text{cm}^2$  also resulted in similar performance). Sodium metal foil (Merck), 1 M  $\text{NaClO}_4$  in ethylene carbonate (EC) (Alfa Aesar) and propylene carbonate (PC) (1:1 volume ratio) and Whatman Glass Microfibre Filter (Grade GF/F) were used as counter electrode, electrolyte and separator, respectively, to assemble coin-type cells (size 2016) in an argon filled glove box (MBraun, Germany). The sodium metal rods (Merck), immersed in kerosene, were wiped clean, cut into slices, rolled into the desired thickness and finally cut into circular disks. All cells contained a stainless steel spring between the sodium disk and the coin cell container to establish better contact. Charge–discharge cycling at a constant current mode was carried out using a computer controlled Arbin battery tester (Model, BT2000, USA) and cyclic voltammetry (CV) studies were carried out at room temperature using a computer controlled VMP3 battery tester (Bio-logic, France) in the voltage window 0.5 – 2.5 *V*. For the *ex-situ* X-ray Diffraction (XRD) studies of the cycled pure electrodes (without any carbon black) at different voltages, the electrode was charged/discharged at a rate of *C/5*. The discharged material was found to be unstable in air. This instability could be conveniently followed from the colour change of the electrodes- the fully discharged electrode was black in colour. It took

approximately 15 – 30 *min* in ambient air for the discharged electrode to start to change its colour to white. Hence, for the *ex-situ* studies, the electrodes were sealed in Ar filled containers and opened just prior to measurement. The total measurement time was 5 *min*. The discharged electrode was, hence, black in colour even after recording the XRD spectrum. For the variable temperature thermal XRD studies, the spectrum was obtained in vacuum. Rietveld refinement was performed using TOPAS 3.0 software, while the calculations to determine the lattice parameters at the various states of charge and discharge for the *ex-situ* XRD experiments were carried out using Prozski software, by following the shift in the 200, -201, 110, 310, 402 and 020 peaks. Thermogravimmetric Analysis (TGA) was performed on sodiated  $\text{Na}_2\text{Ti}_6\text{O}_{13}$  powder of weight around 2 *mg* in an alumina pan under nitrogen atmosphere with a ramp rate of 10 °C/*min*.

## 2.4 Results and Discussion

### 2.4.1 As-synthesized Powder Characterization

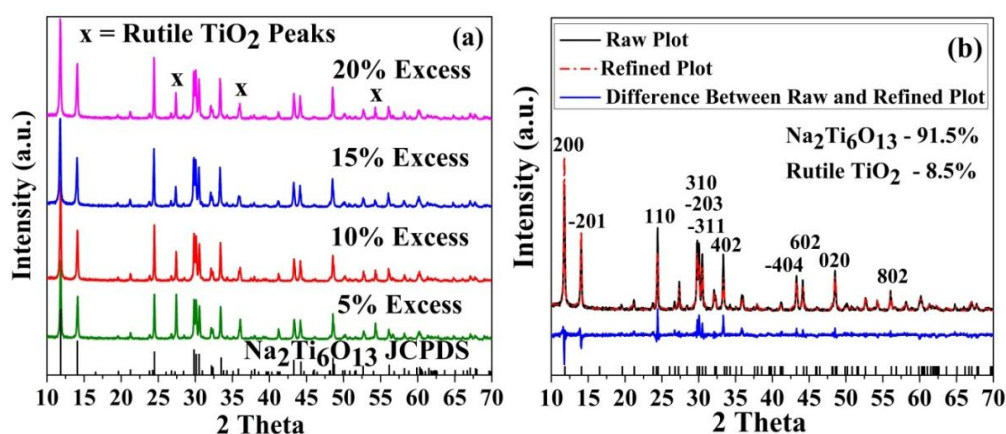


**Figure 2.2** | Evaluation of the phase purity of the as-prepared  $\text{Na}_2\text{Ti}_6\text{O}_{13}$  from the soft-template method. (a) PXRD patterns of the as-synthesized  $\text{Na}_2\text{Ti}_6\text{O}_{13}$  powders, as a function of the excess of sodium to titanium stoichiometric molar ratio. (b) Rietveld refinement of the as-prepared sample with 15% molar excess of the sodium source, with respect to the titanium source. A consideration of preferential orientation during refinement did not improve the fitting.

**Table 2.1** | Phase purity of the as-prepared Na<sub>2</sub>Ti<sub>6</sub>O<sub>13</sub> samples for different molar ratio of the Na and Ti sources, as determined from Rietveld refinement of PXRD data

Samples with different Na:Ti ratio	Molar Stoichiometry (Na:Ti)	Na <sub>2</sub> Ti <sub>6</sub> O <sub>13</sub> Phase (%)	Rutile TiO <sub>2</sub> (%)
<b>5% Excess</b>	1.05 : 3	81.5	18.5
<b>10% Excess</b>	1.10 : 3	88.6	11.4
<b>15% Excess</b>	1.15 : 3	91.5	8.5
<b>20% Excess</b>	1.20 : 3	90.5	9.5

Na<sub>2</sub>Ti<sub>6</sub>O<sub>13</sub> was synthesized from an inexpensive and easy to scale up soft-template method. It also resulted in a gram-scale amount of the final product. In fact, a single synthesis in a 250 mL glass vessel could result in a high yield of around 6 g of Na<sub>2</sub>Ti<sub>6</sub>O<sub>13</sub>. The PXRD pattern of the as-prepared Na<sub>2</sub>Ti<sub>6</sub>O<sub>13</sub> powder as a function of the excess of sodium to titanium molar ratio (stoichiometric molar ratio is 1:3) is depicted in Fig. 2.2a. All the peaks could be indexed with those belonging to Na<sub>2</sub>Ti<sub>6</sub>O<sub>13</sub> (JCPDS card number 73-1398), except for three peaks belonging to rutile TiO<sub>2</sub>. Occurrence of rutile TiO<sub>2</sub> impurity is common while preparing this phase<sup>49</sup> (rutile TiO<sub>2</sub> is electrochemically inactive with sodium). The fraction of rutile TiO<sub>2</sub> phase decreased as the molar excess of the sodium source was increased (refer to Table 2.1), though not monotonically. As indicated by Fig. 2.2b and Tables 2.2, 2.3 and 2.4, Rietveld analysis for 15% excess sample resulted in lattice parameters consistent with the literature ( $a = 15.0949(2)$  Å,  $b = 3.7452(8)$  Å,  $c = 9.1693(5)$  Å,  $\beta = 99.01^\circ$  and  $V = 510.6$  Å<sup>3</sup>).<sup>46, 47</sup> Increasing the sodium source to 20% excess compared to titanium source did not increase the phase purity further (see Table 2.1). Since the purest phase of Na<sub>2</sub>Ti<sub>6</sub>O<sub>13</sub> was obtained for 15% molar excess sample, further physical and electrochemical characterizations were performed on this sample.

**Table 2.2** | Lattice parameters obtained for the as-prepared Na<sub>2</sub>Ti<sub>6</sub>O<sub>13</sub> samples, as determined from Rietveld refinement.

Space Group	a (Å)	b (Å)	c (Å)	$\beta$ (°)	Volume (Å <sup>3</sup> )	R-Bragg	R <sub>wp</sub>	$\chi^2$
<b>C2/m</b>	15.094± 0.009	3.7434± 0.0007	9.168± 0.004	99.0164 ± 0.015	511.6± 0.7	8.06	17.81	1.56

**Table 2.3** | Refined crystallographic data for the as-prepared  $\text{Na}_2\text{Ti}_6\text{O}_{13}$  samples, as determined from Rietveld refinement. All values of x, y and z atomic positions have errors confined to the last digit.

Site	Wyckoff	x	y	z	Atom	Occ	$B_{iso}$
Na1	4a	0.454	0.0000	0.2508			
Ti1	4i	0.1137	0.0000	0.0895	Ti+4	1	1
Ti2	4i	0.1705	0.0000	0.4332	Ti+4	1	1
Ti3	4i	0.2287	0.0000	0.7726	Ti+4	1	1
O1	2a	0.0000	0.0000	0.0000	O-2	1	1
O2	4i	0.2280	0.0000	0.2470	O-2	1	1
O3	4i	0.0710	0.0000	0.2910	O-2	1	1
O4	4i	0.2820	0.0000	0.5740	O-2	1	1
O5	4i	0.1240	0.0000	0.6170	O-2	1	1
O6	4i	0.3580	0.0000	0.8840	O-2	1	1
O7	4i	0.1670	0.0000	0.9270	O-2	1	1

**Table 2.4** | Refined crystallographic data for the rutile  $\text{TiO}_2$  impurity in the as-prepared  $\text{Na}_2\text{Ti}_6\text{O}_{13}$  samples, as determined from Rietveld refinement. All values of x, y and z atomic positions have errors confined to the last digit.

Site	Wyckoff	x	y	z	Atom	Occ	$B_{iso}$
Ti1	2a	0.0000	0.0000	0.0000	Ti+4	1	1
O1	4f	0.3057	0.3057	0.0000	O-2	1	1

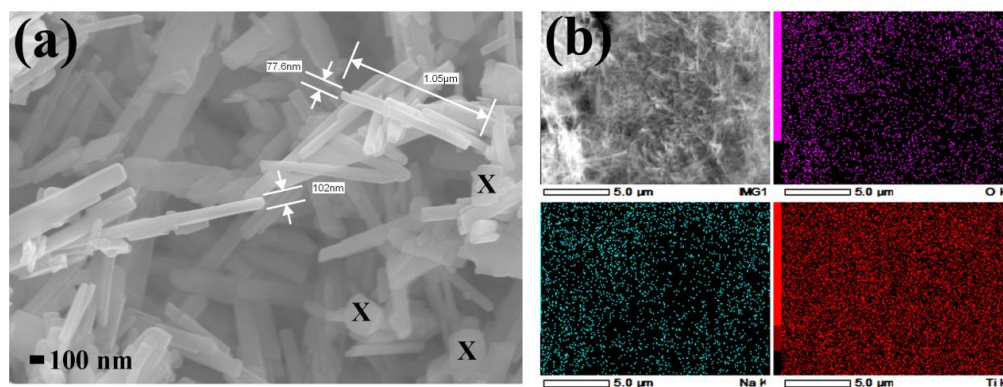


**Figure 2.3** | Morphology characterization of the as-prepared  $\text{Na}_2\text{Ti}_6\text{O}_{13}$  from the soft-template method. (a) FESEM image of the as-synthesized nanorods. The rutile  $\text{TiO}_2$  particles have been marked with an “X”. (b) EDX spectra of the as-prepared  $\text{Na}_2\text{Ti}_6\text{O}_{13}$  nanorods, clearly demonstrating a uniform distribution of Na, Ti and O throughout the sample.

Figure 2.3a presents the FESEM image of  $\text{Na}_2\text{Ti}_6\text{O}_{13}$  showing nanorod morphology, with width and thickness in the range 50-200 nm, and length in the range 0.5-2 µm. The FESEM image depicts some spherical particles (marked by “X” in Fig. 2.3a), which are believed to be the rutile  $\text{TiO}_2$  impurities. Energy-dispersive X-ray Spectroscopy (EDX) revealed uniform distribution of Na, Ti and O with no other impurity elements (see Fig. 2.3b). The HRTEM image and SAED pattern revealed

single crystalline nature of the nanorods and that they grew along  $b$ -axis in length, as deduced from the lattice fringes observed in the HRTEM image and the indexed  $0h0$  spots seen in the SAED pattern along the nanorod (refer to Fig. 2.4).

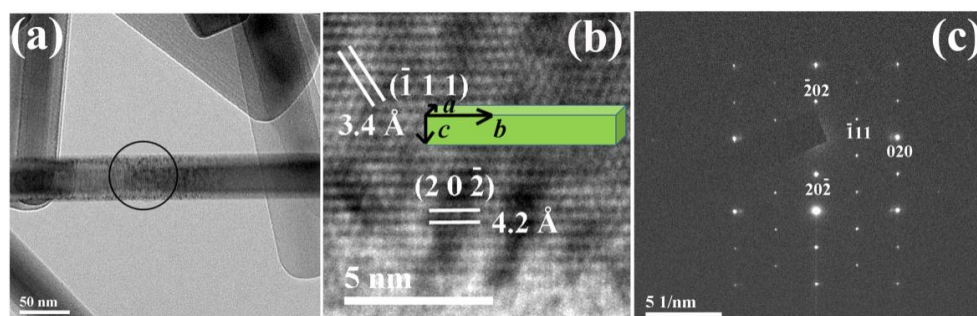


**Figure 2.4** | Evaluation of  $\text{Na}_2\text{Ti}_6\text{O}_{13}$  nanorod by TEM analysis. (a) TEM image of an isolated nanorod with the corresponding HRTEM pattern shown in (b) and the SAED pattern depicted in (c). The single-crystalline nature of the rod is evident. In (b), the rod can be seen growing along the  $b$ -axis in length with the inset depicting an illustration of a nanorod growing with its length along the  $b$ -axis (angle between  $a$  and  $c$ -axes is  $99^\circ$ ), The SAED indexed spots in (c) also highlight that the rod grows preferentially along  $[010]$ , the  $b$ -axis. The SAED pattern was recorded along the  $[101]$  zone axis.

## 2.4.2 Sodium Storage Mechanism

Galvanostatic cycling curves of an electrode consisting of just the as-synthesized  $\text{Na}_2\text{Ti}_6\text{O}_{13}$  nanorods with binder (henceforth referred as “pure  $\text{Na}_2\text{Ti}_6\text{O}_{13}$ ”) at a  $C/5$  rate is depicted in Fig. 2.5a. The electrode was first discharged (Na intercalation) and a sloping plateau (enlarged view in Fig. 2.5b) was observed around  $0.83\text{ V}$  yielding a first discharge capacity of  $65\text{ mAh/g}$ . In the subsequent charge (Na de-intercalation), similar sloping plateau behaviour was seen. A total first charge capacity of  $42\text{ mAh/g}$  was obtained.

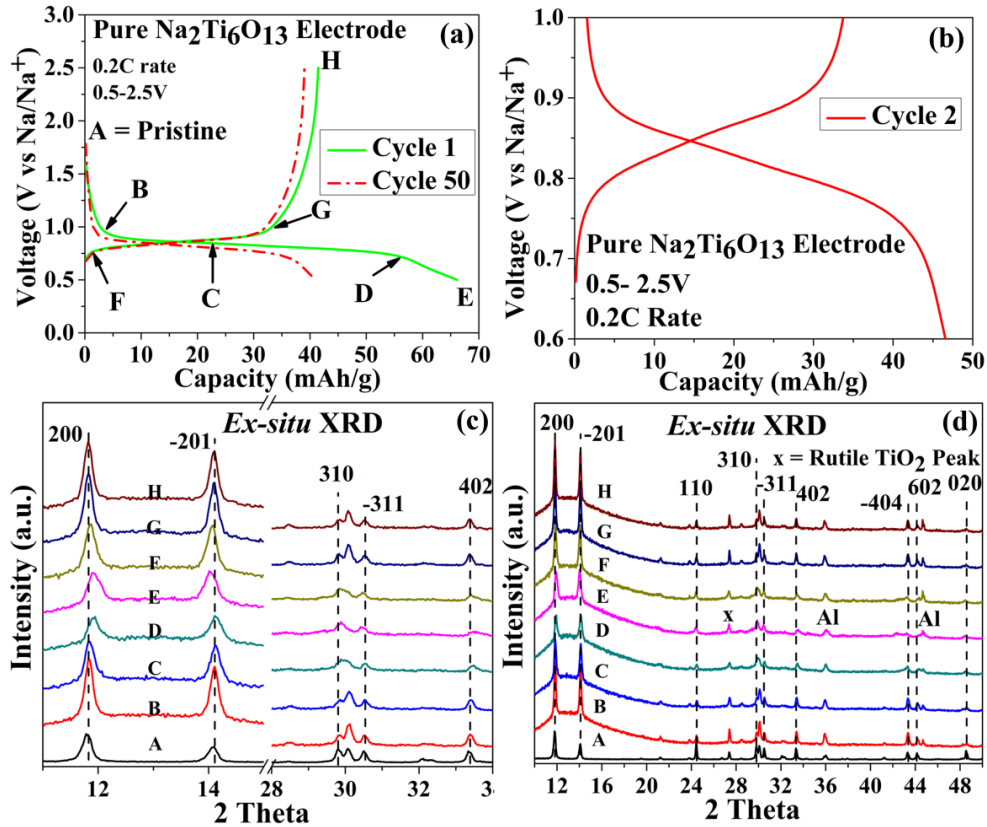


**Figure 2.5** | Evaluation of sodium storage mechanism of  $\text{Na}_2\text{Ti}_6\text{O}_{13}$ . (a) Galvanostatic cycling profiles of cycles 1 and 50 of a pure  $\text{Na}_2\text{Ti}_6\text{O}_{13}$  electrode, with different points on the first cycle where *ex-situ* XRD measurements were obtained. (b) Cycle 2 of a pure  $\text{Na}_2\text{Ti}_6\text{O}_{13}$  electrode at a C/5 rate showing the clear sloping nature of the plateau, when the y-axis scale is changed to 0.6-1.0 V, instead of the usual 0.5-2.5 V. This sloping plateau indicates a solid-solution nature of sodium storage. This was supported by (c) which depicts the *ex-situ* XRD of the pure  $\text{Na}_2\text{Ti}_6\text{O}_{13}$  electrode at various points indicated by (a) between 11-15° and 28-34°. (d) *Ex-situ* XRD of the pure  $\text{Na}_2\text{Ti}_6\text{O}_{13}$  electrode at various points indicated by (a) in the entire 10-50° 2 Theta range. No new peaks were seen at any states of charge/discharge. "Al" represents the peaks contributed from the Al current collector substrate.

To elucidate the sodium storage mechanism, *ex-situ* XRD was performed at various states of charge and discharge of the first cycle (see Fig. 2.5c and Fig. 2.5d). Different voltage points, represented by letters A through H in Fig. 2.5a, were selected so as to follow changes in the XRD spectrum closely as the state of discharge/charge was varied continuously. With sodium insertion/extraction, we did observe some systematic variations in the peak intensities and their positions (Fig. 2.5c). With increasing amount of sodium intercalation into  $\text{Na}_2\text{Ti}_6\text{O}_{13}$ , there was a continuous increase in  $c$  and  $\beta$  parameters, shown in Fig. 2.6a and Fig. 2.6b, while  $b$  value displayed negligible change. No conclusions could be drawn regarding change in the parameter  $a$ , as the observed trend was within experimental error. Such a



continuous shift in the lattice parameters, along with the fact that no new peaks were observed with increasing sodium content, implies a solid-solution storage mechanism. The volume expansion between the pristine and fully discharge material was  $1.0 \pm 0.3\%$ . The electrochemical equation for sodium storage can hence be stated as equation (2.1), with  $x = 1$  referring to a theoretical capacity of  $49.5 \text{ mAh/g}$ . Please note that  $49.5 \text{ mAh/g}$  is regarded as the “theoretical capacity” of  $\text{Na}_2\text{Ti}_6\text{O}_{13}$  in this thesis based solely on storage of one mole of sodium per mole of  $\text{Na}_2\text{Ti}_6\text{O}_{13}$ . Since a pure  $\text{Na}_2\text{Ti}_6\text{O}_{13}$  electrode delivered  $42 \text{ mAh/g}$  during charge and since the as-synthesized compound contained about 91.5 % by weight of  $\text{Na}_2\text{Ti}_6\text{O}_{13}$ , it can be calculated that 1 g of the as-synthesized material should be able to deliver:  $0.915 \times 49.5 \approx 45.3 \text{ mAh}$  of capacity. This meant that about  $42/45.3 \approx 0.93$  moles of sodium were stored per mole of  $\text{Na}_2\text{Ti}_6\text{O}_{13}$  in the present study. Hence, equation (2.1) can be stated as follows:

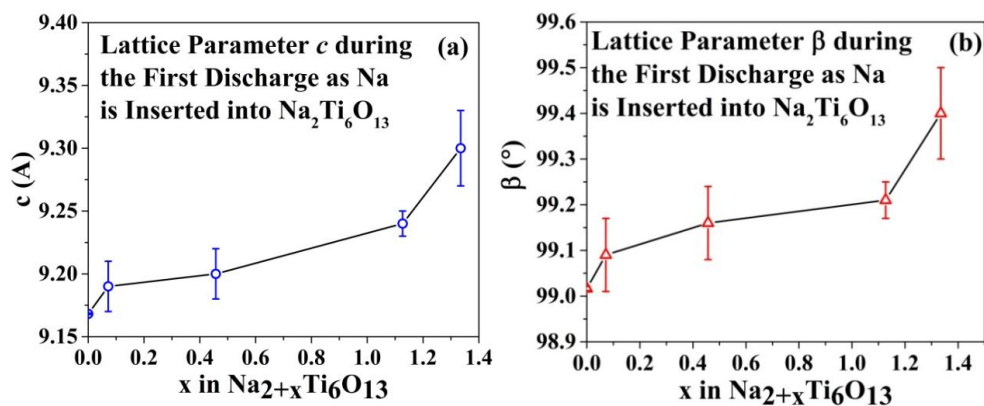
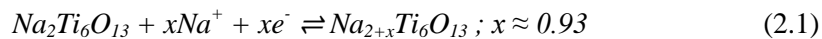


**Figure 2.6** | Effect on lattice parameters of  $\text{Na}_2\text{Ti}_6\text{O}_{13}$  by sodium incorporation as evaluated from *ex-situ* XRD data. The continuous change in the lattice parameters  $c$  and  $\beta$ , with increasing sodium insertion, is depicted in (a) and (b), respectively.

### 2.4.3 Electrochemical Cycling Performance

Figure 2.7a depicts stable cycling of the pure  $\text{Na}_2\text{Ti}_6\text{O}_{13}$  electrode over a wide range of  $C$  rates, from  $C/10$  to a fast  $20 C$  (3 min charge/discharge), and good retention when cycling is switched from high to low rate. Even when cycled at low  $C$  rates

where a greater percentage of the theoretical capacity was utilized (more than 80% at  $C/5$  rate), the cycling was very stable as exhibited by Fig. 2.7b. Figure 2.7c presents the long term cycling performance of the pure  $\text{Na}_2\text{Ti}_6\text{O}_{13}$  electrode at 1  $C$  rate exhibiting very stable cycling over 500 cycles and a stable coulombic efficiency ( $\text{CE}_{\text{ff}}$ ) exceeding 99%. These results demonstrate that the structure is able to reversibly withstand high current densities without collapsing over many cycles which is crucial in grid-storage applications as a way to counter power surges or support frequency regulation.<sup>3</sup> However, the observed capacity progressively decreased with increasing current density, pointing to the need for additive conducting agents.

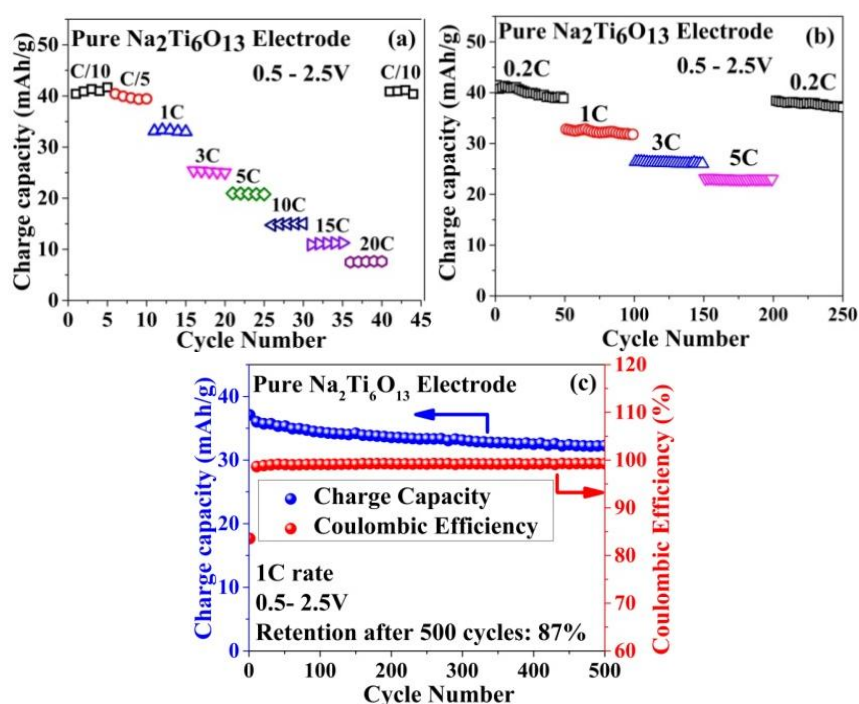


**Figure 2.7** | Cycling performance of pure  $\text{Na}_2\text{Ti}_6\text{O}_{13}$  electrode. Rate performance of a pure  $\text{Na}_2\text{Ti}_6\text{O}_{13}$  electrode from (a)  $C/10$  to 20  $C$  rate and (b) rate performance over 50 cycles each at  $C/5$ , 1, 3, 5  $C$  and back to  $C/5$ . Even at low  $C$  rates, where more than 80% of the theoretical capacity was obtained, the cycling was stable, indicative of the excellent reversibility of this material towards sodium intercalation/de-intercalation. (c) 500 cycles of a pure  $\text{Na}_2\text{Ti}_6\text{O}_{13}$  electrode showing the charge capacity and coulombic efficiency at 1  $C$  rate.

To enhance the high rate performance, carbon black (CB) conductive additive was used to prepare  $\text{Na}_2\text{Ti}_6\text{O}_{13}/\text{CB}$  composite electrodes. The first discharge of such a composite electrode resulted in almost 3 moles of Na insertion, yielding a capacity of 147  $\text{mAh/g}$ , while only 1.4 moles of Na (70  $\text{mAh/g}$ ) could be extracted in the first

charge (see Fig. 2.8a). Correlating the first cycles of the  $\text{Na}_2\text{Ti}_6\text{O}_{13}/\text{CB}$  composite and the pure  $\text{Na}_2\text{Ti}_6\text{O}_{13}$  electrodes, it can be concluded that the high surface area CB additives were responsible for the big ICL primarily due to the enhanced electrochemically active surface area resulting in greater irreversible charge consumption to form an SEI layer on the anode. The conductive additives also took part in the sodium storage, resulting in enhanced storage capacity of  $70 \text{ mAh/g}$  upon charge. This is supported by the Cyclic Voltammetry (CV) results shown in Fig. 2.8b. The first reduction (sodium intercalation) of the composite electrode displayed a big, broad peak around  $0.55 \text{ V}$ , which disappeared in subsequent cycles, consistent with the disappearance of the tail of the discharge plateau in the subsequent galvanostatic cycles (see Fig. 2.8a). Furthermore, this peak was not present in the first cycle CV curve of the pure  $\text{Na}_2\text{Ti}_6\text{O}_{13}$  electrode (refer to Fig. 2.8b). Hence, this big irreversibility can be attributed to the carbon black additive. Due to the facts that the fifth cycle of the  $\text{Na}_2\text{Ti}_6\text{O}_{13}/\text{CB}$  composite electrode displayed three times the reduction current and five times the oxidation current between  $0.7 - 0.5 \text{ V}$  compared to the corresponding processes in the fifth cycle of a pure  $\text{Na}_2\text{Ti}_6\text{O}_{13}$  electrode, it can be stated that the carbon black additives also take part in the sodium storage in this composite electrode. To calculate the fraction of CB contribution to the overall specific capacity, the observed charge capacity of a pure  $\text{Na}_2\text{Ti}_6\text{O}_{13}$  electrode can be correlated with that of a  $\text{Na}_2\text{Ti}_6\text{O}_{13}/\text{CB}$  composite electrode ( $42 \text{ mAh/g}$  vs  $70 \text{ mAh/g}$ , respectively). One can state that the extra  $28 \text{ mAh/g}$  capacity in the  $\text{Na}_2\text{Ti}_6\text{O}_{13}/\text{CB}$  composite electrode originated from the CB additives. Hence, the fraction of the CB to the total charge capacity of a  $\text{Na}_2\text{Ti}_6\text{O}_{13}/\text{CB}$  composite electrode was likely  $(28/70) \times 100 = 40 \%$ .

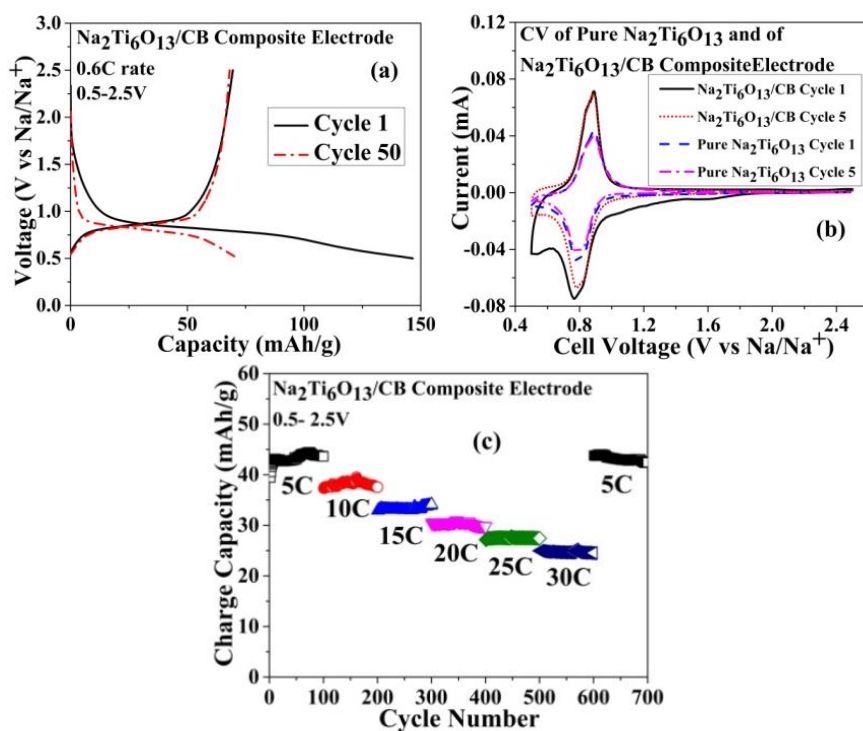


**Figure 2.8** | Cycling performance of Na<sub>2</sub>Ti<sub>6</sub>O<sub>13</sub>/CB composite electrode. (a) Galvanostatic cycling profiles of cycles 1 and 50 depicting the huge first discharge capacity with respect to a pure Na<sub>2</sub>Ti<sub>6</sub>O<sub>13</sub> electrode (see Fig. 2.5a). (b) Cyclic voltammograms of the first and the fifth cycles of a pure Na<sub>2</sub>Ti<sub>6</sub>O<sub>13</sub> and a Na<sub>2</sub>Ti<sub>6</sub>O<sub>13</sub>/CB composite electrode at a 0.05 mV/s scan rate. (c) Rate performance of a Na<sub>2</sub>Ti<sub>6</sub>O<sub>13</sub>/CB composite electrode at various rates.

The cycling performance of the Na<sub>2</sub>Ti<sub>6</sub>O<sub>13</sub>/CB composite electrode was similarly found to be very stable (refer to Fig. 2.8c), though the high ICL it displayed is a major limitation. To circumvent this, graphite was chosen as an alternate conductive additive since it is known that graphite cannot store appreciable amounts of sodium.<sup>50</sup> The first cycle ICL of a Na<sub>2</sub>Ti<sub>6</sub>O<sub>13</sub>/graphite composite electrode was significantly less than that of a Na<sub>2</sub>Ti<sub>6</sub>O<sub>13</sub>/CB composite electrode and quite close to that of a pure Na<sub>2</sub>Ti<sub>6</sub>O<sub>13</sub> electrode (see Fig. 2.9a). At low *C* rates, the Na<sub>2</sub>Ti<sub>6</sub>O<sub>13</sub>/graphite electrode performed similar to that of the pure Na<sub>2</sub>Ti<sub>6</sub>O<sub>13</sub> electrode. However, at high rates ( $\geq 5$  *C*), the composite electrode delivered enhanced performance: the delivered charge capacity at 20 *C* rate was more than double (refer Fig. 2.9b) compared to that of pure Na<sub>2</sub>Ti<sub>6</sub>O<sub>13</sub> electrode (see Fig. 2.7a). Moreover, even at an ultra-fast 30 *C* rate (2 min charge/discharge), the capacity was stable; when cycling was switched back to 5 *C* rate, 100% of the original 5 *C* capacity was obtained. Perez-Flores *et al.* have indicated that the intercalating sodium would likely reside in the central site between

the two existing sodium atoms within a hexatitanate unit tunnel.<sup>46</sup> The easiest way to access these sites would be along the *b*-axis tunnels. However, the excellent high rate capability achieved by the nanorods in the present study, with their *b*-axis tunnels oriented along the length (extending up to 0.5-2  $\mu\text{m}$ ), suggests that there may be a possibility of sodium ions accessing these sites from the *c*-axis (and hence, perpendicular to the length, which would result in high surface area exposed to the electrolyte). *Ab-initio* or atomistic simulation studies would help to clarify this observed storage performance.

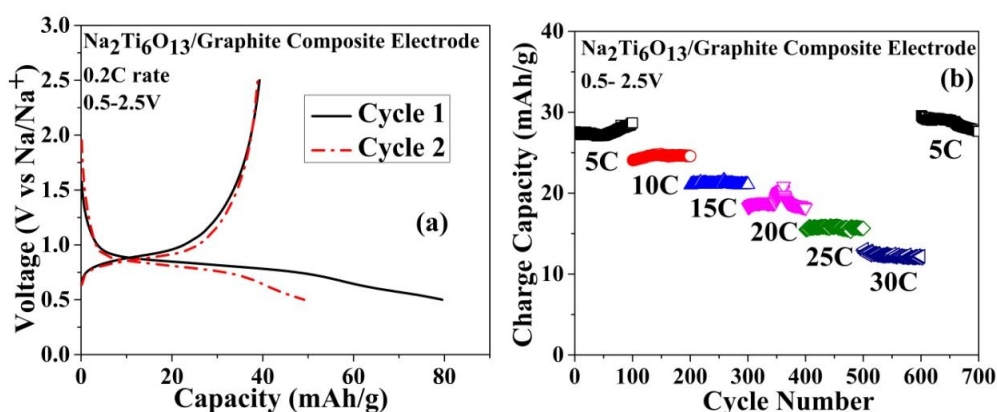


**Figure 2.9** | Cycling performance of Na<sub>2</sub>Ti<sub>6</sub>O<sub>13</sub>/graphite composite electrode. (a) Galvanostatic cycling profiles of cycles 1 and 2 illustrating that the irreversible capacity loss increases by only a small amount when graphite is used with respect to a pure Na<sub>2</sub>Ti<sub>6</sub>O<sub>13</sub> electrode (see Fig. 2.5a). (b) Rate performance of a Na<sub>2</sub>Ti<sub>6</sub>O<sub>13</sub>/graphite composite electrode at various rates.

Inspired by the stable cycling and good rate performance of this material, long-term cycling was undertaken. A Na<sub>2</sub>Ti<sub>6</sub>O<sub>13</sub>/CB composite electrode retained 78% of its initial capacity after 3,000 cycles at 20 C rate as shown in Fig. 2.10a. When mixed with graphite, the Na<sub>2</sub>Ti<sub>6</sub>O<sub>13</sub>/graphite composite electrode could be cycled for an impressive 5,000 cycles at 20 C with capacity retention of 85% of its initial value (see Fig. 2.10b). More importantly, the CE<sub>eff</sub> was observed to be at 98% throughout cycling. Furthermore, at a fast rate of 20 C, the composite electrodes still demonstrated similar plateau behaviour as that shown by their respective first cycles, even after long-term cycling, illustrating the robustness of the structure (refer to Fig. 2.10c and Fig. 2.10d). Such good cycle life can be attributed to the minimal volume change experienced by this material during sodium storage found by the *ex-situ* XRD

studies ( $\approx 1\%$ ). Though the theoretical capacity of  $\text{Na}_2\text{Ti}_6\text{O}_{13}$  is less, this is not of paramount importance for large-scale energy storage, such as micro-grids, which mainly require long cycle life, high rate capability and low cost demonstrated here.

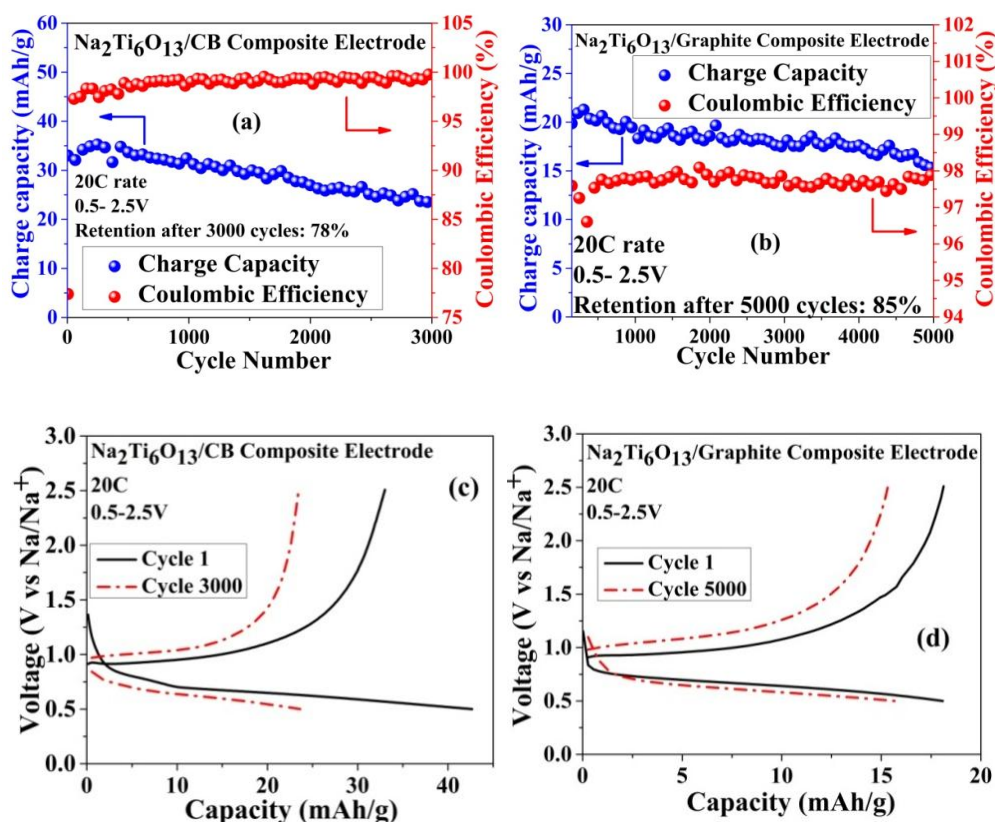


**Figure 2.10** | Long term cycling of  $\text{Na}_2\text{Ti}_6\text{O}_{13}$  with conductive additives at a fast 20 C (3 min charge/discharge) rate. (a) 3,000 cycles of a  $\text{Na}_2\text{Ti}_6\text{O}_{13}$ /CB composite electrode showing the charge capacity and coulombic efficiency. (b) 5,000 cycles of a  $\text{Na}_2\text{Ti}_6\text{O}_{13}$ /graphite electrode. Corresponding galvanostatic cycling curves of (c) cycles 1 and 3,000 of a  $\text{Na}_2\text{Ti}_6\text{O}_{13}$ /CB composite and (d) cycles 1 and 5,000 of a  $\text{Na}_2\text{Ti}_6\text{O}_{13}$ /graphite composite electrode. The plateau is clearly visible even after thousands of cycles, suggesting robustness of the electrodes upon long term cycling at high rates.

## 2.4.4 Application to Full Cells

A full cell of pure  $\text{Na}_2\text{Ti}_6\text{O}_{13}$  against  $\text{Na}_3\text{V}_2(\text{PO}_4)_2\text{F}_3/\text{C}$  cathode, prepared in-house, was fabricated as a proof-of-concept. As presented in Fig. 2.11a, the preliminary results of full cell cycling show a discharge plateau at an average voltage of 2.5 V with a capacity of 42 mAh/g at a C/5 rate and good cycling stability. Such a high voltage full cell would greatly increase the energy density of a future NIB. More impressively, a  $\text{Na}_3\text{V}_2(\text{PO}_4)_2\text{F}_3/\text{C} \parallel \text{Na}_2\text{Ti}_6\text{O}_{13}$  full cell can be cycled with excellent cycling stability and a stable  $\text{CE}_{\text{ff}}$  between 97 and 99 % for over 400 cycles at 1 C, as

illustrated in Fig. 2.11b. These results prove that  $\text{Na}_2\text{Ti}_6\text{O}_{13}$  can cycle in a full NIB in as stable a manner as it does in a half cell. With further optimization, a stable cycle life exceeding 5,000 cycles can be expected even for a full NIB.

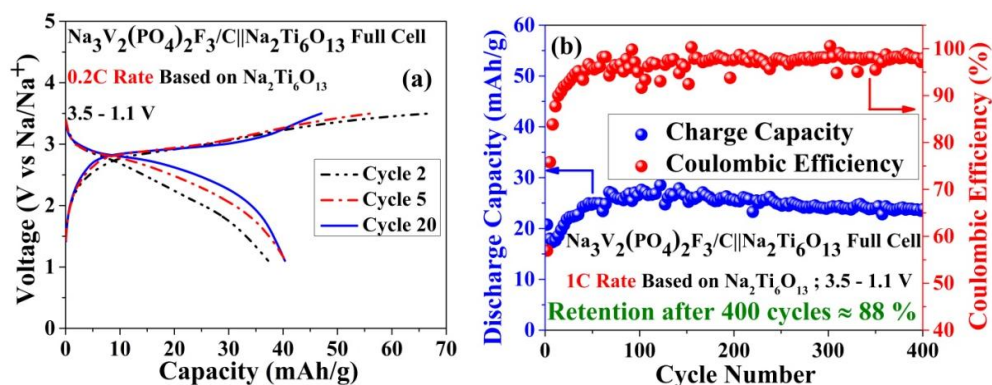


**Figure 2.11** | Illustration of  $\text{Na}_2\text{Ti}_6\text{O}_{13}$  being used as anode in a full NIB. (a) A pure  $\text{Na}_2\text{Ti}_6\text{O}_{13} \parallel \text{Na}_3\text{V}_2(\text{PO}_4)_2\text{F}_3/\text{C}$  full cell cycled at a  $C/5$  rate, between 3.5 – 1.1 V. A capacity of 42 mAh/g was obtained, and found to be stable, after 20 cycles. (b) 400 cycles of a pure  $\text{Na}_2\text{Ti}_6\text{O}_{13} \parallel \text{Na}_3\text{V}_2(\text{PO}_4)_2\text{F}_3/\text{C}$  full cell cycled at 1 C rate. Good capacity retention is obtained along with a high coulombic efficiency. The capacity is displayed with respect to the anode weight, as excess cathode was utilized in these full cells. The electrolyte used was 1M  $\text{NaClO}_4$  in EC:PC (1:1 volume ratio).

## 2.4.5 Stability of Sodiated $\text{Na}_2\text{Ti}_6\text{O}_{13}$

Another factor important for commercial application of  $\text{Na}_2\text{Ti}_6\text{O}_{13}$  in a NIB for grid storage applications is its stability in the sodiated state. Variable temperature XRD patterns on a fully discharged (to 0.5 V) pure  $\text{Na}_2\text{Ti}_6\text{O}_{13}$  electrode are presented in Fig. 2.12a. The sodiated  $\text{Na}_2\text{Ti}_6\text{O}_{13}$  phase was unaltered up to 500 °C, in contrast to the thermal instability of a carbon based anode.<sup>30</sup> To complement above study on thermal stability of the sodiated material, TGA experiment was carried out on the fully discharged electrode. The sodiated material could retain 82 % of its initial weight after 500 °C, with major weight losses taking place close to 93 and 310 °C, which could be attributed to traces of surface-adsorbed moisture during the sample transfer and melting of residual  $\text{NaClO}_4$  salt, respectively (see Fig. 2.12b).<sup>30</sup> While 18 % weight loss may appear to be huge, this can be explained due to the relative weight ratio of the residual  $\text{NaClO}_4$  salt with that of the weight of the sample on which TGA measurements were conducted. For this TGA experiment, about 2 mg of sodiated  $\text{Na}_2\text{Ti}_6\text{O}_{13}$  was taken. The electrolyte (1M  $\text{NaClO}_4$  in EC:PC) quantity was about 150

$\mu\text{l}$  in the coin cell. After opening of the cell, the sodiated powder was washed several times with PC solvent so as to remove the residual  $\text{NaClO}_4$  salt and then dried in vacuum. However, it can be calculated that  $150 \mu\text{l}$  of this electrolyte contained about  $18.4 \text{ mg}$  of  $\text{NaClO}_4$  salt. While washing was performed several times with PC, it is entirely possible that a fraction of this salt was not removed. If even 1-2 % of the salt remained, then that would translate to about  $0.184 - 0.368 \text{ mg}$ , which is 9-18 % by weight of the  $2 \text{ mg}$  powder sample we used for the TGA measurement, respectively. Despite this large contribution from the  $\text{NaClO}_4$  salt, the conclusions drawn from the TGA experiment, viz. the sodiated  $\text{Na}_2\text{Ti}_6\text{O}_{13}$  displayed negligible weight loss till  $500 \text{ }^\circ\text{C}$ , is still valid. Hence, we believe that  $\text{Na}_2\text{Ti}_6\text{O}_{13}$  has high thermal stability and is a safe anode material for NIB application.

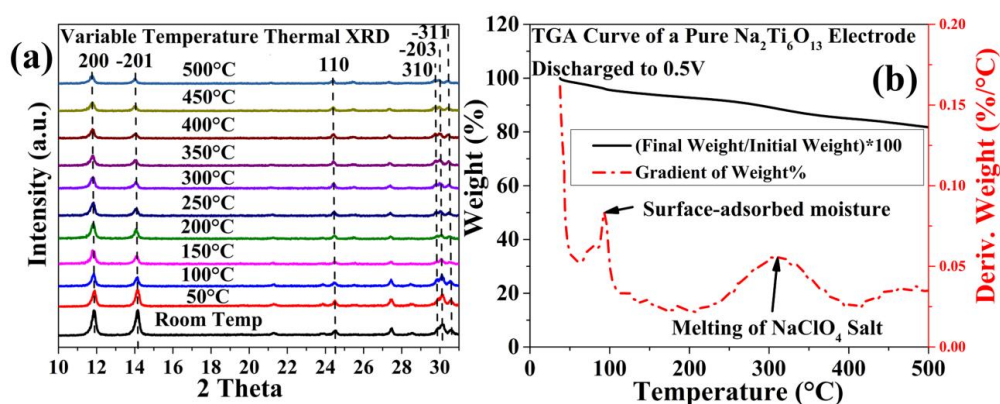


**Figure 2.12** | Stability of sodiated  $\text{Na}_2\text{Ti}_6\text{O}_{13}$ . (a) Variable temperature XRD of a pure  $\text{Na}_2\text{Ti}_6\text{O}_{13}$  electrode discharged to  $0.5 \text{ V}$  from room temperature to  $500 \text{ }^\circ\text{C}$ . Absence of new peaks indicates good thermal stability of the sodiated phase. (b) TGA curve of a pure  $\text{Na}_2\text{Ti}_6\text{O}_{13}$  electrode discharged to  $0.5\text{V}$  showing the loss of weight and its gradient. Majority of the weight loss takes place close to  $100$  and  $310 \text{ }^\circ\text{C}$ , which can be attributed to surface-adsorbed moisture and melting of residual  $\text{NaClO}_4$  salt, respectively. Hence, the sodiated  $\text{Na}_2\text{Ti}_6\text{O}_{13}$  material does not undergo much weight loss till  $500 \text{ }^\circ\text{C}$ .

## 2.5 Summary

We report here preparation of  $\text{Na}_2\text{Ti}_6\text{O}_{13}$  nanorods by a soft-template method. The obtained nanorods are able to reversibly store close to one mole of sodium even without conductive additives, through a solid-solution mechanism. The  $\text{Na}_2\text{Ti}_6\text{O}_{13}$ /graphite electrode can retain more than 85% of its capacity after 5,000 cycles, with almost 100% coulombic efficiency. A  $2.5 \text{ V}$  NIB fabricated using



$\text{Na}_2\text{Ti}_6\text{O}_{13}$  as anode against  $\text{Na}_3\text{V}_2(\text{PO}_4)_2\text{F}_3/\text{C}$  cathode cycled in a very stable manner over 400 cycles. The sodiated material was found to be stable up to 500 °C, as confirmed by TGA and variable temperature XRD studies, indicating its thermal safety. We have also introduced graphite as an effective conductive additive which does not cause a big ICL in the first cycle at least if the lower cut-off voltage is restricted to 0.5 V vs Na/Na<sup>+</sup>, thus circumventing a common problem while using carbon black as additive. We believe that the combination of low material cost, long and stable cycle life (> 5,000 cycles), good thermal stability and high efficiency make this environmental friendly material a possible anode for NIB application. Due to this material's outstanding high rate performance, its use for frequency regulation in grid storage would be quite appealing. However, due to its less capacity, its utilization towards load levelling applications may not be ideal; for those purposes, higher capacity materials may be better.



## Chapter 3 | The $\text{Na}_2\text{Ti}_3\text{O}_7 \rightleftharpoons \text{Na}_4\text{Ti}_3\text{O}_7$ Sodium

### Storage Pathway

---

The results described in this chapter have been published/presented in the following journals/conferences:

1. A. Rudola, N. Sharma and P. Balaya, *Electrochem. Commun.*, 2015, 61, 10-13
2. A. Rudola, K. Saravanan, C.W. Mason and P. Balaya, *J. Mater. Chem. A*, 2013, 1, 2653-2662
3. 8<sup>th</sup> International Conference on Materials for Advanced Technologies (ICMAT 2015), Singapore, July 2015 → Oral Presentation
4. 11<sup>th</sup> International Conference on Ceramic Materials and Components for Energy and Environmental Applications (CMCEE 2015), Vancouver, Canada, June 2015 → Oral Presentation
5. 1<sup>st</sup> International Symposium on Engineering Science, Singapore, May 2015 → Oral Presentation
6. 55<sup>th</sup> Battery Symposium in Japan, Kyoto, Japan, November 2014 → Oral Presentation
7. International Conference of Young Researchers on Advanced Materials (ICYRAM 2012), Singapore, July 2012 → Poster Presentation
8. 16<sup>th</sup> International Meeting on Lithium Batteries (IMLB 2012), Jeju, Korea, June 2012 → Poster Presentation

### 3.1 Preface to Chapter 3

The electrochemical properties of  $\text{Na}_2\text{Ti}_3\text{O}_7$  in a sodium battery are reported. Micrometre sized  $\text{Na}_2\text{Ti}_3\text{O}_7$  prepared from a solid-state synthesis was initially utilized to obtain a deeper understanding into the sodium storage properties of this material. A  $\text{Na}/\text{Na}_2\text{Ti}_3\text{O}_7$  cell displayed a theoretical charge capacity of  $178 \text{ mAh/g}$  at  $0.1 \text{ C}$  rate at a very low average voltage of  $0.3 \text{ V}$  vs  $\text{Na}/\text{Na}^+$ . High rate and long term cycling performance at different rates showed relatively stable storage capacities at high rates ( $5 \text{ C}$ ), but inadequate capacity retention at low rates such as  $0.1$  and  $0.2 \text{ C}$ . CV and GITT studies were used to obtain an insight into the kinetics of sodium insertion and extraction in  $\text{Na}_2\text{Ti}_3\text{O}_7$ . In particular, a relatively high value for the sodium chemical diffusion coefficient was obtained for  $\text{Na}_2\text{Ti}_3\text{O}_7$  estimated using GITT. Hence, sub-micrometric sized  $\text{Na}_2\text{Ti}_3\text{O}_7/\text{C}$  synthesized by a unique solvothermal synthesis demonstrated greatly improved high rate performance, up to  $40 \text{ C}$  (or  $1.5 \text{ min}$  response). The advantages and limitations of this material will be discussed in relation to its application to grid storage NIBs. Furthermore, two puzzling observations made during the course of this work would also be discussed.

## 3.2 Introduction

In the quest for higher capacity anode materials for NIB application, attention was focused on another sodium titanate phase,  $\text{Na}_2\text{Ti}_3\text{O}_7$ , whose crystal structure was also solved by Andersson and Wadsley.<sup>51</sup> This phase differs from that of  $\text{Na}_2\text{Ti}_6\text{O}_{13}$  in that it has a layered structure built up of three  $\text{TiO}_6$  octahedra which share two edges along one line above and below while simultaneously sharing corners, resulting in zigzag  $(\text{Ti}_3\text{O}_7)^{2-}$  layers, as depicted in Fig. 3.1. Within these layers, there are two different sodium sites.<sup>52, 53</sup> The sodium atoms form ionic bonds with the  $\text{TiO}_6$  octahedra, whereas the  $\text{TiO}_6$  octahedra innerlayers have strong covalent bonding, which leads to the stability of  $\text{Na}_2\text{Ti}_3\text{O}_7$ .<sup>52</sup>

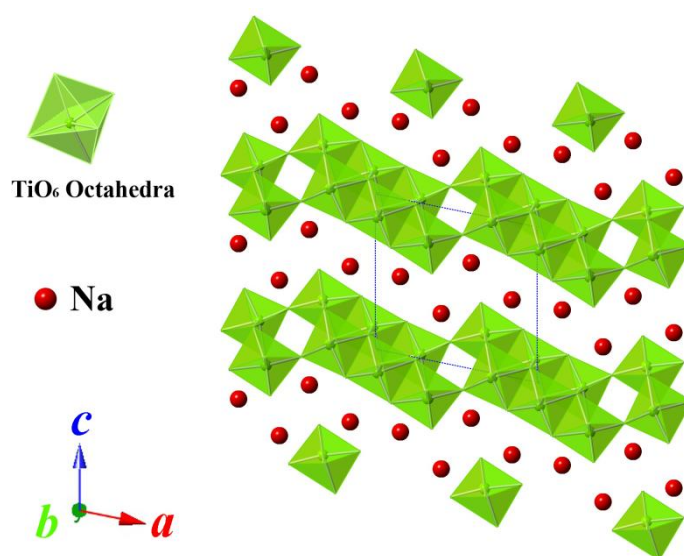


**Figure 3.1** | Crystal structure of  $\text{Na}_2\text{Ti}_3\text{O}_7$  when viewed along the  $b$ -axis demonstrating its layered structure. The  $b$ -axis is pointing perpendicularly out of the plane of the paper.

The layered structure of  $\text{Na}_2\text{Ti}_3\text{O}_7$  renders it useful for a host of diverse applications, such as a sensor,<sup>54</sup> photocatalyst<sup>55</sup> or radioactive waste removal.<sup>56</sup> Indeed, this material was recently shown to reversibly intercalate two moles of sodium through a two-phase reaction mechanism with a plateau centred at 0.3 V vs  $\text{Na}/\text{Na}^+$ , resulting in a capacity of 178 mAh/g.<sup>57</sup> After this first paper about the electrochemical activity of

$\text{Na}_2\text{Ti}_3\text{O}_7$  in a sodium battery, there have been only a handful of reports in the literature about the sodium storage performance of this material. While there is accurate knowledge about the structural changes taking place in  $\text{Na}_2\text{Ti}_3\text{O}_7$  upon two moles of sodium storage, none of the reports demonstrate adequate cycling stability.<sup>44, 58-62</sup> With the aim to understand the performance of  $\text{Na}_2\text{Ti}_3\text{O}_7$  in a sodium battery better, we present here the improved cell cycling and rate capability of  $\text{Na}_2\text{Ti}_3\text{O}_7$  prepared from a solid-state route using anatase- $\text{TiO}_2$  and  $\text{NaOH}$ . We provide evidence to explain the extremely long first discharge of the  $\text{Na}_2\text{Ti}_3\text{O}_7/\text{CB}$  (carbon black) composite electrode. We also report for the first time an interesting phenomenon relating to the appearance of a new charge plateau by raising the voltage window to 0.1 V from 0.01 V vs  $\text{Na}/\text{Na}^+$ . Further, CV and Galvanostatic Intermittent Titration Technique (GITT) studies on  $\text{Na}_2\text{Ti}_3\text{O}_7$  have been performed with the intention of understanding the kinetics of sodiation and de-sodiation within the  $\text{Na}_2\text{Ti}_3\text{O}_7/\text{CB}$  composite electrode.

After understanding the limitations imposed by the solid-state synthesis, we devised a new solvothermal synthesis route to obtain a more optimized morphology. This synthesis conducted in an ethanol medium is different from the established high-pressure syntheses techniques of  $\text{Na}_2\text{Ti}_3\text{O}_7$  generally reported in the literature which all focus on water as the reaction medium (hydrothermal synthesis).<sup>55, 63-65</sup> We demonstrate the best reported cycling performance of  $\text{Na}_2\text{Ti}_3\text{O}_7$ , thus far, which is shown to be a direct outcome of this synthesis. Finally, some important considerations concerning this material as an NIB anode will be discussed.

## **3.3 Experimental Section**

### **3.3.1 Synthesis**

#### **3.3.1.1 Solid-state Synthesis**

$\text{Na}_2\text{Ti}_3\text{O}_7$  was synthesized by the solid-state method. 1 g of anatase  $\text{TiO}_2$  prepared by

the soft-template method<sup>66</sup> and 0.36 g of NaOH (Alfa Aesar), corresponding to a slight excess of NaOH with regard to the molar stoichiometry ( $\text{NaOH}:\text{TiO}_2 = 1:1.5$ ), were ball-milled in a planetary ball mill at 400 rpm for 4 h. The obtained powder was then calcined in air at 750 °C for 20 h.

### 3.3.1.2 Solvothermal Synthesis

$\text{Na}_2\text{Ti}_3\text{O}_7$  was synthesized using a solvothermal approach. The sodium and titanium sources were sodium hydroxide and titanium isopropoxide respectively. They were taken in stoichiometric molar ratio with a 20% molar excess of the former. Gluconic acid lactone was used as the *in-situ* carbon source and absolute ethanol served as the medium. The reaction was carried out in a Teflon<sup>®</sup> vessel sealed in a stainless steel autoclave at 180 °C for 6 h and allowed to cool naturally. The resulting solution with precipitates was centrifuged once with absolute ethanol and then dried in an oven kept at 70 °C for 4 h. The obtained orange-light brown powder was then calcined at 800 °C for 4 h under argon gas flow in a tube furnace. The resulting black powder was the desired  $\text{Na}_2\text{Ti}_3\text{O}_7$  phase embedded in a carbon matrix (referred to as “ $\text{Na}_2\text{Ti}_3\text{O}_7/\text{C}$ ”).

## 3.3.2 Synthesized Powder Characterization

### 3.3.2.1 Solid-state Synthesized $\text{Na}_2\text{Ti}_3\text{O}_7$

PXRD patterns were recorded using a D5005 Bruker X-ray diffractometer equipped with Cu K $\alpha$  radiation. The accelerating voltage and current were 40 kV and 40 mA, respectively. A scan speed of 0.015 °/s was used to record the PXRD patterns. Lattice parameters were obtained using TOPAS-R (version 3.0) software. The morphology of the product was examined using FESEM (model JEOL JSM-7000F) operated at 15 kV and 20 mA and HRTEM (model JEOL JEM-2010). For FESEM examination, the sample surface was sputtered with a thin platinum coating. For HRTEM studies, the sample was dispersed in ethanol by sonication, a drop was loaded on Cu-grid and

dried. X-ray Photoelectron Spectroscopy (XPS) studies were performed with a Kratos AXIS Ultra<sup>DVD</sup> (Kratos Analytical Ltd) at a base pressure of  $1 \times 10^{-9}$  Torr and a working pressure of  $5 \times 10^{-9}$  Torr with a mono Al K $\alpha$  radiation.

### **3.3.2.2 Solvothermal Synthesized Na<sub>2</sub>Ti<sub>3</sub>O<sub>7</sub>**

PXRD patterns were acquired on the as-synthesized Na<sub>2</sub>Ti<sub>3</sub>O<sub>7</sub>/C powder in the  $2\theta$  range of  $8-70^\circ$  with a Bruker AXS D8 ADVANCE powder diffractometer using Cu K $\alpha$  radiation source and operated at 25 mA and 40 kV. Rietveld refinement was conducted with the TOPAS academic version 4.2 software. TGA was conducted by a TA instrument 2960 in air where the sample was heated from room temperature to 750 °C with a 10 °C /min ramp rate. FESEM images were obtained using a JEOL JSM-7000F instrument operated at 20 mA and 15 kV. For the TEM, HRTEM and SAED experiments, the as-prepared powder was sonicated in ethanol and then loaded on a Cu grid. The prepared sample was then transferred to the JEOL TEM-2010 instrument for data collection. N<sub>2</sub> physisorption using a NOVA 1200 Quantachrome apparatus was utilized to collect the Brunauer-Emmett-Teller (BET) surface area and the Barrett-Joyner-Halenda (BJH) pore-size distribution. Prior to measurements, the Na<sub>2</sub>Ti<sub>3</sub>O<sub>7</sub>/C powder was dried in vacuum at 110 °C.

### **3.3.3 Electrochemical Characterization**

#### **3.3.3.1 Solid-state Synthesized Na<sub>2</sub>Ti<sub>3</sub>O<sub>7</sub>**

For sodium storage studies, composite electrodes were fabricated with the active material, Super P carbon black CB, and PVDF binder (Kynar 2801) in the weight ratio 70:20:10 using NMP as solvent. In all electrochemical tests, unless otherwise mentioned, the active material was ball-milled with CB at 400 rpm for 20 min using a FRITSCH Planetary Micro Mill PULVERISETTE 7 premium line ball mill with the balls made of Zirconia. The obtained slurry was coated uniformly on an etched copper foil (15  $\mu$ m thick) using a doctor blade. The coated slurry was then dried at



110 °C under vacuum for 12 h. The dried slurry was pressed using a twin roller at a pressure of 37 psi to ensure close contact between the composite electrode materials and the current collector. The pressed electrodes were cut into circular discs of 16 mm diameter and consequently dried overnight at 110 °C in an argon filled chamber. Sodium metal foil (Merck), 1 M NaClO<sub>4</sub> in EC (Alfa Aesar) and propylene carbonate PC (1:1 v/v) and Whatman Glass Microfibre Filter (Grade GF/F) were used as counter electrode, electrolyte and separator, respectively, to assemble coin-type cells (size 2016) in an argon filled glove box (MBraun, Germany). The geometrical area of the electrode was 2.0 cm<sup>2</sup>. The active material content in the electrode was around 1.5 mg. Charge–discharge cycling at a constant current mode was carried out using a computer controlled Arbin battery tester (Model, BT2000, USA) and CV and GITT studies were carried out at room temperature using a computer controlled VMP3 battery tester (Bio-logic, France) in the voltage window 0.01 – 2.5 V. For the GITT studies, a current pulse was applied for 10 min at 0.2 C rate and a relaxation period of 2 h was given, unless the system attained equilibrium earlier.

### 3.3.3.2 Solvothermal Synthesized Na<sub>2</sub>Ti<sub>3</sub>O<sub>7</sub>

Composite electrodes were made with Na<sub>2</sub>Ti<sub>3</sub>O<sub>7</sub>/C: Super P carbon: sodium salt of carboxymethyl cyellulose (CMC) in the weight ratio 80:10:10. First, required weights of Na<sub>2</sub>Ti<sub>3</sub>O<sub>7</sub>/C and Super P carbon black were added to CMC-water solution. The resulting slurry was thoroughly mixed and then coated on an etched aluminium foil by the doctor blade method. The coated slurry was allowed to dry under vacuum for 12 h at 110 °C, before being pressed by a twin roller at a pressure of 37 psi. The final electrode loading of Na<sub>2</sub>Ti<sub>3</sub>O<sub>7</sub> (excluding the *in-situ* carbon) was between 1.5 – 2.0 mg/cm<sup>2</sup>. These composite electrodes were used as the working electrode to construct three-electrode and two-electrode cells. For the three-electrode cells, sodium metal disk served as the counter electrode (CE) and a sodium metal ring served as the reference electrode (RE). Commercial three-electrode cells provided by MTI (model

number EQ-3ESTC15) were used. For the two-electrode cells, sodium metal disk served as the counter and reference electrodes, in a 2016-type coin cell. All cells were fabricated inside an Argon-filled glove box. 1M NaClO<sub>4</sub> in EC:PC (1:1 v/v), prepared in-house from commercially available NaClO<sub>4</sub> and solvents, was used as the electrolyte. The two-electrode cells were cycled on an Arbin battery tester (model BT2000, USA) while the three-electrode cells were cycled with a VMP3 instrument (Bio-Logic, France).

## 3.4 Results and Discussion

### 3.4.1 Solid-state Na<sub>2</sub>Ti<sub>3</sub>O<sub>7</sub> Powder Characterization

Synthesis reaction parameters including effects of (1) temperature and (2) time on two different sodium precursors have been optimised to establish the factors that govern the formation of pure Na<sub>2</sub>Ti<sub>3</sub>O<sub>7</sub>. Figure 3.2 presents the PXRD pattern of the as-synthesized Na<sub>2</sub>Ti<sub>3</sub>O<sub>7</sub> under different calcination temperatures and times using NaOH as the sodium precursor. A calcination temperature of 650 °C was first attempted for two time intervals of 20 and 40 h. The crystalline phase obtained in this temperature did not match with any known standard JCPDS pattern. This phase is probably an intermediate phase to Na<sub>2</sub>Ti<sub>3</sub>O<sub>7</sub>. No significant electrochemical activity was detected with this intermediate phase.

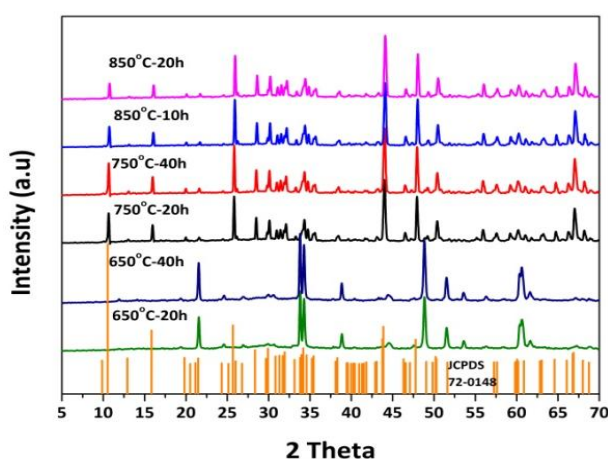


**Figure 3.2** | Comparison of PXRD patterns with different calcination temperatures and times using NaOH and anatase-TiO<sub>2</sub> as precursors.

When the calcination temperature was increased to 750 °C for 20 and 40 h, the diffraction patterns clearly matched the Na<sub>2</sub>Ti<sub>3</sub>O<sub>7</sub> pattern (JCPDS - 72-0148) revealing monoclinic phase formation with space group P121/m<sub>1</sub>, consistent with the PXRD pattern obtained by Senguttuvan *et al.*<sup>57</sup> The increase in the calcination time from 20 to 40 h at the same temperature (750 °C) did not alter the phase purity.

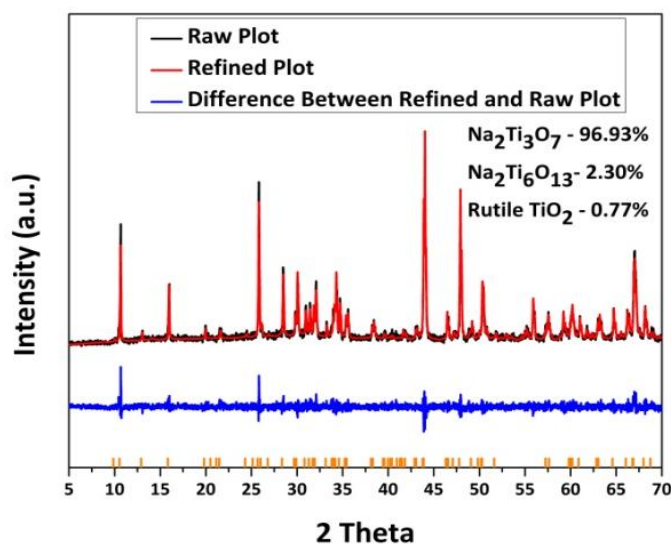


**Figure 3.3** | Rietveld Refinement of the PXRD Data for the Na<sub>2</sub>Ti<sub>3</sub>O<sub>7</sub> sample sintered at 750 °C for 20 h.

Figure 3.3 presents the Rietveld refinement of the PXRD pattern obtained from the sample calcined at 750 °C for 20 h. The analysis suggested trace impurities of Na<sub>2</sub>Ti<sub>6</sub>O<sub>13</sub> (2.3%) and rutile TiO<sub>2</sub> (0.77%) along with formation of Na<sub>2</sub>Ti<sub>3</sub>O<sub>7</sub>. Table 2.1 shows relevant parameters obtained from the refinement. The lattice parameters (*a*, *b*, *c*, *β* and *V*) values obtained are in good agreement with published results.<sup>52, 57</sup>

**Table 3.1** | Rietveld refinement parameters for Na<sub>2</sub>Ti<sub>3</sub>O<sub>7</sub> calcined at 750 °C for 20 h.

Space Group	<i>a</i> (Å)	<i>b</i> (Å)	<i>c</i> (Å)	<i>β</i> (°)	Volume (Å <sup>3</sup> )	R-Bragg	R <sub>wp</sub>	χ <sup>2</sup>
P121/m <sub>1</sub>	8.565	3.802	9.128	101.589	291.181	3.551	16.76	1.16

Further increasing the calcination temperature to 850 °C resulted in a qualitatively similar PXRD pattern which was obtained at 750 °C. However, Rietveld refinement

showed that the  $\text{Na}_2\text{Ti}_3\text{O}_7$  phase decreased to 95.15% for 850 °C- 10 h and further to 82.63% for the 850 °C- 40 h calcination conditions.

To examine the effect of a different precursor,  $\text{Na}_2\text{Ti}_3\text{O}_7$  was synthesized using sodium acetate as a sodium precursor under identical conditions. Figure 3.4 provides the PXRD patterns of the compound synthesized using  $\text{CH}_3\text{COONa}$  and anatase  $\text{TiO}_2$ . At 650 °C, the identical unknown phase was observed, as with NaOH precursor. At 750 °C, the PXRD pattern seemed to be similar to  $\text{Na}_2\text{Ti}_3\text{O}_7$  but with impurities present. At 850 °C, a pure phase was obtained. In fact, Rietveld refinement suggests that the sample prepared at 850 °C- 20 h was 97.9% pure. Interestingly, the purity of that calcined at 850 °C-10 h was only 85.27%. This trend is opposite to that observed with the NaOH precursor; the sample prepared at 850 °C-10 h is purer than that at 850 °C-20 h. Since a pure phase of  $\text{Na}_2\text{Ti}_3\text{O}_7$  was obtained at a lower temperature with the NaOH precursor, it was used for further investigations.

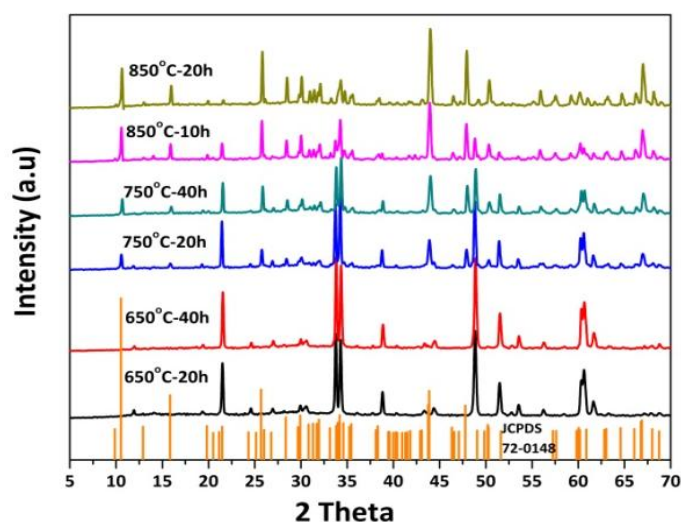


**Figure 3.4** | PXRD patterns obtained for the  $\text{CH}_3\text{COONa}$  precursor at different calcination temperatures and times.

The FESEM images of the as-prepared  $\text{Na}_2\text{Ti}_3\text{O}_7$  samples are shown in Fig. 3.5. The microstructure consisted of plate like agglomerates in the range of 5-50  $\mu\text{m}$ . A higher magnification image revealed that each agglomerate consisted of small platelets of length 1-2  $\mu\text{m}$  with thickness of 0.1-0.2  $\mu\text{m}$ .

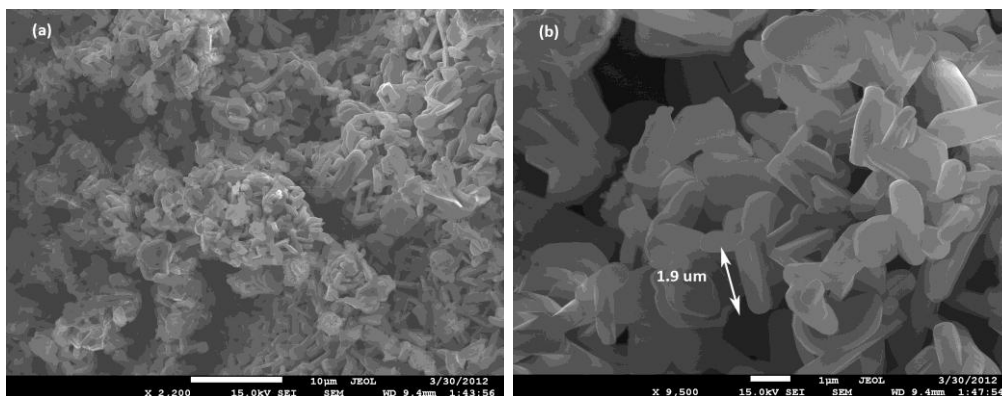


**Figure 3.5** | FESEM images of  $\text{Na}_2\text{Ti}_3\text{O}_7$  calcined at  $750^\circ\text{C}$  for  $20\text{ h}$ . (a) FESEM image at magnification of  $\times 2200$  and (b) at magnification of  $\times 9500$ .

To further explore the morphology, TEM, HRTEM and SAED analysis were carried out on the  $\text{Na}_2\text{Ti}_3\text{O}_7$  sample (see Fig. 3.6). The platelets of thickness in the nanometre range can be seen from the TEM image (Fig. 3.6a), while the HRTEM image (Fig. 3.6b) clearly shows lattice fringes indicating the single crystalline nature of the platelets. The width ( $0.84\text{ nm}$ ) of neighbouring lattice fringes corresponds to the (100) plane of  $\text{Na}_2\text{Ti}_3\text{O}_7$ . The SAED pattern depicted in Fig. 3.6c demonstrates the highly crystalline characteristic of the as-prepared  $\text{Na}_2\text{Ti}_3\text{O}_7$  platelets. Various planes corresponding to the  $\text{Na}_2\text{Ti}_3\text{O}_7$  have been indexed in Fig. 3.6c which is consistent with the PXRD pattern results shown in Fig. 3.2.

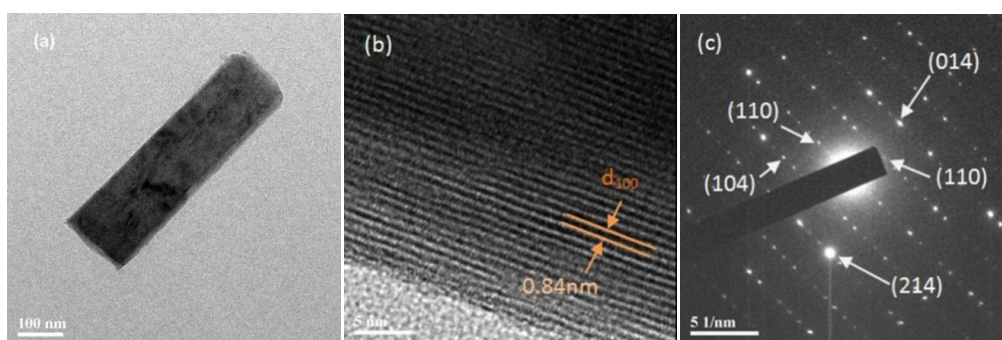


**Figure 3.6** | Morphology characterization of the as-prepared  $\text{Na}_2\text{Ti}_3\text{O}_7$  from the solid-state method. (a) TEM image obtained of a nanometer sized  $\text{Na}_2\text{Ti}_3\text{O}_7$  particle. (b) HRTEM image of a single  $\text{Na}_2\text{Ti}_3\text{O}_7$  platelet and (c) SAED pattern of the sample shown in (a) and (b).

XPS is a non-destructive technique well-suited for the evaluation of valence states of metal/non-metal ions and extensively used in the characterization of electrode materials. The binding energy values for the as-synthesized  $\text{Na}_2\text{Ti}_3\text{O}_7$  powder are

summarized in Table 2.2. The high resolution XPS spectrum for Ti 2p is depicted in Fig. 3.7. The binding energy of 458.2 eV obtained for the Ti 2p doublet is very similar to previously reported values.<sup>67</sup> This confirms that the oxidation state of the titanium ions in the pristine powder is Ti<sup>4+</sup>.<sup>68-70</sup> The binding energy values of 1071.05 eV for the Na 1s peak and of 529.85 eV for the O1s peak are also consistent with the literature.<sup>67, 68, 71</sup>

**Table 3.2** | XPS Results of the as synthesized Na<sub>2</sub>Ti<sub>3</sub>O<sub>7</sub> powder.

State	Na 1s	Ti 2P	O 1s
Binding energy (eV)	1071.05	458.2	529.85
Atomic percentage	15.15	19.79	65.06

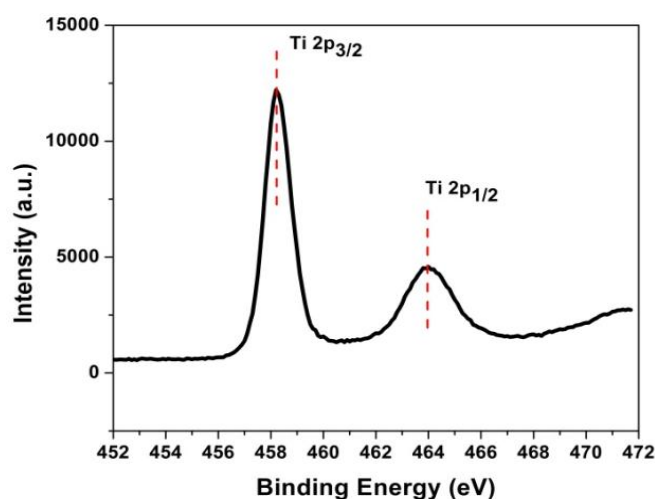


**Figure 3.7** | High resolution spectra for Ti 2p of as-prepared Na<sub>2</sub>Ti<sub>3</sub>O<sub>7</sub> powder.

EDX mapping showed no impurity elements. All three elements- Na, Ti and O- were found to be present uniformly throughout the bulk of the sample (Fig. 3.8).

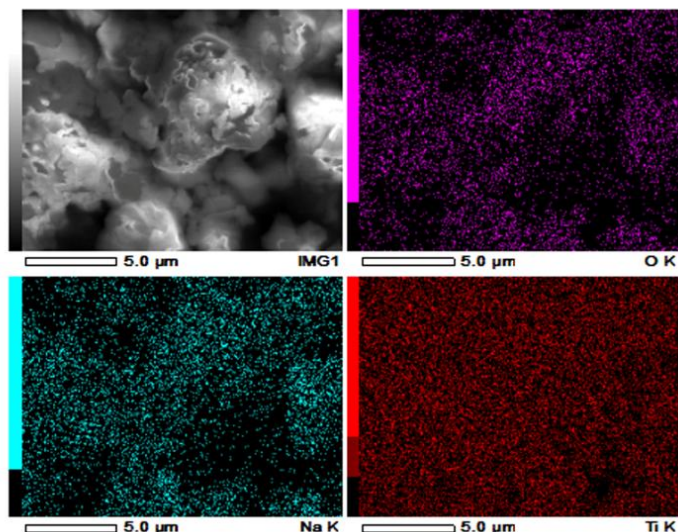


**Figure 3.8** | FESEM examination along with elemental mapping (EDX) for the elements Na, Ti and O for the as-synthesized  $\text{Na}_2\text{Ti}_3\text{O}_7$ . No other impurity elements were detected. The mapped cyan, red and pink regions correspond to Na, Ti and O, respectively. The elemental mapping demonstrates a uniform distribution of elements throughout the volume of the sample analyzed.

## 3.4.2 Electrochemical Properties of Solid-state $\text{Na}_2\text{Ti}_3\text{O}_7$

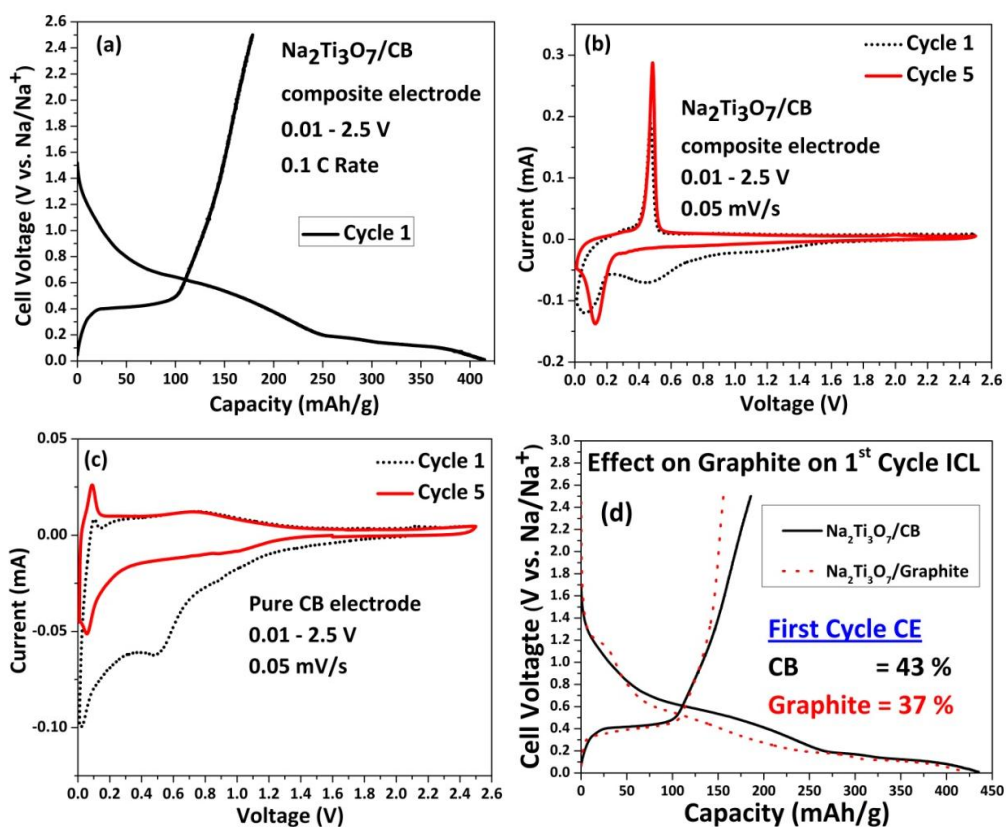
### 3.4.2.1 First Cycle Irreversibility

Figure 3.9a presents the first discharge and the first charge of the ball-milled  $\text{Na}_2\text{Ti}_3\text{O}_7/\text{CB}$  composite electrode against Na metal at 0.1  $C$  rate (current value corresponding to two moles of sodium storage per mole of  $\text{Na}_2\text{Ti}_3\text{O}_7$  in 10  $h$  according to a theoretical capacity of 178  $\text{mAh/g}$ ) over a voltage window 0.01 - 2.5  $V$ . The first discharge consists of several plateaus, consistent with the earlier report.<sup>57</sup> Among these discharge plateaus, only the one at 0.2  $V$  is seen upon subsequent cycling (refer to Fig. 3.10, discussed in the following section). To understand this long first discharge and the various plateaus for the  $\text{Na}_2\text{Ti}_3\text{O}_7/\text{CB}$  composite electrode, CV studies were performed on both  $\text{Na}_2\text{Ti}_3\text{O}_7/\text{CB}$  (Fig. 3.9b) and pure CB (Fig. 3.9c) electrodes. Referring to Fig. 3.9b, it can be seen that the first cycle reduction (*i.e.*, Na-intercalation) process consists of two peaks: a broad peak at 0.45  $V$  and a sharper peak at 0.07  $V$ . On subsequent cycling, the 0.45  $V$  reduction peak

vanishes completely while the 0.07 V reduction peak intensifies and shifts to 0.13 V. The first cycle oxidation process has a big, prominent peak at 0.47 V which does not alter upon cycling. On comparing this with the CV of the pure CB electrode, the broad first cycle reduction peak around 0.45 V is in good agreement with the first reduction peak obtained with the composite electrode. This 0.45 V peak for the pure carbon black electrode vanished upon cycling, similar to the case for the Na<sub>2</sub>Ti<sub>3</sub>O<sub>7</sub>/CB composite electrode. This fact suggests that the long first discharge observed for the Na<sub>2</sub>Ti<sub>3</sub>O<sub>7</sub>/CB composite electrode was not due to irreversible sodium storage in Na<sub>2</sub>Ti<sub>3</sub>O<sub>7</sub>. Interestingly, the oxidation peak of 0.10 V for the carbon black electrode did not appear in the CV curve of the Na<sub>2</sub>Ti<sub>3</sub>O<sub>7</sub>/CB composite electrode. This fact implies that the carbon additive does not take part in the sodium storage during the oxidation process.

In addition, the formation of a SEI also contributes to the first cycle irreversibility, as electrolyte decomposition takes place at such reducing voltages.<sup>29, 30, 41</sup> It was demonstrated in the previous chapter that graphite as a conductive additive helped mitigate the first cycle ICL in a Na<sub>2</sub>Ti<sub>6</sub>O<sub>13</sub>/graphite composite electrode.<sup>72</sup> However, a Na<sub>2</sub>Ti<sub>3</sub>O<sub>7</sub>/graphite composite electrode resulted in greater ICL in the first cycle, largely brought about due to lesser charge capacity of 156 mAh/g in comparison to that of a Na<sub>2</sub>Ti<sub>3</sub>O<sub>7</sub>/CB composite electrode (refer to Fig. 3.9d). It appears graphite as a conductive additive is effective in controlling the ICL if the lower cut-off voltage window is 0.5 V vs Na/Na<sup>+</sup> (as was the case for Na<sub>2</sub>Ti<sub>6</sub>O<sub>13</sub>), but does not appear to influence the ICL if deep discharged down to 0.01 V. Hence, further electrochemical tests were conducted on a Na<sub>2</sub>Ti<sub>3</sub>O<sub>7</sub>/CB composite electrode.

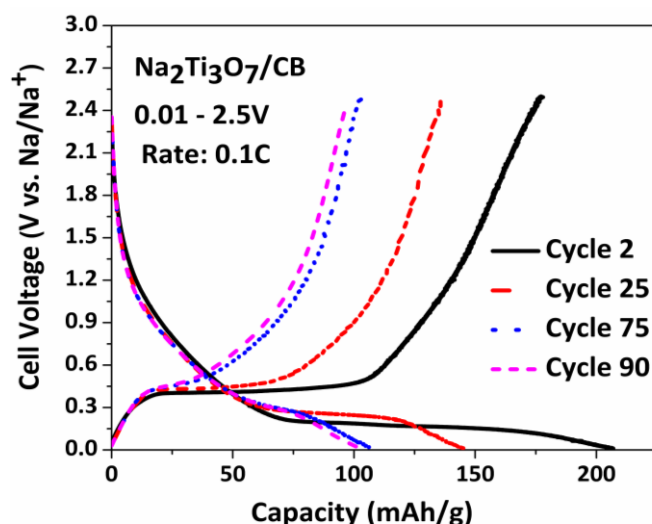




**Figure 3.9** | Investigation into the ICL during the first cycle of a Na<sub>2</sub>Ti<sub>3</sub>O<sub>7</sub>/CB composite electrode. (a) First discharge and subsequent charge of a Na<sub>2</sub>Ti<sub>3</sub>O<sub>7</sub>/CB composite electrode at 0.1 C. (b) CV graph at a scan rate of 0.05 mV/s of a coin cell with a Na<sub>2</sub>Ti<sub>3</sub>O<sub>7</sub>/CB composite electrode. (c) CV graphs at a scan rate of 0.05 mV/s of a coin cell with an electrode consisting of pure carbon black along with binder. (d) Comparison of the first cycle of a Na<sub>2</sub>Ti<sub>3</sub>O<sub>7</sub>/graphite and Na<sub>2</sub>Ti<sub>3</sub>O<sub>7</sub>/CB composite electrodes at identical C/5 rates. The same electrode composition was used for both composite electrodes (Na<sub>2</sub>Ti<sub>3</sub>O<sub>7</sub>: Graphite/Super P CB: PVDF = 70:20:10). Less charge capacity was obtained with slightly more ICL when graphite was used as a conductive additive.

### 3.4.2.2 Long Term Cycling and Rate Performance

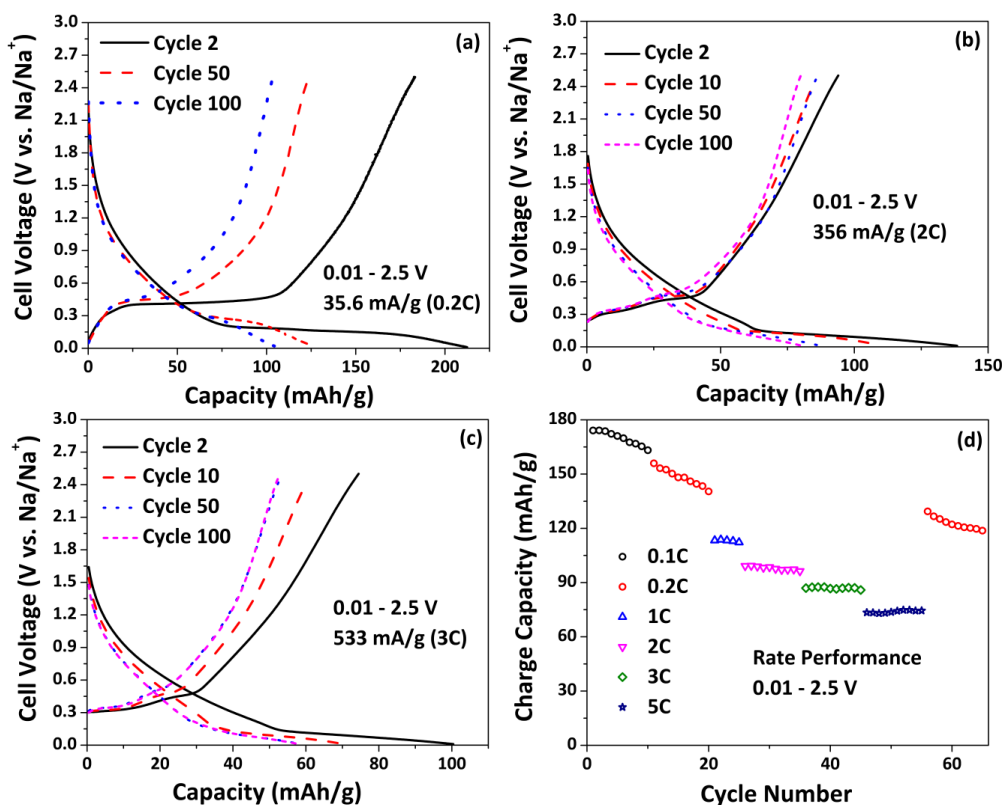
From Open Circuit Voltage (OCV), the cell was first discharged and subsequently charged to obtain a first charge capacity of 178 mAh/g corresponding to two moles of sodium (refer Fig. 3.9a). Figure 3.10 provides the galvanostatic charge - discharge cycling curves of the Na<sub>2</sub>Ti<sub>3</sub>O<sub>7</sub>/CB composite electrode from second cycle onwards. The cycling consists of a discharge plateau at 0.2 V and a charge plateau at 0.4 V. It is interesting to note that the CE<sub>ff</sub> of second discharge (205 mAh/g) and charge (177 mAh/g) cycle is about 87% indicating that SEI formation takes place beyond the first cycle as well. Upon cycling, the capacity retention was found to slightly decrease but at the end of the 90<sup>th</sup> cycle the capacity stabilized to 98 mAh/g.



**Figure 3.10** | Cycling of  $\text{Na}_2\text{Ti}_3\text{O}_7$  electrode with 20% carbon black and 10% binder at 0.1  $C$  rate showing charge-discharge curves for cycles 2, 25, 75 and 90 in the voltage window of 0.01 – 2.5V.

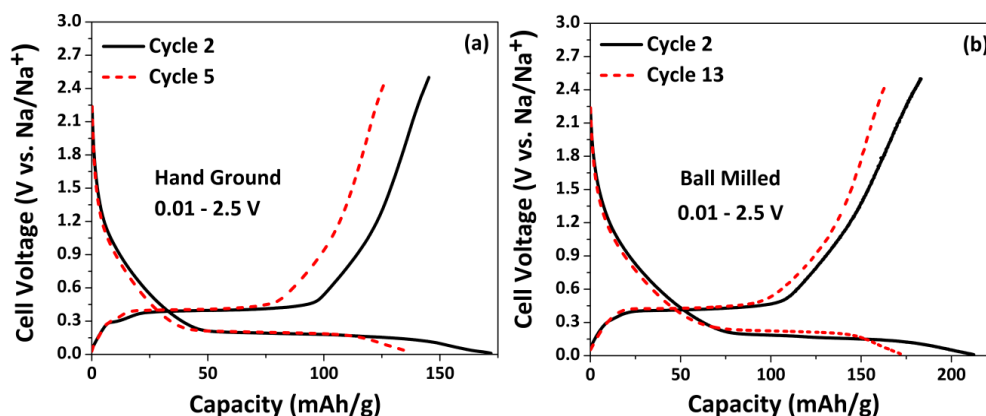
The long term cycling performance of the as-synthesized  $\text{Na}_2\text{Ti}_3\text{O}_7$  at various rates is shown in Fig. 3.11a, Fig. 3.11b and Fig. 3.11c. A first charge capacity of 185.6, 97.9 and 80.2  $\text{mAh/g}$  could be obtained at 0.2, 2 and 3  $C$  rates respectively. The capacity fading tended to decrease as the rate of cycling increased. This declining capacity at high  $C$  rates hints that the rate limiting step for this material could be diffusion, since the  $\text{Na}^+$  ions have insufficient time to intercalate and de-intercalate at high  $C$  rates. This fact will be discussed in section 3.4.2.5.

The rate performance of the  $\text{Na}_2\text{Ti}_3\text{O}_7/\text{CB}$  composite electrode is summarized in Fig. 3.11d. The cell was cycled at six different rates of 0.1, 0.2, 1, 2, 3 and 5  $C$  in the voltage window 0.01-2.5 V. As expected, the charge capacity decreases from 175  $\text{mAh/g}$  at 0.1  $C$  rate to about 71  $\text{mAh/g}$  at 5  $C$  rate, again implying a diffusion limited  $\text{Na}^+$  ion mass transport. Upon decreasing the current from 5  $C$  to 0.2  $C$ , 130  $\text{mAh/g}$  (which is about 93% of the initial 0.2  $C$  capacity) was obtained. This demonstrates good capacity retention and flexibility when operating conditions switch from high to low rates.



**Figure 3.11** | Long term cycling and rate performance of a  $\text{Na}_2\text{Ti}_3\text{O}_7/\text{CB}$  composite electrode at various rates. (a) Cell Cycling of  $\text{Na}_2\text{Ti}_3\text{O}_7/\text{CB}$  electrode at 0.2 C. (b) Cycling at 2 C rate, (c) Cycling at 3 C rate and (d) Rate performance of  $\text{Na}_2\text{Ti}_3\text{O}_7/\text{CB}$  electrode. All cells cycled in a voltage window of 0.01-2.5 V.

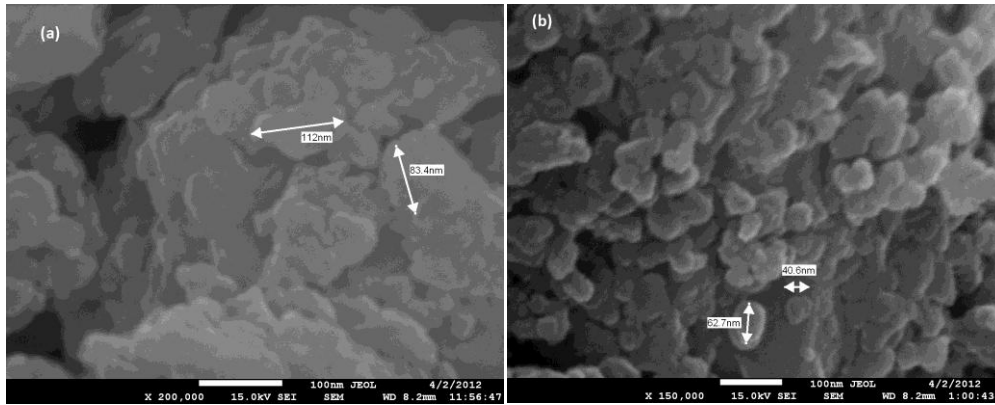
### 3.4.2.3 Effect of Ball-milling on Cycling Performance



**Figure 3.12** | Effect of ball-milling on cycling performance. Cycling at 0.2 C rate of (a) active material hand ground with carbon black and (b) active material ball-milled with carbon.

Figure 3.12 provides a comparison of the electrodes prepared by hand grinding with that using a planetary ball mill. Less charge capacity is obtained with greater fading if the sample is hand ground with CB. The better performance obtained for the ball-milled sample implies particle size reduction. Indeed, this was confirmed by FESEM

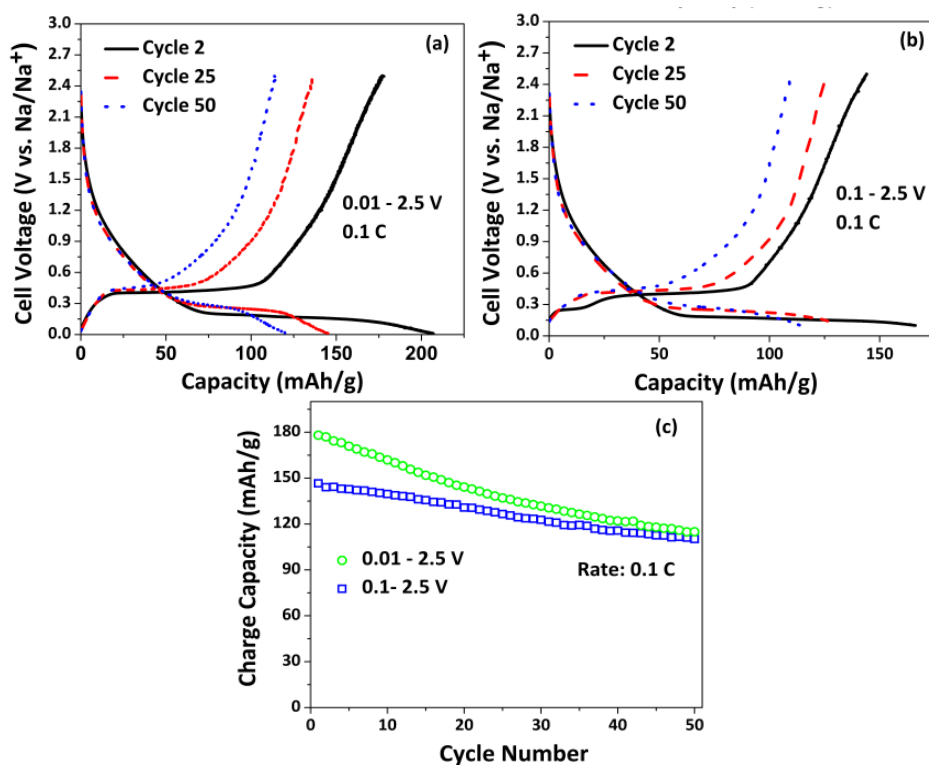
images taken on the pure  $\text{Na}_2\text{Ti}_3\text{O}_7$  sample which was ball-milled at 400 *rpm* for 20 *min* (refer to Fig. 3.13). It can be seen that some of the as-synthesized particle size reduces from 1-2  $\mu\text{m}$  (presented in Fig. 3.5) to less than 100 *nm* upon ball-milling, reducing the particle size by two orders of magnitude. This would promote efficient  $\text{Na}^+$  ion diffusion into the bulk, due to a reduced diffusion length.<sup>73</sup>



**Figure 3.13** | Effect of ball-milling on reducing the active material particle size. FESEM image taken of (a) pure  $\text{Na}_2\text{Ti}_3\text{O}_7$  ball-milled at 400 *rpm* for 20 *min* at a  $\times 200,000$  magnification and (b) ball-milled  $\text{Na}_2\text{Ti}_3\text{O}_7$  with CB at 400 *rpm* for 20 *min* at a  $\times 150,000$  magnification.

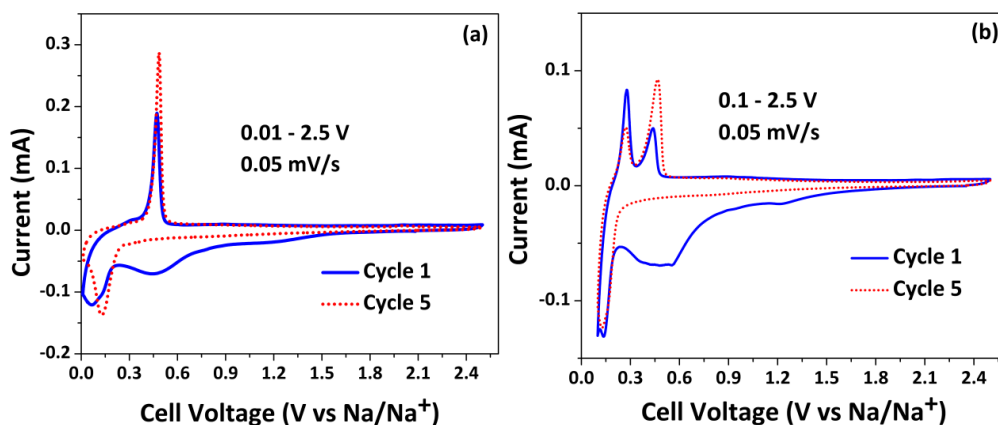
#### 3.4.2.4 Effect of Voltage Window on Cycling Performance

Figure 3.14a and Fig. 3.14b show the first 50 cycles of the ball-milled samples at 0.1 *C* over the voltage window 0.01 – 2.5 *V* and 0.1 – 2.5 *V*, respectively. If the lower cut-off voltage is increased from 0.01 to 0.1 *V*, three noticeable changes take place. Firstly, the capacity delivered decreases, as expected. Secondly, the cycling stability improves significantly, which is illustrated clearly in Fig. 3.14c. In the first 50 cycles, the charge capacity drops by 63 *mAh/g* for the cell cycled between 0.01 - 2.5 *V*, but only drops by 36 *mAh/g* when the  $\text{Na}_2\text{Ti}_3\text{O}_7/\text{CB}$  composite electrode is cycled between 0.1-2.5 *V*.



**Figure 3.14** | Effect of voltage window on cycling profile and performance. (a)  $\text{Na}_2\text{Ti}_3\text{O}_7/\text{CB}$  ball-milled sample cycled between 0.01 – 2.5 V. (b)  $\text{Na}_2\text{Ti}_3\text{O}_7/\text{CB}$  ball-milled sample cycled between 0.1 – 2.5 V. (c) Charge capacity vs cycle number for (a) and (b).

Lastly, and most intriguingly, a new charge plateau was observed at 0.25 V when the electrodes were cycled between 0.1 – 2.5 V. This strange plateau behaviour is clearly highlighted in the CV curves (presented in Fig. 3.15b). The first reductions shown in Fig. 3.15a and Fig. 3.15b have the same broad peak around the 0.45 – 0.5 V range in both voltage windows due to the CB additive. Upon cycling, this reduction peak vanished in the CV curves while only the reduction peak located at 0.13 V was exhibited, in both cases. The fact that reduction takes place at almost the same voltage, suggests that the  $\text{Na}^+$  ion intercalation is the same. However, two oxidation peaks (0.28 V and 0.44 V) were found when the electrodes were cycled between 0.1 - 2.5 V. The intensity of the new peak observed at 0.28 V diminished upon cycling while the 0.44 V peak became more prominent. The reason for the appearance of the new peak has been given in detail in chapter 5.



**Figure 3.15** | Cyclic voltammetry curves illustrating the effect of voltage window. CV at a scan rate of  $0.05 \text{ mV/s}$  showing the first and the fifth cycles of  $\text{Na}_2\text{Ti}_3\text{O}_7/\text{CB}$  ball-milled composite electrode at a voltage window of (a)  $0.01 - 2.5 \text{ V}$  and (b)  $0.1 - 2.5 \text{ V}$ .

### 3.4.2.5 Study of Sodium Insertion and Extraction Kinetics

Since the lower capacity observed at high rates suggests a diffusion limited response, further investigations were performed using CV. The CV plot of the  $\text{Na}_2\text{Ti}_3\text{O}_7/\text{CB}$  sample is shown in Fig. 3.16a over the voltage window  $0.01 - 2.5 \text{ V}$  at different scan rates. It can be seen that the oxidation and reduction peaks do not alter at different scan rates. This confirms the good reversibility of the  $\text{Na}_2\text{Ti}_3\text{O}_7/\text{CB}$  composite electrode. However, it is interesting to note that the oxidation peak intensity is almost double that of the reduction current peak. This seems to imply that the  $\text{Na}^+$  ion extraction process upon charging is more facile than the  $\text{Na}^+$  ion insertion process during discharging. The oxidation and reduction peak currents were plotted with the square root of the scan rate (Fig. 3.16b). The linear relation obtained for both oxidation and reduction shows that the intercalation and de-intercalation process is controlled by diffusion.<sup>74</sup>

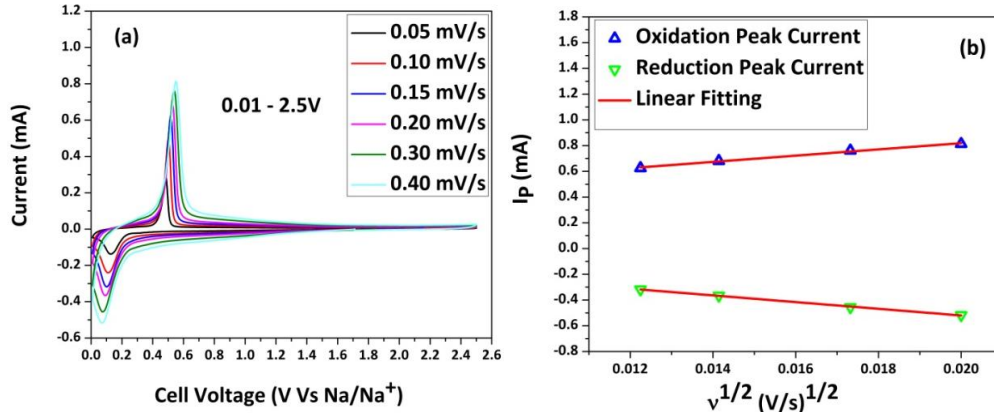


**Figure 3.16** | Evaluation of the sodium storage kinetics using cyclic voltammetry. (a) CV plot for Na<sub>2</sub>Ti<sub>3</sub>O<sub>7</sub>/CB composite electrode for the fifth cycles at various scan rates in the voltage window of 0.01-2.5 V. (b) Plot of the peak current versus square root of scan rate.

To gain a better understanding of the kinetics during the insertion of Na<sup>+</sup> ions in Na<sub>2</sub>Ti<sub>3</sub>O<sub>7</sub>, the sodium chemical diffusion coefficient was calculated using GITT. The procedure used for GITT has been described elsewhere.<sup>75</sup> The sodium chemical diffusion coefficient has been estimated from the GITT curves (refer to Fig. 3.17a) using equation (3.1):

$$D_{GITT} = \frac{4}{\pi\tau} \left( \frac{m_B V_m}{M_B S} \right)^2 \left( \frac{\Delta E_s}{\Delta E_\tau} \right)^2 \quad \left( \tau \ll \frac{l^2}{D_{GITT}} \right) \quad (3.1)$$

In this equation,  $\tau$  is the time period of the current pulse during charge or discharge for a constant current value,  $m_B$  is the mass of the electroactive material,  $M_B$  is its molecular weight and  $V_m$  is its molar volume,  $S$  is the total area of contact of the electrolyte with the electrode,  $\Delta E_s$  is the difference in the open circuit voltage measured at the end of the relaxation period for two successive steps,  $\Delta E_\tau$  is the difference in the cell voltage at the beginning and the end of the current pulse and  $l$  is the thickness of the electrode. The molar volume used in this equation was obtained from the XRD data.<sup>76</sup> This equation can be applied only if there is a linear correlation of  $E_\tau$  with  $\tau^{1/2}$ , which was obtained (refer to Fig. 3.17b). This technique gives accurate results only for small stoichiometric changes and is strictly meant only for a vario-

stoichiometric phase, meaning a solid-solution mechanism.<sup>75, 77</sup> As a consequence, we have applied this technique for a current pulse in the initial stages of discharge of the second cycle, where the composition of the electrode is still close to  $\text{Na}_2\text{Ti}_3\text{O}_7$ . The value of the sodium chemical diffusion coefficient during the insertion of  $\text{Na}^+$  ions into  $\text{Na}_2\text{Ti}_3\text{O}_7$  is calculated to be approximately  $3.48 \times 10^{-12} \text{ cm}^2/\text{s}$ . This is considerably higher than the sodium ion diffusion coefficient for the cathode  $\text{Na}_4\text{Mn}_9\text{O}_{18}$  (around  $10^{-15} - 10^{-16} \text{ cm}^2/\text{s}$ )<sup>78</sup>, indicating the potential for fast-rate application if appropriate  $\text{Na}_2\text{Ti}_3\text{O}_7$  morphology can be obtained.

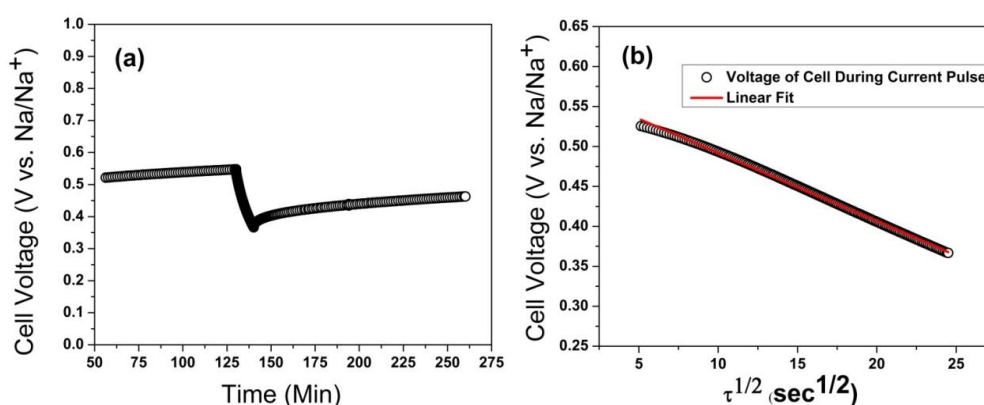


**Figure 3.17** | Evaluation of the sodium chemical diffusion coefficient during the insertion of  $\text{Na}^+$  ions into  $\text{Na}_2\text{Ti}_3\text{O}_7$  using GITT. A representative pulse used for GITT calculations showing (a) one pulse during the initial stages of discharge along with the subsequent relaxation step, and the previous step's relaxation step, and (b) the linear relationship between  $E_t$  with  $\tau^{1/2}$  which is needed for utilizing the GITT relation.

### 3.4.3 Solvothermal $\text{Na}_2\text{Ti}_3\text{O}_7$ Powder Characterization

Since the GITT studies indicated a fairly high sodium chemical diffusion coefficient for  $\text{Na}_2\text{Ti}_3\text{O}_7$ , efforts were made towards decreasing particle size from lengths  $> 1\text{-}2 \mu\text{m}$  obtained from the solid-state synthesis previously described to sub-micrometre dimensions. Furthermore, it was thought that as  $\text{Na}_2\text{Ti}_3\text{O}_7$  is a poor electronic conductor,<sup>59</sup> it will be important that it be made sufficiently electronically conducting so as to enhance its high rate performance. To achieve both these goals simultaneously,  $\text{Na}_2\text{Ti}_3\text{O}_7$  was synthesized by using a solvothermal approach with ethanol as the reaction medium and gluconic acid lactone acting as a carbon source so



as to form some kind of *in-situ* carbon coating or matrix. As depicted in Fig. 3.18a, Rietveld refinement of the structural model with the XRD pattern collected on the as-synthesized material suggests that a pure phase of  $\text{Na}_2\text{Ti}_3\text{O}_7$  was obtained crystallizing in the  $P121/m_1$  space group with good refinement reliability factors and lattice parameters consistent with the literature ( $a = 9.121(4) \text{ \AA}$ ,  $b = 3.800(4) \text{ \AA}$ ,  $c = 8.558(6) \text{ \AA}$  and  $\beta = 101.593^\circ$ ).<sup>44</sup> TGA reveals that the as-synthesized material bears about 14.5 wt% of *in-situ* carbon (see Fig. 3.18b). Please note that this combination of  $\text{Na}_2\text{Ti}_3\text{O}_7$  with *in-situ* carbon is termed as “ $\text{Na}_2\text{Ti}_3\text{O}_7/\text{C}$ ” henceforth in this text.

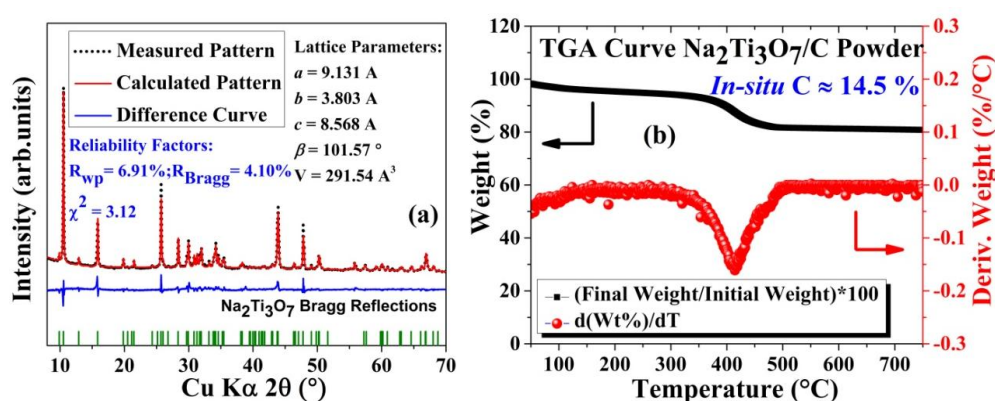


**Figure 3.18** |  $\text{Na}_2\text{Ti}_3\text{O}_7/\text{C}$  powder characterization through XRD and TGA. (a) Rietveld refinement of the as obtained material showing the good fit between the measured pattern and the calculated pattern and the calculated lattice parameters. Please note that “A” in the lattice parameter units refers to Angstroms,  $\text{\AA}$ . (b) TGA curve reveals the amount of *in-situ* carbon arising from the use of gluconic acid lactone in the synthesis.

To gauge the effect of this synthesis on the as-synthesized powder’s morphology, FESEM was utilized. The FESEM image exhibits submicron particles of the as-synthesized  $\text{Na}_2\text{Ti}_3\text{O}_7/\text{C}$  (refer to Fig. 3.19a). It should be stated that it is undesirable to downsize the particle dimensions too much as nano-sizing leads to a loss in the voltage plateaus, thereby eliminating the major advantage of this material and resulting in lower energy density, as demonstrated for  $\text{Na}_2\text{Ti}_3\text{O}_7$  by a previous study.<sup>60</sup> To gauge the nature of the carbon present, SAED and HRTEM was performed and they revealed single crystalline  $\text{Na}_2\text{Ti}_3\text{O}_7$  platelets with the carbon existing as an amorphous matrix (revealed by diffuse SAED rings) surrounding the  $\text{Na}_2\text{Ti}_3\text{O}_7$  particles (shown in Fig. 3.19b). Hence, it can be expected that the as-synthesized

powder should be able to overcome sodium-ion diffusion limitations and potentially ensure full utilization of the active material mass at high rates when cycled in a sodium battery.

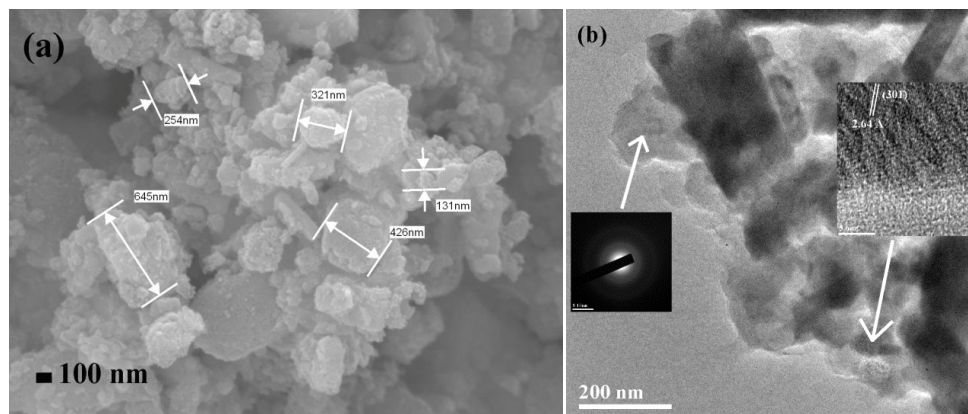


**Figure 3.19** |  $\text{Na}_2\text{Ti}_3\text{O}_7/\text{C}$  powder's morphology characterization. (a) FESEM image highlighting the sub-micrometre particle dimensions. (b) TEM image with the SAED pattern of the surrounding carbon matrix indicating its amorphous nature due to the absence of any diffraction spots. The HRTEM on a single crystalline  $\text{Na}_2\text{Ti}_3\text{O}_7$  platelet shows clear lattice fringes corresponding to the (301) plane with a spacing of 2.64 Å.

These sub-micron sized  $\text{Na}_2\text{Ti}_3\text{O}_7$  particles embedded in a carbon matrix result in a very high surface area of around  $196 \text{ m}^2/\text{g}$ , as indicated by the BET adsorption isotherm depicted in Fig. 3.20a. Furthermore, the BJH pore size distribution shown in Fig. 3.20b of the as-synthesized material demonstrates pores of around 3.8 nm. The existence of these pores along with a high surface area would enable adequate electrolyte wetting, which would help lead to excellent high rate performance (demonstrated in the following section).

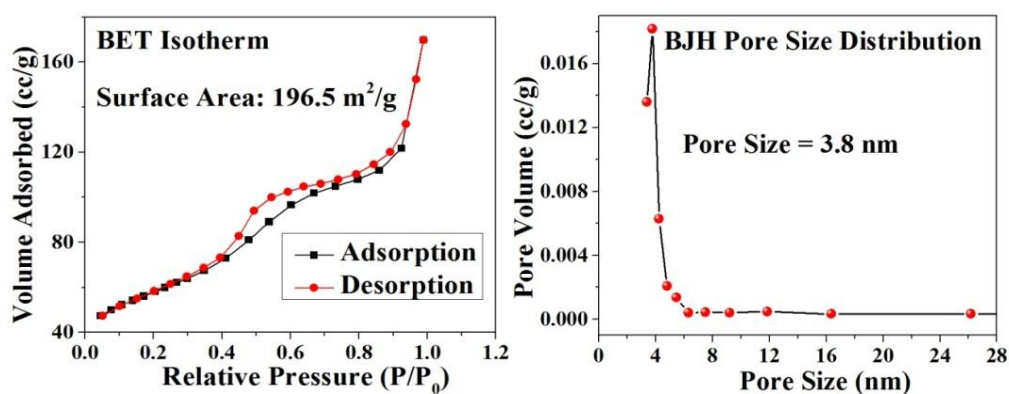


**Figure 3.20** |  $\text{Na}_2\text{Ti}_3\text{O}_7/\text{C}$  powder's surface area and pore size characterization. (a) BET isotherm with the measured surface area and (b) BJH pore size distribution showing the pore size distribution.

### 3.4.4 Solvothermal Na<sub>2</sub>Ti<sub>3</sub>O<sub>7</sub>/C Cycling Performance

The sodium storage performance of the as-synthesized Na<sub>2</sub>Ti<sub>3</sub>O<sub>7</sub>/C composite electrode prepared by the solvothermal process is depicted in Fig. 3.21. From Fig. 3.21a, one can notice that the material can now be cycled up to a very fast 40 C rate (1.5 min charge/discharge). Furthermore, the high rate performance was greatly improved: charge capacities of 97, 70, 43 and 18 mAh/g were witnessed at 5, 10, 20 and 40 C, respectively. This is in stark contrast to the relatively poor high rate cycling of Na<sub>2</sub>Ti<sub>3</sub>O<sub>7</sub> material prepared from solid-state synthesis shown in Fig. 3.11d (only 71 mAh/g was obtained at 5 C). These cycling results are the most promising displayed for this material in the literature and are a direct result of the optimized sub-micrometric Na<sub>2</sub>Ti<sub>3</sub>O<sub>7</sub> particles embedded in an electronically conducting carbon matrix arising from the unique solvothermal synthesis employed in this work.

While this synthesis led to improved high rate performance, it could not adequately improve the cycling stability as the Na<sub>2</sub>Ti<sub>3</sub>O<sub>7</sub>/C composite electrode was found to be stable only at high rates from 10 C onwards. At low rates ( $\leq 2$  C), the material still displayed poor capacity retention, similar to that seen for the solid-state synthesized Na<sub>2</sub>Ti<sub>3</sub>O<sub>7</sub> (refer to Fig. 3.11d). This fact is fully appreciated by comparing Fig. 3.21b with Fig. 3.11a: the Na<sub>2</sub>Ti<sub>3</sub>O<sub>7</sub>/C composite electrode was able to retain 57.7 % of its initial capacity over 100 cycles at a 0.2 C rate, while the Na<sub>2</sub>Ti<sub>3</sub>O<sub>7</sub>/CB composite electrode prepared from solid-state synthesis demonstrated capacity retention of 56 %. Even though the high rate performance of Na<sub>2</sub>Ti<sub>3</sub>O<sub>7</sub> was improved by particle downsizing and increased electronic conductivity achieved through a solvothermal synthesis, the cycling stability still was not satisfactory. In fact, it was very recently shown that the fully discharged material (*i.e.* Na<sub>4</sub>Ti<sub>3</sub>O<sub>7</sub>) undergoes self-relaxation.<sup>44</sup> This structural instability seems to be an inherent trait of the Na<sub>4</sub>Ti<sub>3</sub>O<sub>7</sub> phase and may likely be the reason for its poor cycling stability observed in this work, as well as in other published studies.<sup>44, 57-62</sup>

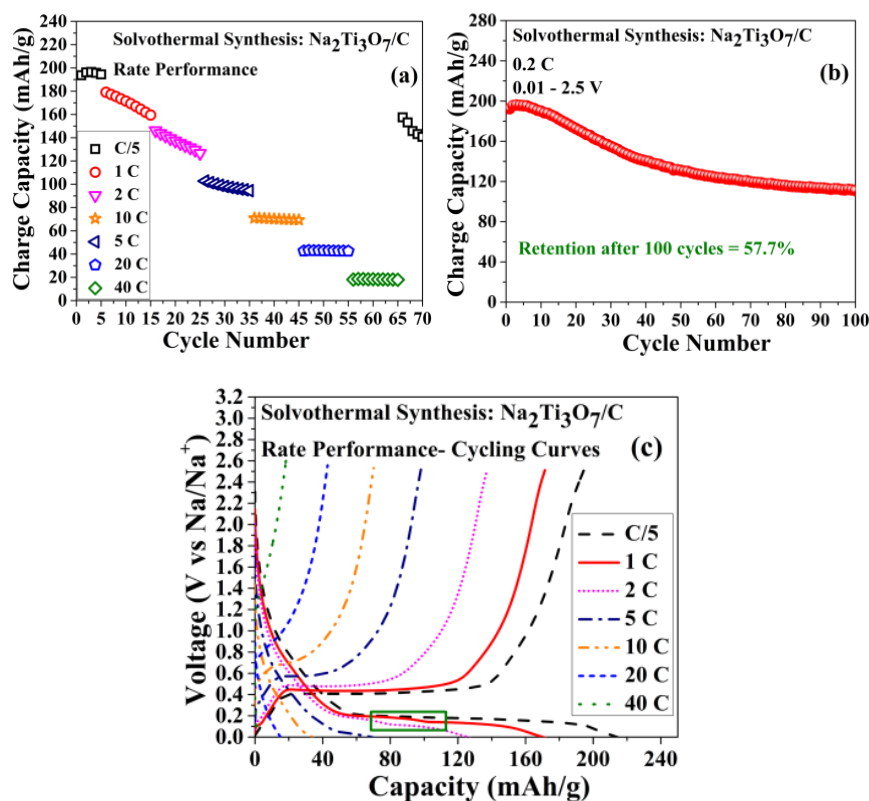


**Figure 3.21** | Cycling performance of  $\text{Na}_2\text{Ti}_3\text{O}_7/\text{C}$  prepared by the solvothermal synthesis. (a) Charge capacity obtained vs cycle number at various rates. (b) 100 cycles at 0.2 C rate. (c) Corresponding galvanostatic cycling curves for (a). For the rate performance test,  $\text{Na}_2\text{Ti}_3\text{O}_7/\text{C}$  was cycled in a three-electrode cell, with the cycling limits controlled by the working electrode's voltage. The cycling profiles shown in (c) are for the resulting two-electrode's cycling profile (the profile of sodium metal counter electrode subtracted from that of the working electrode). The reason for this will be clear in chapter 4.

The galvanostatic cycling curves of the rate performance test (refer to Fig. 3.21c) elicit two important points. Firstly, they demonstrate progressively increasing polarization with complete loss of the charge plateaus at 20 and 40 C. In particular, it is noteworthy that the polarization displayed by this material is still greater than 0.20 V even at very slow cycling rates of C/5 despite incorporating  $\text{Na}_2\text{Ti}_3\text{O}_7$  within a conductive carbon matrix. A recent report<sup>59</sup> has discussed that a polarization  $\geq 0.225$  V can be expected for this material as it could be dictated by thermodynamic factors, likely owing to structural considerations.<sup>58</sup> Hence, it could be possible that further morphology optimization may not have much effect on its cycling stability and polarization, a fact which would be quite detrimental towards its utilization as an anode for NIB application.

Secondly, the discharge curves of this material at high rates (for example, 1 and 2 C) exhibit a peculiar voltage step, highlighted by the green box in Fig. 3.21c. Such a voltage step is not witnessed at low C rates during discharge (such as, at C/5) or in the corresponding charging curves. In fact, this observation is similar to that observed by us on another material, the cathode  $\text{Na}_3\text{V}_2(\text{PO}_4)_3$ .<sup>15</sup> The cause for this unusual voltage step has been uncovered and will be discussed in chapter 4. Chapter 4 will also provide the reasoning behind cycling the  $\text{Na}_2\text{Ti}_3\text{O}_7/\text{C}$  in a three-electrode cell.

### 3.5 Summary

We have attempted to gain a deeper understanding into the sodium storage performance of  $\text{Na}_2\text{Ti}_3\text{O}_7$ . Firstly, we have synthesized  $\text{Na}_2\text{Ti}_3\text{O}_7$  by a solid-state route using anatase  $\text{TiO}_2$  and  $\text{NaOH}$ . The as-prepared micrometer sized powder is predominantly  $\text{Na}_2\text{Ti}_3\text{O}_7$ . Ball-milling was carried out along with the carbon additive to enhance the electronic conductivity and to downsize the  $\text{Na}_2\text{Ti}_3\text{O}_7$  particles. This  $\text{Na}_2\text{Ti}_3\text{O}_7/\text{CB}$  composite electrode delivered theoretical capacities at slow cycling rates with a small amount of fade per cycle. In contrast, the cycling retention improved significantly at high rates, though the capacities delivered were considerably less than the theoretical value. It was found that ball-milling  $\text{Na}_2\text{Ti}_3\text{O}_7$  with CB demonstrated better storage performance in terms of both delivered capacity and retention, when compared with hand-grinding  $\text{Na}_2\text{Ti}_3\text{O}_7$  with CB for the preparation of electrodes. The ICL in the first cycle is due to electrolyte decomposition to form an SEI. In this regard, switching the conductive additive from CB to graphite did not decrease the ICL, implying that graphite is an effective conductive additive only if the galvanostatic cycling of an anode is stopped around 0.5 V vs  $\text{Na}/\text{Na}^+$  (as was done in the previous chapter) but is ineffective if discharged down to 0.01 V vs  $\text{Na}/\text{Na}^+$ . Interestingly, we found that increasing the lower cut-off voltage from 0.01 to 0.1 V introduced a new charge plateau during cycling. The cause

for this new plateau will be discussed in chapter 5. CV studies indicated that sodium intercalation and de-intercalation was limited by diffusion. Hence, the chemical diffusion coefficient for the insertion of sodium ions into this material was obtained using GITT technique and estimated to be  $3.48 \times 10^{-12} \text{ cm}^2/\text{s}$ .

The relatively high value of the diffusion coefficient prompted us to, secondly, devise a new synthesis strategy so as to decrease the particle size to sub-micrometric dimensions as it was believed that large particle size was the reason for poor high rate sodium storage performance of  $\text{Na}_2\text{Ti}_3\text{O}_7$  synthesized from the solid-state method. Particle size reduction was achieved through a novel solvothermal synthesis approach, which also resulted in  $\text{Na}_2\text{Ti}_3\text{O}_7$  particles being embedded in a carbon matrix. The resulting  $\text{Na}_2\text{Ti}_3\text{O}_7/\text{C}$  was shown to display excellent high rate performance, storing sodium even at a very fast 40 C rate. However, the cycling was not found to be adequately stable. Furthermore, the material demonstrated a large polarization  $\geq 0.20 \text{ V}$  even at low rates of cycling. Such a large polarization would undoubtedly result in low RTEE of a NIB, adversely affecting its sodium storage performance. These two drawbacks, *viz.* poor cycling stability and high polarization, are believed to be inherent to the  $\text{Na}_2\text{Ti}_3\text{O}_7 \rightleftharpoons \text{Na}_4\text{Ti}_3\text{O}_7$  sodium storage pathway. Hence, it may be unlikely that improvements in its cycling could be made through morphology optimization, unless the crystal structure of  $\text{Na}_2\text{Ti}_3\text{O}_7$  is appropriately modified such as through stabilizing dopants. With these results, we believe that while  $\text{Na}_2\text{Ti}_3\text{O}_7$  holds great promise as a non-carbon based, low-voltage anode material for room temperature NIB applications owing to its high capacity (178  $\text{mAh/g}$ ), low average voltage (0.3 V vs  $\text{Na}/\text{Na}^+$ ) and good sodium chemical diffusion coefficient, it is yet to display all qualities required for a NIB anode to be employed for grid storage. The quest for such a suitable NIB anode material is, hence, still not complete.

## **Chapter 4 | Understanding the Role of the Sodium CE in Half Cell Evaluation in Sodium Batteries**

---

**The results described in this chapter have been published/presented in the following journals/conferences:**

1. **A. Rudola, D. Aurbach and P. Balaya, *Electrochem. Commun.*, 2014, 46, 56-59**
2. 55<sup>th</sup> Battery Symposium in Japan, Kyoto, Japan, November 2014 → **Oral Presentation**
3. 39<sup>th</sup> International Conference and Expo on Advanced Ceramics and Composites (**ICACC 2015**), Daytona Beach, Florida, USA, January 2015 → **Poster Presentation**

## 4.1 Preface to Chapter 4

The galvanostatic cycling of electrode materials in lithium or sodium batteries is assumed to arise just from the contribution of the working electrode, with the counter electrode seen as always operating at a fixed potential. In this chapter, a hitherto unreported phenomenon in sodium batteries is revealed which involves a voltage step seen in the discharge profiles at high rates of two-phase electrode materials that is produced not from a change in voltage of the working electrode, but from an increase in polarization of the counter electrode. The choice of solvent used is critical in this context, with the phenomenon existing for EC:PC solvent and not for PC. It arises due to a passivation layer(s) formed on the sodium counter electrode. The voltage step is observed only in the presence of sodium metal as the counter electrode, as it is not seen in full sodium-ion cells. This passivation layer(s) also causes a sodium counter electrode to operate at high overvoltage at high  $C$  rates (or current densities), as much as  $0.2\text{ V vs Na/Na}^+$  or ever higher. The results contained in this chapter are believed to have profound implications for all researchers working in the field of NIBs, especially those evaluating the sodium storage performance of low voltage anodes.



## 4.2 Introduction

In the previous chapter, a peculiar voltage step was observed in the galvanostatic profiles during the discharge (sodium insertion) of  $\text{Na}_2\text{Ti}_3\text{O}_7$  at high rates, but such a step was not observed during the corresponding charge (sodium extraction) profiles and also not during slow rates of discharge/charge. In fact, in a recent publication, we also noticed such a voltage step in the galvanostatic profile of  $\text{Na}_3\text{V}_2(\text{PO}_4)_3$  (NVP) during discharge when cycled in a sodium half cell.<sup>15</sup> Similar to the case of  $\text{Na}_2\text{Ti}_3\text{O}_7$ , this voltage step was noticed only at high rates of discharge, and was not observed during the charge cycle. Even more intriguingly, other reports published on NVP did not exhibit this voltage step.<sup>79-82</sup> Thinking that this voltage step observation in  $\text{Na}_2\text{Ti}_3\text{O}_7$  and NVP was interrelated, we sought to reproduce this on another material and understand its cause.

In this chapter, we report this observed phenomenon on another material,  $\text{NaTi}_2(\text{PO}_4)_3$  (NTP). This material was chosen due to its flat cycling profile owing to its two-phase sodium storage mechanism, as well as its redox potential ( $\approx 2.1 \text{ V vs Na/Na}^+$ ) lying right in the middle of the electrochemical stability window of the electrolyte solutions based on alkyl carbonate solvents.<sup>30, 32</sup> It will be shown that this voltage step is not caused by any change in the working electrode (WE). Surprisingly, it arises due to an *in-situ* passivation layer formed on the sodium counter electrode (CE) caused by solvent interactions that produce surface species, which form and dissolve during each cycle. The traits of this passivation layer and implications to full sodium-ion cells will be discussed. To the best of our knowledge, this would be the first instance where the galvanostatic cycling profile of a sodium battery is influenced by a passivation layer formed on the CE. Another important effect of the sodium CE towards assessment of a working electrode's sodium storage performance will be

stated which is believed to be quite important for all researchers working in the NIB field, especially those studying low voltage anodes.

## **4.3 Experimental Section**

### **4.3.1 Synthesis**

$\text{NaTi}_2(\text{PO}_4)_3$  was synthesized using the soft-template approach. Sodium acetate, orthophosphoric acid, titanium isopropoxide and CTAB were used as the sodium, phosphate, titanium and templating sources, respectively. An ethanol-water mixture constituted the reaction medium to which appropriate molar ratios of the chemicals were added, with 3.64 g of CTAB being utilized. The resulting solution was stirred for 12 h, before being dried by roto-evaporation. Finally, the powder was made to undergo a two-step calcination process (450 °C for 4 h before being ramped up to 800 °C for another 4 h) and allowed to cool naturally. The resultant black powder was the desired product. For the micro-sized NTP, the same synthesis procedure was adopted as described above, except for the fact that CTAB was not used.

### **4.3.2 Synthesized Powder Characterization**

PXRD patterns were recorded using a D2 Phaser Bruker X-ray diffractometer equipped with Cu K $\alpha$  radiation. The accelerating voltage and current were 40 kV and 40 mA, respectively. A step size of 0.02° was used with 0.2 s per step. TGA was conducted by a TA instrument 2960 in air where the sample was heated from room temperature to 900 °C with a 10 °C/min ramp rate.

### **4.3.3 Electrochemical Characterization**

Coin-cells were fabricated with NTP as the working electrode and sodium metal as the CE and the reference electrode (RE). The NTP electrode consisted of NTP: PVDF binder in the weight ratio of 90:10 (no external Super P carbon black was used). For the three-electrode cells, NTP electrode served as the WE, sodium metal disk served

as the CE and a sodium metal ring served as the RE. Commercial three-electrode cells provided by MTI (model number EQ-3ESTC15) were used. In all cases, the electrolytes used were 1M NaClO<sub>4</sub> in ethylene carbonate (EC): propylene carbonate (PC) in a 1:1 volume ratio, and 1M NaClO<sub>4</sub> in PC, as specified. Electrochemical Impedance Spectroscopy (EIS) studies were performed on a three-electrode cell using the VMP3 instrument (Bio-Logic, France) between 1 MHz to 10 mHz and the resulting Nyquist plots were fit using the EC-Lab software (ver. 10.19). Other relevant information is the same as that contained in the previous chapters.

## 4.4 Results and Discussion

### 4.4.1 As-synthesized Powder Characterization

Since the desired objective in this work was to firstly reproduce the voltage step in NTP as well, an optimized morphology was required. This was achieved through a soft-template synthesis which has been shown previously to obtain favourable morphology for Na<sub>2</sub>Ti<sub>6</sub>O<sub>13</sub> in chapter 2, as well as for other titanates such as TiO<sub>2</sub>.<sup>66</sup> The PXRD pattern of the as-synthesized NTP powder, shown in Fig. 4.1a, suggests that a pure phase with no impurity peaks was obtained, when compared with the standard pattern (number 20776) of the Inorganic Crystal Structure Database (ICSD). A uniform morphology in the nanometer dimensions resulted from this synthesis procedure, with an average particle size being around 100 nm (refer to Fig. 4.1b). Such small particle size is desirable and expected to result in excellent high rate performance. The other component towards good sodium storage performance at high rates, *viz.* adequate electronic conductivity, was also achieved through this synthesis due to the presence of *in-situ* carbon. TGA analysis, presented in Fig. 4.1c, indicates that the as-prepared material consisted of around 12 weight % *in-situ* carbon. Hence, the soft-template synthesis gave rise to quite optimal morphology of

NTP and electrochemical measurements were thus performed with the hope of witnessing the voltage step.

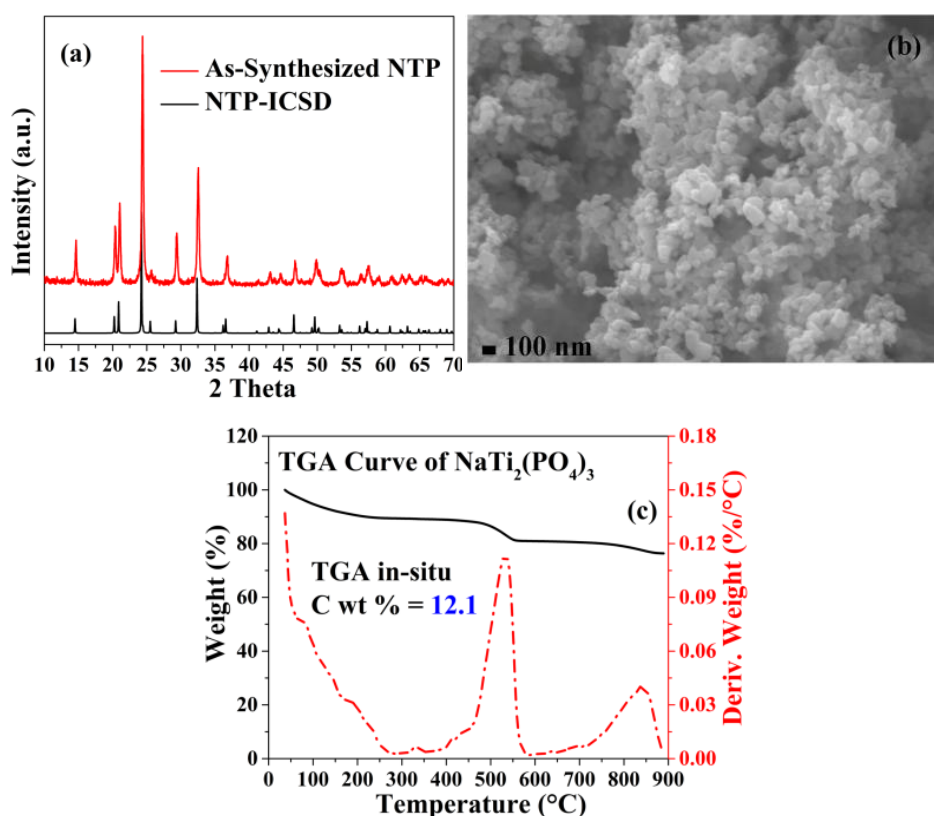


**Figure 4.1** | Material characterization of the as-prepared NTP. (a) PXRD pattern demonstrating the good match obtained with the standard pattern of NTP. (b) FESEM image of NTP showing uniform particle size around 100 nm. (c) TGA curve of NTP in air depicting the amount of *in-situ* carbon as a result of the soft-template synthesis to be around 12 wt%.

#### 4.4.2 Reproduction of the Voltage Step Phenomenon

Figure 4.2a depicts the cycling of NTP in a two-electrode coin cell versus sodium metal acting as the CE and RE simultaneously. The voltage step on discharge in EC:PC solution at 5 C rate is clearly seen. At a low C/5 rate, this step is barely noticeable. The step is also observed at other high rates (e.g., 1, 2 and 10 C) in EC:PC solution (see Fig. 4.2b). This result is analogous to that seen in the discharge profile of NVP at high rates.<sup>15</sup> It should be mentioned that the voltage step is witnessed in EC:PC solution irrespective of the NTP morphology, as illustrated by Fig. 4.2d and Fig. 4.2e, which indicates that the step can be elicited even by electrodes consisting of micro-sized NTP particles.

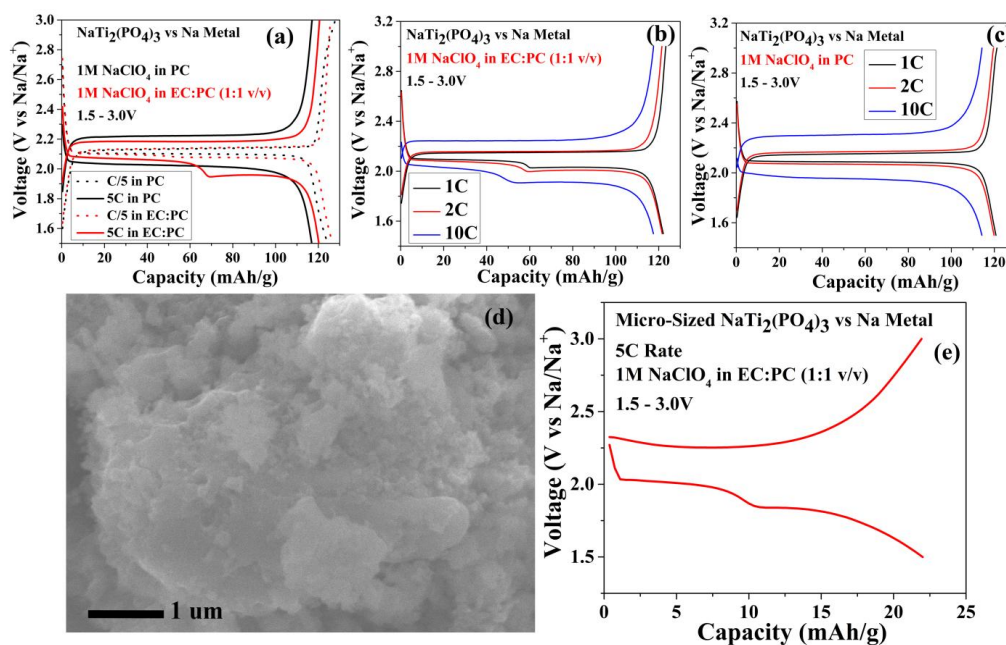


**Figure 4.2** | Reproduction of the voltage step phenomenon in NTP. (a) Illustration of the voltage step phenomenon. The voltage step is witnessed in EC:PC based solutions at high rates of discharge but not in PC solutions. The voltage step is observed at different rates in EC:PC solution (b) but not in PC solution at the same rates (c). (d) FESEM image of micro-sized NTP prepared by the soft-template synthesis and (e) its corresponding galvanostatic cycling in EC:PC solution, demonstrating that the voltage step will be witnessed irrespective of the morphology of the WE.

Surprisingly, when cycled in  $1M$   $\text{NaClO}_4$  in PC, the NTP electrode did not display a voltage step for any  $C$  rate (refer to Fig. 4.2a and Fig. 4.2c). Such an observation mirrors the lack of voltage step seen in NVP by other groups, as all other reports published on NVP in the literature use PC as the solvent.<sup>79-82</sup> Since the same material is used as the WE, the voltage step should not arise from the way Na intercalates into the crystal structure of NTP irrespective of the solvents used. This fact is very surprising since the flat plateau nature of the cycling profile, before and after the voltage step, seems to indicate that there could be different two-phase domains or two different energetic sites for inserted Na-ions.

### 4.4.3 Three-electrode Cycling Studies

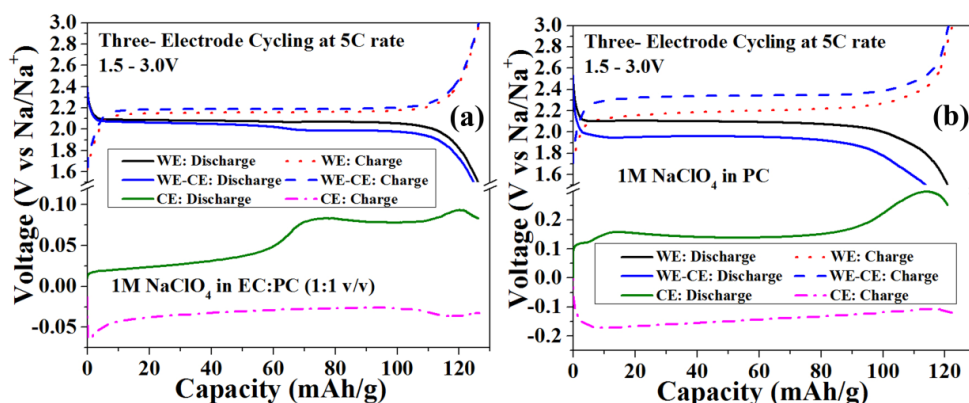


**Figure 4.3** | Three-electrode cycling of NTP to understand the cause of the voltage step phenomenon. Three-electrode cycling for NTP WE against Na CE and RE, in 1M NaClO<sub>4</sub> in EC:PC (a) and PC (b). Abrupt increase of the Na CE's polarization midway through discharge in EC:PC solution is clearly seen and results in the voltage step in WE-CE profile seen in the traditional half cell approach.

From previous work<sup>83, 84</sup>, it is well known that WE materials operating within the electrolyte solution's stability zone (away from low voltages which lead to SEI formation) may be covered by a passivation layer when they come in contact with the electrolyte solution due to surface interactions of transition metal oxides with electrophilic solvents such as alkyl carbonates. Therefore, it was thought that there could be a passivation layer formed on NTP electrodes which is different in EC:PC solutions compared to PC, similar to the differences seen on the SEI formed on hard carbon anodes in these solvents.<sup>30</sup> To glean more insight into this unusual voltage step, a three-electrode cell was constructed using EC:PC and PC based solutions. The corresponding cycling curves are presented in Fig. 4.3a and Fig. 4.3b, respectively. Surprisingly, the behavior of the WE was found to be identical in both solutions. What was striking was the role of the sodium metal CE upon discharge; in EC:PC solutions, a clear voltage polarization-step is seen around 65 mAh/g which is absent in pure PC solutions. Hence, it is not a surprise to note that the traditional two-electrodes cycling curve, which is just a result of the cycling profile of the CE subtracted from that of the WE, exhibits the voltage step.

#### 4.4.4 Impedance Studies

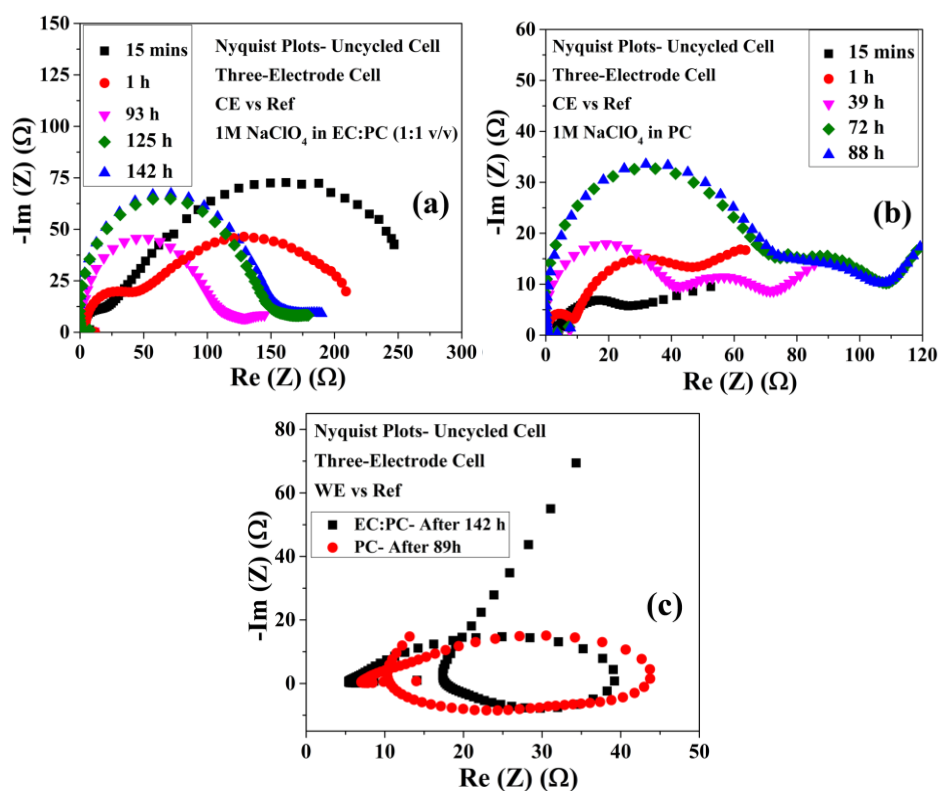


**Figure 4.4** | EIS studies on uncycled cells. Nyquist plots for the Na CE as a function of time for uncycled cells in (a) EC:PC and (b) PC solution. (c) Nyquist plots for the NTP WE in both solutions. The scale of the x and y axes have been purposely kept different to help conveniently gauge the shape of the impedance spectra.

The difference in the polarization of the sodium CE clearly suggests a difference in the way these solutions interact with sodium metal. To understand this interaction, EIS was performed on three-electrode cells. Firstly, an experiment was undertaken to examine what happens to the sodium CE when a cell is fabricated without any current passing through it. The Nyquist plots of the impedance response of the Na CE as a function of time in both EC:PC and PC solutions are presented in Fig. 4.4a and Fig. 4.4b, respectively. Generally, the Nyquist plots exhibit a semicircle in the high-medium frequency region, and another semicircle in the middle-low frequencies. The high frequency semicircle is attributed to a surface film which could be any electrode-electrolyte interfacial film, the second semicircle at middle-low frequency range arises due to charge transfer and the diameter of each semicircle is a measure of the resistance of the corresponding processes.<sup>83</sup> These features are observed even for

lithium electrodes immersed in non-aqueous electrolyte solutions.<sup>83, 85</sup> In both solutions, the fresh cell displays a time-varying impedance response, with the general trend being a decrease in the middle-low frequency semicircle and an increase in the high frequency semicircle. This indicates that when Na metal is placed in these solutions, sodium ions are being consumed to form a passivation layer on it. Over time, the passivation layer appears to reach a meta-stable state. Hence, the growth of the passivation layer on the Na CE electrode is time-dependent. Furthermore, the passivation layer formed in the EC:PC solution appears to be more resistive than that formed in PC solution. It is interesting to note that no significant difference was observed in the Nyquist plots of the NTP electrodes in EC:PC vs PC solutions (Fig. 4.4c). The induction loop seen at low frequencies is believed to be a consequence of the two-phase sodium storage mechanism of NTP and is observed by other groups as well.<sup>86, 87</sup>

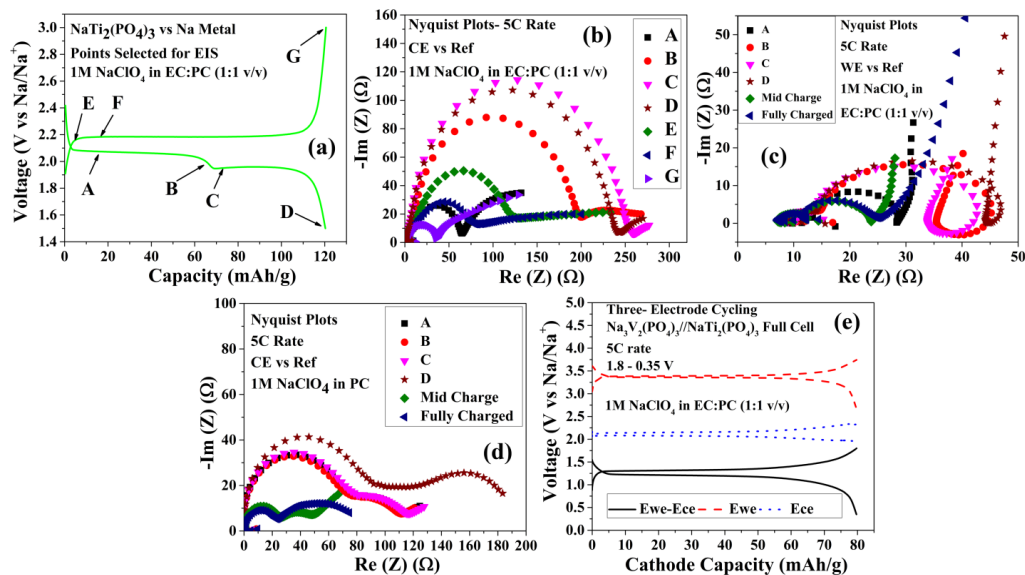


**Figure 4.5** | EIS studies while cycling along with implications of the voltage step on full NIBs. (a) Points chosen for EIS measurements during cycling at 5 C. Corresponding Nyquist plots in EC:PC for (b) Na CE and (c) NTP WE and (d) Na CE in PC. Please note that for (c) and (d) “Mid charge” and “Fully charged” mean data collected at 65 mAh/g and at 3 V during charging, respectively. The scale of the x and y axes have been purposely kept different to help conveniently gauge the shape of the impedance spectra. (e) NVP//NTP full sodium-ion cell cycled at 5 C.

To study how these passivation layers change during the course of cycling, EIS plots were obtained at different states of discharge/charge in EC:PC solutions at 5 C rate,



as depicted in Fig. 4.5a. As seen from Fig. 4.5b, a drastic increase is observed in the resistance of the passivation layer (indicated by the diameter of the high frequency semicircle) formed on the Na CE around the voltage step (points B and C). Upon charge of the cell, the resistance gradually decreases to much smaller values. No significant differences are seen in the corresponding Nyquist plots of the NTP electrode (Fig. 4.5c). These observations imply two points. Firstly, during the course of cycling, an *in-situ* surface film of high resistance is formed on the Na CE during discharge which dissolves in the following charging step. This process is repeated in each cycle. Secondly, the increase in resistance of the passivation layer necessitates over-potential of the Na CE and it is this over-potential that manifests itself as the observed step in the two-electrode galvanostatic profile.

For the case of PC solutions, Nyquist plots were obtained at the same capacity values during discharge with respect to Fig. 4.5a, and are depicted in Fig. 4.5d. The resistance of the Na CE's passivation layer was essentially found to remain unchanged during the course of discharge. Hence, no voltage step is seen if the solvent is PC. Similar to the EC:PC case, this passivation layer formed on Na CE dissolves during the charging step and reforms in the next discharge step. Comparing the behavior in the two solutions, it can be concluded that the high resistivity of the passivation layer in the EC:PC solution must come from the presence of EC (in line with the higher reactivity of EC for reduction processes compared to PC).

#### **4.4.5 Voltage Step Phenomenon in Full Cells**

Since EC:PC has a pronounced effect on Na CE leading to the voltage step, the question arises as to how this phenomenon would affect a full sodium-ion cell which does not contain sodium metal. To understand this point, a full sodium-ion cell was fabricated with NVP as the cathode and NTP as the anode. The cycling of this full cell is depicted in Fig. 4.5e at a high 5 C rate. Smooth and flat profiles for both the NVP and NTP electrodes result in no voltage step being observed in the full cell's

cycling profile. Hence, for the voltage step to be observed, not only EC:PC mixture is essential, but also sodium metal acting as the counter electrode.

It should be kept in mind that this passivation layer has nothing to do with the state of the WE surface which is often influenced by SEI. SEI effects are seen at highly reducing voltages being really noticeable only below 0.9 V vs Na/Na<sup>+</sup> in sodium batteries.<sup>88</sup> SEI formation on the NTP electrode does not take place since the lower cut-off potential in this work was 1.5 V. The unique passivation phenomenon described herein relates to the presence of EC in sodium battery systems. The existing knowledge gathered on the formation and traits of SEI in lithium and sodium batteries may not be applicable to this passivation phenomenon. Hence, a new chemical and physical explanation needs to be developed to understand it.

#### **4.4.6 High Polarization of the Sodium CE**

Apart from the voltage step phenomenon, these results also illustrate the high polarization of sodium metal in alkyl carbonate solvent based solutions. Referring to Fig. 4.3, one can notice that the Na CE operates not quite at 0.0 V vs Na/Na<sup>+</sup>, as one may expect. Instead, at a 5 C rate, the polarization of Na metal CE can be as much as 0.1 – 0.2 V vs Na/Na<sup>+</sup>. In fact, as the rate of cycling increases, so does the polarization, as is evident from Fig. 4.6, which compares the polarization of the Na CE at different C rates during discharge with NTP as the WE in a three-electrode cell. It should be kept in mind that this polarization is a result of the current density experienced by the Na CE. Hence, for extremely heavily loaded WE or high capacity anode materials (such as those based on conversion or alloy reactions where the capacity can approach 1,000 mAh/g or even higher), even cycling at C/5 may elicit the increased polarization and also the voltage step, since such effects are prevalent even at low current densities, but are just not as noticeable.

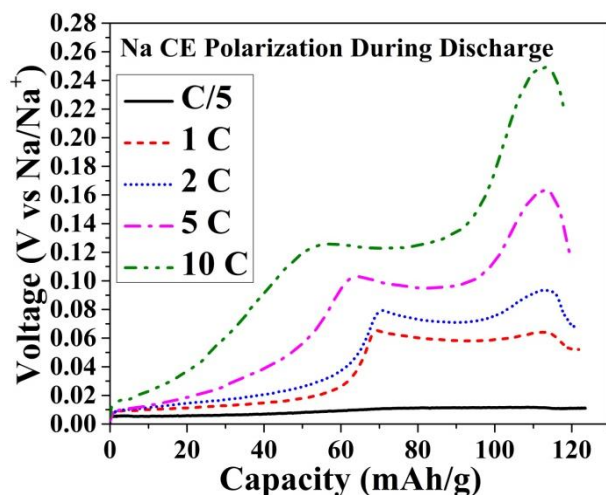


**Figure 4.6** | Illustration of the increase in Na CE's polarization during galvanostatic cycling at different  $C$  rates in alkyl carbonate solvents based solutions. The WE was NTP. Electrolyte was  $1M$   $NaClO_4$  in EC:PC (1:1 v/v).

This fact has important implications for the evaluation of low voltage NIB anodes such as  $Na_2Ti_3O_7$  in a sodium half cell. If the Na CE's voltage itself can be as high as  $0.2$  V, then, a low voltage anode whose redox voltage lies below  $0.2$  V vs  $Na/Na^+$  will not be able to reach its voltage plateau in the traditional half cell approach at high  $C$  rates: the two-electrode cell will prematurely reach the stated cut-off voltage predefined by the system/user (such as  $0.01$  V) even though the WE will not be at  $0.01$  V. Figure 4.7 clarifies this point, by depicting the WE as well as WE-CE galvanostatic cycling curves during discharge at  $1/5$ ,  $1$ ,  $5$  and  $20$   $C$  rates of  $Na_2Ti_3O_7/C$  whose cycling performance was exhibited as Fig. 3.21 in the previous chapter. One can notice that at  $C/5$ , the low polarization of the Na CE (as well as the low polarization of the WE) enables the WE-CE profile to complete its discharge plateau, resulting in theoretical capacity to be displayed in the charge cycle. However, at high rates, the increased polarization of the Na CE is compounded on the increased polarization of the WE. For example, at  $5$   $C$  rate, the WE delivered  $99$  mAh/g upon reaching  $0.01$  V vs  $Na/Na^+$ . However, the WE-CE profile (which would have been the only profile seen during two-electrode cycling in a sodium half cell) would have indicated that  $Na_2Ti_3O_7/C$  only delivered  $66$  mAh/g at  $0.01$  V vs  $Na/Na^+$ . Hence, at

high  $C$  rates, one may need to be careful while interpreting sodium storage performance in a half cell. Perceived poor high rate performance could actually arise due to the fact that sodium was never inserted into the anode in the first place owing to the cell prematurely reaching the stated cut-off voltage. These results highlight the importance of utilizing a three-electrode cell for studying the sodium storage properties of electrode materials in sodium batteries.

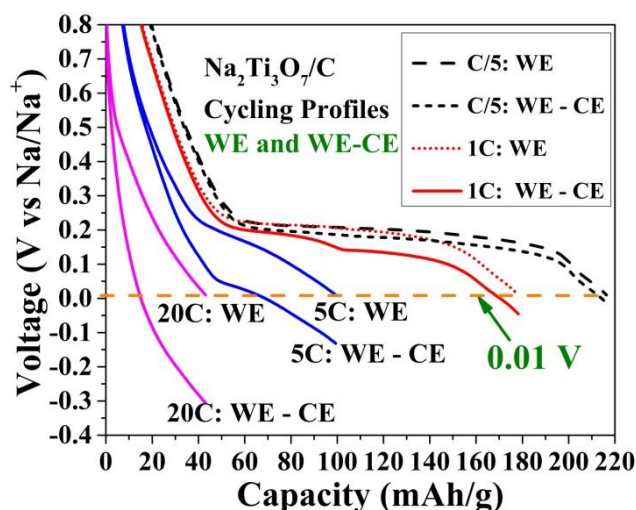


**Figure 4.7** | Illustration of the possibility of erroneous data interpretation in sodium half cells of low voltage NIB anodes caused by increased Na CE's polarization. Due to the increased Na CE polarization, the WE-CE profile of  $\text{Na}_2\text{Ti}_3\text{O}_7/\text{C}$  operates correspondingly at lower voltages with respect to the WE voltage. This causes premature cycling stoppage owing to the WE-CE profile reaching the cut-off voltage prematurely. Please note that for this cell, the cycling was stopped only when the WE reached 0.01 V vs  $\text{Na}/\text{Na}^+$ . Electrolyte was 1M  $\text{NaClO}_4$  in EC:PC (1:1 v/v).

## 4.5 Summary

We have uncovered the reason for the unusual voltage step seen in the galvanostatic cycling profile of flat-potential electrode materials such as  $\text{Na}_2\text{Ti}_3\text{O}_7$ ,  $\text{Na}_3\text{V}_2(\text{PO}_4)_3$  and  $\text{NaTi}_2(\text{PO}_4)_3$  when cycled against sodium metal in EC:PC solutions. The voltage step arises due to an increase in polarization of the sodium counter electrode. With the aid of EIS, it was shown that this polarization must arise due to a passivation layer formed on the sodium counter electrode. While passivation layers are formed in PC solutions as well, its nature is different, since no polarization-step is seen. Hence, these cells do not exhibit the voltage step when cycled with PC solutions. It was

confirmed that the voltage step phenomenon does not relate at all to the working electrode (and any related surface aspects formed on it). It was clearly demonstrated (using full sodium-ion cells) that the voltage step with EC:PC solutions relates only to the sodium metal counter electrodes in the cells. Furthermore, the increased polarization of the Na CE during discharge at high rates may drastically skew cycling performance in traditional half cells and hence, their interpretation. These results demonstrate that the common practice of evaluating the properties of electrode materials for NIBs in half cells needs careful studies since there may be pronounced effects related to the sodium counter electrodes (not seen during half cell testing of Li-ion insertion electrodes). The lessons learnt from this chapter will be shown to be instrumental towards achieving the results stated in the following chapter.



## **Chapter 5 | A 0.2 V Earth-abundant Sodium-ion Battery Anode: the $\text{Na}_2\text{Ti}_3\text{O}_7$ to $\text{Na}_{3-x}\text{Ti}_3\text{O}_7$ Sodium Storage Pathway**

---

**The results described in this chapter have been published/presented in the following journals/conferences:**

1. **A. Rudola, N. Sharma and P. Balaya, *Electrochem. Commun.*, 2015, 61, 10-13**
2. 8<sup>th</sup> International Conference on Materials for Advanced Technologies (**ICMAT 2015**), Singapore, July 2015 → **Oral Presentation**
3. 11<sup>th</sup> International Conference on Ceramic Materials and Components for Energy and Environmental Applications (**CMCEE 2015**), Vancouver, Canada, June 2015 → **Oral Presentation**

## 5.1 Preface to Chapter 5

Renewable sources of energy will become cost-effective if the energy storage system used to handle their intermittency is also low cost. Sodium-ion batteries (NIBs), relying on the globally widespread sodium resources, are appealing grid energy storage devices especially when integrated with earth abundant elements such as iron or titanium. High voltage iron-based cathode materials have been recently discovered which function very well in NIBs. No single NIB anode has been shown to possess all qualities required for a material applicable for grid storage. In this chapter, a new sodium storage pathway is unveiled for the anode  $\text{Na}_2\text{Ti}_3\text{O}_7$  for the first time. The  $\text{Na}_2\text{Ti}_3\text{O}_7 \rightleftharpoons \text{Na}_{3-x}\text{Ti}_3\text{O}_7$  sodium storage pathway has the lowest voltage of 0.2 V vs  $\text{Na}/\text{Na}^+$  ever reported for a non-carbon based NIB anode along with negligible polarization, excellent rate performance (as high as 80 C, or a 45 s response) and cycling stability as well as a high degree of safety. Details about the  $\text{Na}_2\text{Ti}_3\text{O}_7 \rightleftharpoons \text{Na}_{3-x}\text{Ti}_3\text{O}_7$  sodium storage pathway are mentioned, along with its successful integration to a stable high energy density NIB highlighted by the highest voltage discharge plateau ever reported for any NIB which is not based on carbonaceous electrodes. The  $\text{Na}_2\text{Ti}_3\text{O}_7 \rightleftharpoons \text{Na}_{3-x}\text{Ti}_3\text{O}_7$  sodium storage pathway is currently the strongest contender for high performance NIB anodes having the potential to be applied not just for both load levelling and frequency regulation grid storage NIBs, but also perhaps in electric vehicles.



## 5.2 Introduction

$\text{Na}_2\text{Ti}_3\text{O}_7$  has been regarded as a promising NIB anode since its sodium storage activity was first discovered in 2011.<sup>57</sup> By storing two moles of sodium per mole of  $\text{Na}_2\text{Ti}_3\text{O}_7$  through a two-phase reaction mechanism between  $\text{Na}_2\text{Ti}_3\text{O}_7$  and  $\text{Na}_4\text{Ti}_3\text{O}_7$ , it has a high capacity (178 mAh/g) and very low and flat voltage of 0.4 V vs Na/Na<sup>+</sup> upon sodium extraction.<sup>57, 58, 88</sup> The major drawback of this material is its high polarization greater than 0.2 V. In fact, it has been proposed that the polarization is thermodynamically controlled (independent of particle size) and may not be below 0.225 V.<sup>59</sup> Such polarization > 0.2 V will result in an undesirably low RTEE. Furthermore, the fully sodiated phase,  $\text{Na}_4\text{Ti}_3\text{O}_7$ , has been shown to be unstable due to self-relaxation<sup>44</sup> which may be the reason for its poor cyclability observed in chapter 3 and also in previous studies.<sup>41, 44, 57, 59, 61, 88</sup>

The following results are an outcome of an observation made regarding the appearance of a new charge plateau during the galvanostatic cycling of  $\text{Na}_2\text{Ti}_3\text{O}_7$  when the lower cut-off voltage is altered, as described in chapter 3. In this chapter, we demonstrate the existence of a completely new intermediate phase between  $\text{Na}_2\text{Ti}_3\text{O}_7$  and  $\text{Na}_4\text{Ti}_3\text{O}_7$ ; that of  $\text{Na}_{3-x}\text{Ti}_3\text{O}_7$ . This new  $\text{Na}_2\text{Ti}_3\text{O}_7 \rightleftharpoons \text{Na}_{3-x}\text{Ti}_3\text{O}_7$  sodium storage pathway for  $\text{Na}_2\text{Ti}_3\text{O}_7$  results in a very low charge plateau at 0.2 V vs Na/Na<sup>+</sup> with negligible polarization which makes it the lowest activity redox voltage of any non-carbon based NIB anode. We also show that this pathway displays excellent rate performance, retaining its charge plateaus even till 80 C, resulting in impressive energy as well as power densities at high rates. Its sodium storage mechanism will be discussed with the help of EIS and *ex-situ* XRD, along with performance implications to full NIBs. Finally, its application to a stable non-carbon based NIB exhibiting the highest voltage plateau ever reported leading to high energy density will be demonstrated as a proof-of-concept.

## 5.3 Experimental Section

The same solvothermal synthesis approach to obtain  $\text{Na}_2\text{Ti}_3\text{O}_7/\text{C}$  utilized in chapter 3 was used in this work as well with most of the powder and electrochemical characterization being the same. Experimental details specific for this work are given below.

### 5.3.1 Synthesis of $\text{Na}_3\text{V}_2(\text{PO}_4)_2\text{F}_3/\text{C}$

$\text{Na}_3\text{V}_2(\text{PO}_4)_2\text{F}_3/\text{C}$  was synthesized using a soft-template approach using sodium fluoride, vanadium (III) acetylacetonate and ammonium dihydrogen phosphate as the sodium and fluorine sources, vanadium source and phosphate source, respectively. CTAB was used as the templating agent and was dissolved in a milli-Q water-absolute ethanol mixture. The resulting solution was stirred for 12 h and dried using a rotor-evaporator. The obtained powder was then calcined under argon gas flow to a temperature of 350 °C for 3 h followed by 650 °C for 3 h in a tube furnace to give the desired product. TGA analysis revealed the amount of *in-situ* carbon in the as-prepared  $\text{Na}_3\text{V}_2(\text{PO}_4)_2\text{F}_3/\text{C}$  to be around 25 wt%.

### 5.3.2 Electrochemical Characterization

To evaluate the sodium storage properties of the  $\text{Na}_2\text{Ti}_3\text{O}_7 \rightleftharpoons \text{Na}_{3-x}\text{Ti}_3\text{O}_7$  pathway, composite electrodes were made with  $\text{Na}_2\text{Ti}_3\text{O}_7/\text{C}$ : Super P carbon: CMC (or PVDF) in the weight ratio 80:10:10. First, required weights of  $\text{Na}_2\text{Ti}_3\text{O}_7/\text{C}$  and Super P carbon black were added to CMC-water solution (or PVDF- NMP solution). The resulting slurry was thoroughly mixed and then coated on an etched aluminium foil by the doctor blade method. The coated slurry was allowed to dry under vacuum for 12 h at 110 °C, before being pressed by a twin roller at a pressure of 37 psi. The final electrode loading of  $\text{Na}_2\text{Ti}_3\text{O}_7$  (excluding the *in-situ* carbon) was between 1.5 – 2.0  $\text{mg}/\text{cm}^2$ . These composite electrodes were used as the working electrode to construct

three-electrode and two-electrode cells. For the three-electrode cells, sodium metal (Merck) disk served as the counter electrode and a sodium metal ring served as the reference electrode. Commercial three-electrode cells provided by MTI (model number EQ-3ESTC15) were used. For the two-electrode cells, sodium metal disk served as the counter and reference electrodes, in a 2016-type coin cell. All cells were fabricated inside an Argon-filled glove box. 1M NaClO<sub>4</sub> in EC:PC (1:1 v/v), prepared in-house from commercially available NaClO<sub>4</sub> (Alfa Aesar) and solvents (Alfa Aesar and Sigma Aldrich for EC and PC, respectively), was used as the electrolyte in all cases unless otherwise specified. All other electrolytes were also prepared in-house from commercially available salts/solvents which were used as-received. The two-electrode cells were cycled on an Arbin battery tester (model BT2000, USA) while the three-electrode cells were cycled with a VMP3 instrument (Bio-Logic, France).

Please note that the voltage window to witness the Na<sub>2</sub>Ti<sub>3</sub>O<sub>7</sub> ⇌ Na<sub>3-x</sub>Ti<sub>3</sub>O<sub>7</sub> pathway depends on the loading of Na<sub>2</sub>Ti<sub>3</sub>O<sub>7</sub>, the C rate used to cycle, the electrolyte used, the electrode composition, the morphology of the synthesized Na<sub>2</sub>Ti<sub>3</sub>O<sub>7</sub> and on the quality of cell fabrication. As an indicator, the lower cut-off window was found to be around 0.16-0.15 V at a C/5 rate in 1M NaClO<sub>4</sub> in EC:PC (1:1 v/v) electrolyte in the present study using Na<sub>2</sub>Ti<sub>3</sub>O<sub>7</sub>/C. For thicker loadings (>2 mg/cm<sup>2</sup>) or for alternate electrolytes or for solid-state synthesized Na<sub>2</sub>Ti<sub>3</sub>O<sub>7</sub>, the lower cut-off window could be as low as 0.12-0.10 V even for the C/5 rate. It should, hence, be understood that the lower cut-off voltage can be sensitive and may require some optimization so as to isolate the Na<sub>2</sub>Ti<sub>3</sub>O<sub>7</sub> ⇌ Na<sub>3-x</sub>Ti<sub>3</sub>O<sub>7</sub> pathway.

For the full sodium-ion cell with Na<sub>3</sub>V<sub>2</sub>(PO<sub>4</sub>)<sub>2</sub>F<sub>3</sub>/C and Na<sub>2</sub>Ti<sub>3</sub>O<sub>7</sub>/C, a three-electrode cell (MTI Corporation, model number EQ-3ESTC15) was fabricated with the former as the cathode, the latter as the anode and a sodium metal ring serving as the reference. The Na<sub>3</sub>V<sub>2</sub>(PO<sub>4</sub>)<sub>2</sub>F<sub>3</sub>/C electrode consisted of Na<sub>3</sub>V<sub>2</sub>(PO<sub>4</sub>)<sub>2</sub>F<sub>3</sub>/C: CMC in the weight ratio of 90:10 (no external Super P carbon black was used). The loading of

$\text{Na}_3\text{V}_2(\text{PO}_4)_2\text{F}_3$  was around  $1.2 \text{ mg/cm}^2$ . In the full cell, the weight ratio of the active materials in the cathode to the anode was around 1.9:1, to account for the first cycle coulombic inefficiency of the anode. To stay consistent with the electrode loadings, the cross sectional area of the cathode and anode were different: the  $\text{Na}_3\text{V}_2(\text{PO}_4)_2\text{F}_3/\text{C}$  electrode's cross sectional area was  $2.0 \text{ cm}^2$ , while that for the  $\text{Na}_2\text{Ti}_3\text{O}_7/\text{C}$  electrode was  $0.95 \text{ cm}^2$ . For the pre-cycled full cell experiment, a similar three-electrode cell was constructed with the weight ratio of the active materials in the cathode to anode as 0.93:1. Both cathode and anode had a cross-sectional area of  $0.95 \text{ cm}^2$  and both were pre-cycled versus the sodium metal reference electrode for a few cycles prior to full cell cycling.

EIS studies were performed on a three-electrode cell using the VMP3 instrument (Bio-Logic, France) between  $1 \text{ MHz}$  to  $10 \text{ mHz}$  and the resulting Nyquist plots were fit using the EC-Lab software (ver. 10.19). The cell was discharged to the required voltage at  $C/5$  rate and allowed to rest for  $10 \text{ min}$  prior to measurements. CV studies were also performed in the VMP3 instrument at a scan rate of  $0.05 \text{ mV/s}$  in a two-electrode cell. For the Differential Scanning Calorimetry (DSC) study on sodiated  $\text{Na}_2\text{Ti}_3\text{O}_7/\text{C}$ , an electrode comprising just the as-prepared  $\text{Na}_2\text{Ti}_3\text{O}_7/\text{C}$  was prepared (without binder or conductive additives) and cycled in a 2016 coin-cell. The sodiated  $\text{Na}_2\text{Ti}_3\text{O}_7/\text{C}$  (that is,  $\text{Na}_{3-x}\text{Ti}_3\text{O}_7/\text{C}$ ) was hence obtained by opening the cell in the glove box, washing several times in PC, drying for  $16 \text{ h}$  in vacuum and finally scratching it from the aluminium current collector. The powder was then sealed under argon gas, taken to the DSC instrument and transferred into the DSC container in about  $10 \text{ s}$  in order to ensure minimal exposure to air during sample transfer. The container was then sealed and purged with  $\text{N}_2$ . DSC measurement was then performed on a TA Instrument 2920 in  $\text{N}_2$  atmosphere up to  $450 \text{ }^\circ\text{C}$  at a  $10 \text{ }^\circ\text{C/min}$  ramp rate.

### 5.3.3 *Ex-situ* XRD characterization

*Ex-situ* XRD experiments were also performed with a Bruker AXS D8 ADVANCE powder diffractometer using Cu K $\alpha$  radiation source and operated at 25 mA and 40 kV. For *ex-situ* XRD studies, solid-state synthesized Na<sub>2</sub>Ti<sub>3</sub>O<sub>7</sub> was used in order to obtain better counting statistics (and reflection intensities) owing to its micrometer-sized particles (please refer to chapter 3 for synthesis and material characterization details as well as for its sodium storage performance). The electrodes were made with solid-state synthesized Na<sub>2</sub>Ti<sub>3</sub>O<sub>7</sub>, Super P carbon black and CMC as the binder in the weight ratio 70:20:10 and were made to cycle to the respective states of discharge at C/5 rate corresponding to 1 mole sodium storage. The electrodes were then opened in a glove box, covered with Kapton Tape and all XRD patterns reported were obtained within 3 min as the discharged electrodes were found to be very unstable in air. The Kapton tape cover delayed phase transformation to Na<sub>2</sub>Ti<sub>3</sub>O<sub>7</sub> long enough to obtain reliable XRD patterns.

## 5.4 Results and Discussion

### 5.4.1 Na<sub>2</sub>Ti<sub>3</sub>O<sub>7</sub> $\rightleftharpoons$ Na<sub>3-x</sub>Ti<sub>3</sub>O<sub>7</sub> Sodium Storage Pathway

The first galvanostatic cycle of Na<sub>2</sub>Ti<sub>3</sub>O<sub>7</sub>/C cycled in a three-electrode cell between 2.5 and 0.01 V (deep discharged) is depicted in Fig. 5.1a at a C/2.5 rate (2.5 h charge/discharge corresponds to one mole of sodium storage per mole of Na<sub>2</sub>Ti<sub>3</sub>O<sub>7</sub> based on a theoretical capacity of 88.9 mAh/g). Please note that, similar to our definition of “theoretical capacity” for Na<sub>2</sub>Ti<sub>6</sub>O<sub>13</sub> being one mole sodium storage per mole of Na<sub>2</sub>Ti<sub>6</sub>O<sub>13</sub>, we have defined the “theoretical capacity” of this Na<sub>2</sub>Ti<sub>3</sub>O<sub>7</sub>  $\rightleftharpoons$  Na<sub>3-x</sub>Ti<sub>3</sub>O<sub>7</sub> sodium storage pathway as 88.9 mAh/g based solely on one mole of Na<sub>2</sub>Ti<sub>3</sub>O<sub>7</sub> storing one mole of sodium. In this voltage window, Na<sub>2</sub>Ti<sub>3</sub>O<sub>7</sub> can accommodate two moles of sodium, resulting in a charge (Na extraction) capacity of 178 mAh/g, consistent with previous reports.<sup>41, 44, 58-62, 88</sup> A closer look at the discharge

(Na intercalation) profile reveals a distinct voltage step (see inset of Fig. 5.1a). In fact, this voltage step can be clearly seen in the first discharge profiles of this material in other reports as well.<sup>41, 44, 59, 61, 62</sup> Such a voltage step was recently witnessed in the discharge profiles of  $\text{Na}_3\text{V}_2(\text{PO}_4)_3$  and  $\text{NaTi}_2(\text{PO}_4)_3$ .<sup>15, 89</sup> In those systems, the interaction of EC and PC based electrolyte solutions with the sodium metal CE was responsible for the observed step (refer to the previous chapter) and it did not reflect the behaviour of the WE.<sup>89</sup> Even though EC:PC solution was used in this work, the three-electrode cycling depicted in Fig. 1a with  $\text{Na}_2\text{Ti}_3\text{O}_7/\text{C}$  acting as the WE, a sodium metal disk acting as the CE and a sodium metal ring serving as a RE clearly reveals that the voltage step observed in  $\text{Na}_2\text{Ti}_3\text{O}_7$  actually arises due to the WE, as the WE-CE profile smoothly follows that of the WE. This observation implies that there must be an intermediate phase existing between  $\text{Na}_2\text{Ti}_3\text{O}_7$  and the deep discharged  $\text{Na}_4\text{Ti}_3\text{O}_7$ , as there are two separate voltage plateaus.

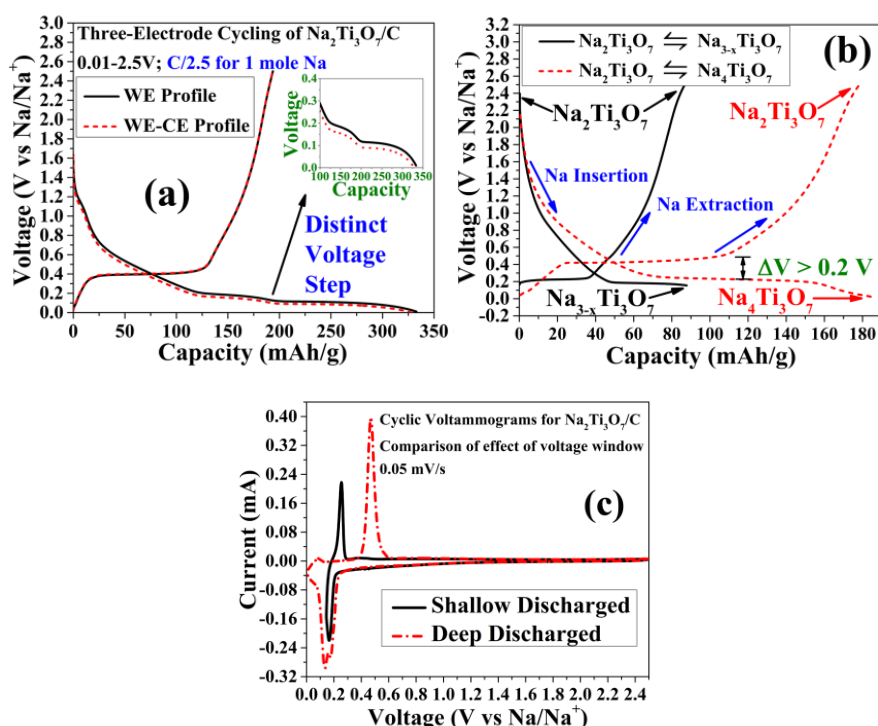


**Figure 5.1** | Illustration of the  $\text{Na}_2\text{Ti}_3\text{O}_7 \rightleftharpoons \text{Na}_{3-x}\text{Ti}_3\text{O}_7$  pathway. (a) Three-electrode cycling of a  $\text{Na}_2\text{Ti}_3\text{O}_7/\text{C}$  electrode from 0.01 – 2.5 V with the inset providing a zoomed-in view of the voltage step. (b) Representative galvanostatic cycling profiles at C/5 rate for the  $\text{Na}_2\text{Ti}_3\text{O}_7 \rightleftharpoons \text{Na}_{3-x}\text{Ti}_3\text{O}_7$  pathway (2.5 V – 0.155 V) and at C/2.5 rate for the  $\text{Na}_2\text{Ti}_3\text{O}_7 \rightleftharpoons \text{Na}_4\text{Ti}_3\text{O}_7$  pathway (2.5 – 0.01 V), clearly showing the negligible polarization of the former. (c) CV curves highlighting the new oxidation peak seen around 0.24 V for the  $\text{Na}_2\text{Ti}_3\text{O}_7 \rightleftharpoons \text{Na}_{3-x}\text{Ti}_3\text{O}_7$  pathway as opposed to the 0.47 V oxidation peak seen for the deep discharged material.

Indeed, if the lower cut-off voltage is limited to around 0.155 V (shallow discharged) instead of 0.01 V such that the material is allowed to intercalate sodium until the end of the upper discharge plateau (till the voltage step), the resulting galvanostatic profile of the charge curve is completely different (refer to Fig. 5.1b). The shallow discharged material now displays a flat charging plateau at 0.22 V, contrary to the 0.44 V plateau witnessed for  $\text{Na}_2\text{Ti}_3\text{O}_7$  that was deep discharged to 0.01 V. The obtained capacity of 87 mAh/g during charge indicates that almost one mole of sodium was inserted in the  $\text{Na}_2\text{Ti}_3\text{O}_7/\text{C}$  composite electrode during discharge, nominally forming “ $\text{Na}_{3-x}\text{Ti}_3\text{O}_7/\text{C}$ ”. Please note that the amorphous carbon matrix may have taken part in sodium storage. However, as demonstrated in chapter 3, since the same  $\text{Na}_2\text{Ti}_3\text{O}_7/\text{C}$  composite electrode delivered 178 mAh/g during charge if deep discharged (meaning two moles of sodium were inserted per mole of  $\text{Na}_2\text{Ti}_3\text{O}_7$  to form the established and well-understood phase  $\text{Na}_4\text{Ti}_3\text{O}_7$ <sup>44, 58</sup> at its deep discharged state), we do believe that the intermediate phase’s composition formed during shallow discharge is  $\text{Na}_{3-x}\text{Ti}_3\text{O}_7$  with  $x \approx 0$  (i.e.,  $\text{Na}_3\text{Ti}_3\text{O}_7$ ). Confirmation of the crystal structure and exact amount of sodium in the intermediate phase  $\text{Na}_{3-x}\text{Ti}_3\text{O}_7$  is currently in progress through *in-situ* XRD measurements. This charge plateau close to 0.2 V makes the  $\text{Na}_2\text{Ti}_3\text{O}_7 \rightleftharpoons \text{Na}_{3-x}\text{Ti}_3\text{O}_7$  sodium storage pathway the lowest redox voltage non-carbon based NIB anode ever reported, being 0.2 V lower than the previous lowest voltage non-carbon anode, viz. the  $\text{Na}_2\text{Ti}_3\text{O}_7 \rightleftharpoons \text{Na}_4\text{Ti}_3\text{O}_7$  pathway demonstrating its charge plateau at 0.44 V (please note that the charge profile of an anode is most relevant in full cells as the discharge voltage of cathode and charge voltage of anode determine the discharge voltage of the resulting full cell). Further to charge/discharge plateaus observed, CV curves (refer to Fig. 5.1c) support the notion of a distinctly different oxidation-reduction mechanism operating, with a clear oxidation peak at 0.24 V for the proposed  $\text{Na}_{3-x}\text{Ti}_3\text{O}_7 \rightarrow \text{Na}_2\text{Ti}_3\text{O}_7$  transition as opposed to that at 0.47 V for the  $\text{Na}_4\text{Ti}_3\text{O}_7 \rightarrow \text{Na}_2\text{Ti}_3\text{O}_7$  transition. Furthermore, the close proximity of the oxidation and reduction peaks for the  $\text{Na}_2\text{Ti}_3\text{O}_7 \rightleftharpoons \text{Na}_{3-x}\text{Ti}_3\text{O}_7$

pathway implies lower polarization and good reversibility.<sup>9</sup>

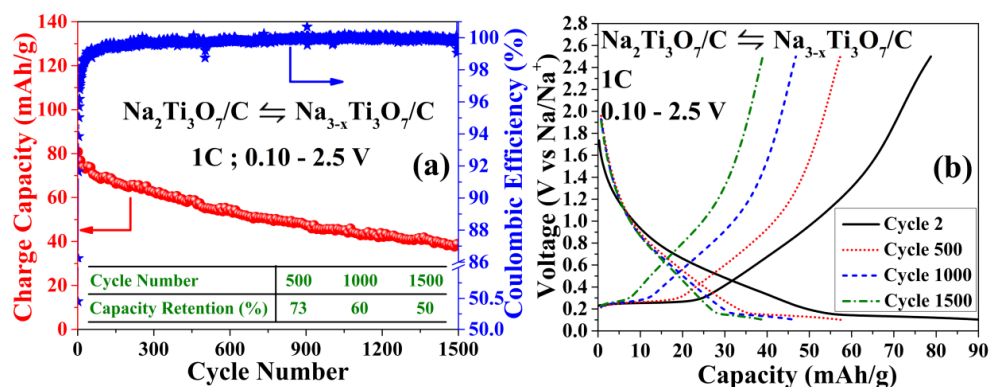


**Figure 5.2** | Long term cycling of the  $\text{Na}_2\text{Ti}_3\text{O}_7 \rightleftharpoons \text{Na}_{3-x}\text{Ti}_3\text{O}_7$  pathway in a sodium half cell over 1,500 cycles between 0.10 – 2.5 V. (a) The charge capacity and coulombic efficiency obtained versus cycle number indicating the good capacity retention and a very high, stable coulombic efficiency > 99.5 %. (b) The galvanostatic charge and discharge profiles of the 2<sup>nd</sup>, 500<sup>th</sup> and 1000<sup>th</sup> and 1500<sup>th</sup> cycle highlighting the fact that there is no discernible increase in the polarization of this pathway (difference between the charge and discharge plateaus) even after 1,500 cycles.

Indeed, the material can cycle stably and exceed 1,500 cycles at a 1 C rate with capacity retention of 73, 60 and 50% after 500, 1,000 and 1,500 cycles respectively, a stable  $\text{CE}_{\text{ff}}$  exceeding 99.5 % and negligible increase in polarization (refer to Fig. 5.2). Please note that such a long cycle life is reported for the first time for any NIB anode demonstrating the majority of its charge capacity below 0.8 V vs Na/Na<sup>+</sup>, to the best of our knowledge.<sup>6, 11, 21, 90</sup> Furthermore, as seen from Fig. 5.3a and Fig. 5.3b, it is impressive to note that the  $\text{Na}_2\text{Ti}_3\text{O}_7 \rightleftharpoons \text{Na}_{3-x}\text{Ti}_3\text{O}_7$  pathway demonstrates stable charge capacities of 86, 80, 78, 75, 71, 69, 64 and 55 mAh/g at various rates- 1/5, 1, 2, 5, 10, 20, 40 and 80 C, respectively. This capacity retention of 64 % in switching from a slow C/5 to an ultra-fast 80 C (45 s response) highlights the versatility of this sodium storage pathway. In particular, the polarization in this material became significant only at 40 and 80 C (see Fig. 5.3c). In fact, this pathway's polarization at a fast 10 C rate was the same as that displayed by the  $\text{Na}_2\text{Ti}_3\text{O}_7 \rightleftharpoons \text{Na}_4\text{Ti}_3\text{O}_7$  pathway at its slowest cycling rates. Moreover, the charge plateau was retained at all C rates (refer to Fig. 5.3a). The contribution of this charge plateau to the total charge capacity was found to be roughly around 41 % at all C rates, a fact that will be advantageous towards achieving high energy and power densities when this pathway is used in a



full cell (to be discussed later).

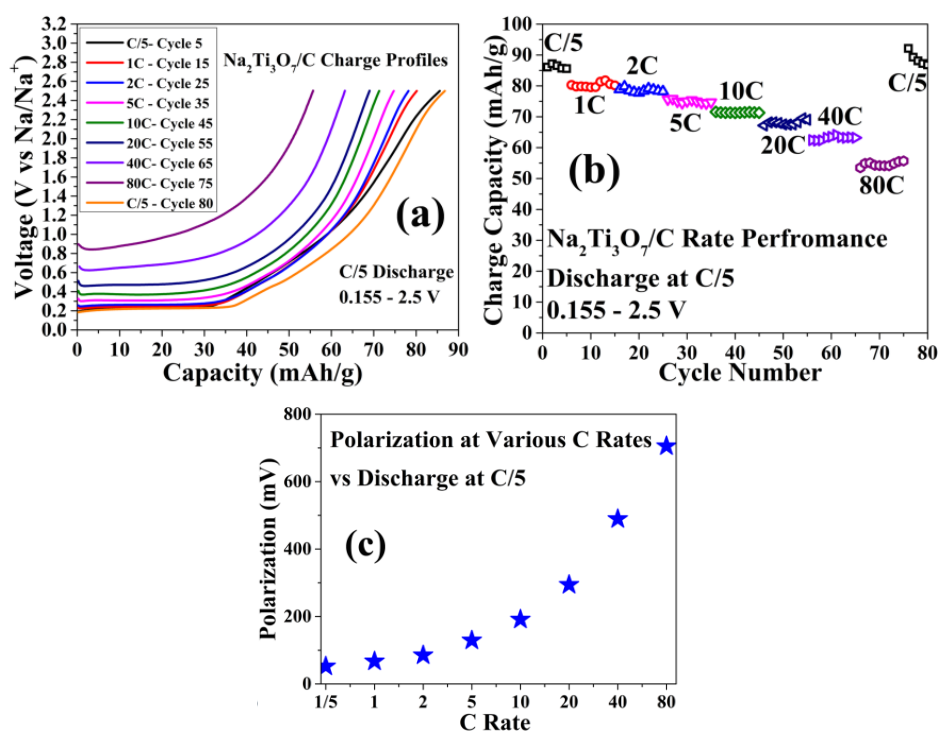


**Figure 5.3** | Rate performance of the  $\text{Na}_2\text{Ti}_3\text{O}_7 \rightleftharpoons \text{Na}_{3-x}\text{Ti}_3\text{O}_7$  pathway in a sodium half cell from C/5 to 80 C. (a) Charge profiles at various rates with the discharge being performed at C/5 rate. (b) The corresponding charge capacity versus cycle number. (c) Polarization (difference between the voltages of the charge plateaus at different C rates with respect to the voltage of the discharge plateau at C/5 rate) of the  $\text{Na}_2\text{Ti}_3\text{O}_7 \rightleftharpoons \text{Na}_{3-x}\text{Ti}_3\text{O}_7$  pathway at various C rates.

## 5.4.2 Understanding the $\text{Na}_2\text{Ti}_3\text{O}_7 \rightarrow \text{Na}_{3-x}\text{Ti}_3\text{O}_7 \rightarrow \text{Na}_4\text{Ti}_3\text{O}_7$

### Transition

In order to shed light into the drastic differences witnessed in the respective polarizations exhibited between the two pathways, EIS was performed using a three-electrode cell to obtain insight into their kinetic differences. The Nyquist plots are presented in Fig. 5.4a with the points selected for EIS shown in the top inset. The general shape of the Nyquist plots can be described as a series of semicircles obtained at high-medium frequencies, another semi-circle at medium-low frequencies, followed by a 45° straight line at even lower frequencies which tapers to high angles at the extremely low frequency points. These features are consistent with existing literature.<sup>83, 91</sup> To obtain physically meaningful interpretation, the intuitive circuit

model proposed by Aurbach *et al.* was followed.<sup>91</sup> In this model, each semi-circle can be represented by a parallel combination of a resistor and a capacitor.<sup>83, 91</sup> The semicircles obtained at high and medium frequencies are attributed to surface layers comprising the SEI formed on the  $\text{Na}_2\text{Ti}_3\text{O}_7$  electrode caused by electrolyte degradation at the highly reducing potentials during discharge.<sup>41</sup> This SEI is made of different layers and hence, more than one parallel R/C circuit connected in series is needed for its description as each layer has its own resistivity and capacity.<sup>29, 42, 43</sup> These SEI-related R/C circuits will be followed by another R/C circuit in series in the middle-low frequency domain which represents the charge transfer into the bulk of the active material ( $\text{Na}_{2+x}\text{Ti}_3\text{O}_7$  in this case). This last R/C circuit would represent the “charge transfer resistance,  $R_{ct}$ ” as often quoted in the literature which is deemed to be a gauge on how facile the sodium storage kinetics are in a material. At the next lower frequencies, ambipolar diffusion<sup>92</sup> of sodium into the bulk of the active material (governed by a material’s crystal structure) can be modelled as a  $45^\circ$  straight line Warburg element connected in series with these R/C circuits. Finally, at the very low frequencies, this straight line with unity slope gives way to a vertical line, which represents the theoretical intercalation capacity of the material, and can be represented by a capacitor connected in series with the rest of the circuit. Due to variables such as electrode thickness, varying particle size that affects the chemical diffusion of the intercalating ion and a limit on the low frequency used to sample the EIS spectra due to practical reasons, there is often overlap of the last two elements which prevents an observation of a straight, vertical line at the very low frequencies (refer to references 83 and 91 for more details). In the present study, one resistor accounting for the resistance offered by the electrolyte solution ( $R_{sol}$ ), two parallel R/C circuits connected in series accounting for the SEI ( $R_{SEI-I}/C_{SEI-I}$  and  $R_{SEI-II}/C_{SEI-II}$ ), one R/C element in series representing the charge transfer ( $R_{ct}/C_{ct}$ ) and a Warburg

element ( $W$ ) and a capacitor ( $C_{\text{int}}$ ) connected in series for the low frequency region, were found to adequately fit the observed patterns (refer to Fig. 5.4b).

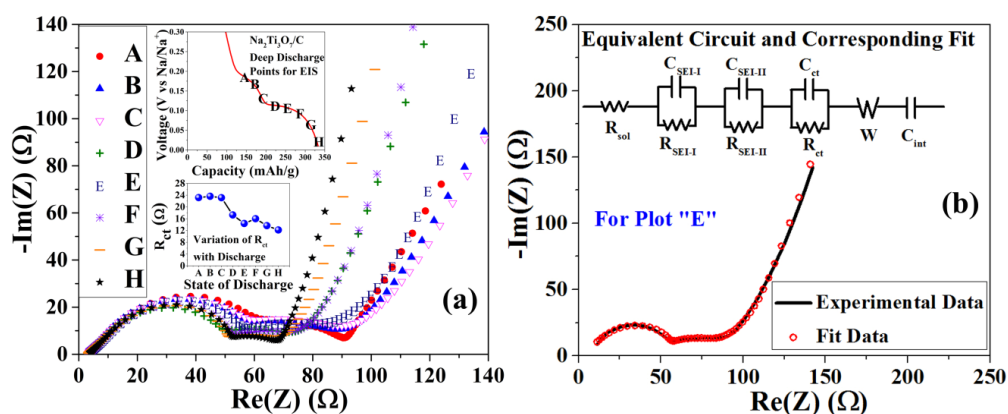


**Figure 5.4** | EIS analysis into the cause for the significant difference in polarization witnessed in the two pathways of sodium storage in  $\text{Na}_2\text{Ti}_3\text{O}_7/\text{C}$ . (a) Nyquist plots of the EIS analysis at various states of discharge (shown as the top inset) with the variation of  $R_{\text{ct}}$  with the state of discharge displayed as the bottom inset. (b) A typical fit obtained using the circuit model (shown on the top of the figure) with the experimental curve recorded at “E” from (a).

Upon application of the above model (refer to Fig. 5.4b), a good agreement with the observed pattern was obtained. A closer examination of Fig. 5.4a reveals very similar Nyquist plots obtained for the  $\text{Na}_2\text{Ti}_3\text{O}_7 \rightarrow \text{Na}_{3-x}\text{Ti}_3\text{O}_7$  (plots A - C) and  $\text{Na}_{3-x}\text{Ti}_3\text{O}_7 \rightarrow \text{Na}_4\text{Ti}_3\text{O}_7$  (plots D – H) transitions. In particular,  $R_{\text{ct}}$  (charge transfer resistance) was found to be similar for all spectra (see bottom inset of Fig. 5.4a). This fact is quite surprising since the significant differences in the polarization for the two types of pathways might have indicated differing charge transfer kinetics. Since this is not the case, the  $> 0.2 \text{ V}$  polarization for the  $\text{Na}_2\text{Ti}_3\text{O}_7 \rightleftharpoons \text{Na}_4\text{Ti}_3\text{O}_7$  pathway must be related to the chemical diffusion (ambipolar diffusion which involves coupled transport of Na-ion and electron within the crystal structure)<sup>92</sup> of sodium which would be dictated by different structural considerations, especially if there are different phases involved in sodium storage of  $\text{Na}_2\text{Ti}_3\text{O}_7$ .

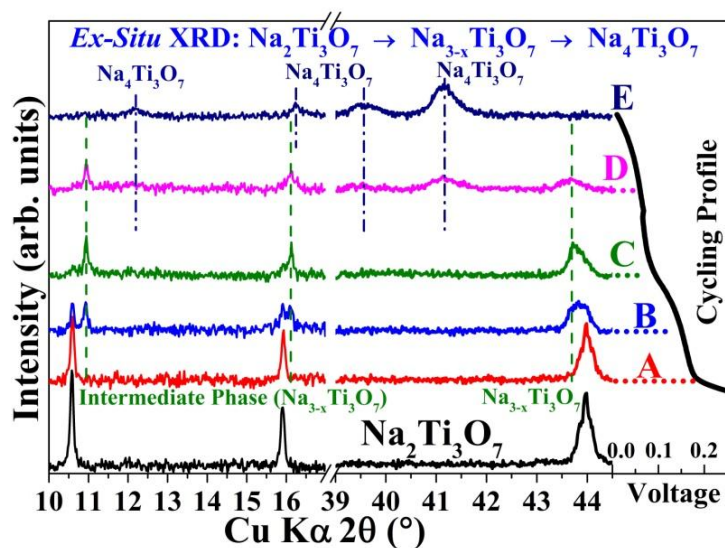


**Figure 5.5** | Structural changes occurring during the  $\text{Na}_2\text{Ti}_3\text{O}_7 \rightarrow \text{Na}_{3-x}\text{Ti}_3\text{O}_7 \rightarrow \text{Na}_4\text{Ti}_3\text{O}_7$  transition. *Ex-situ* XRD patterns on  $\text{Na}_2\text{Ti}_3\text{O}_7$  at various states of discharge as indicated by the cycling profile on the right.

To clarify this point, *ex-situ* XRD patterns were collected at different stages of the discharge (refer to Fig. 5.5). As discharge proceeded, the reflections associated with the parent  $\text{Na}_2\text{Ti}_3\text{O}_7$  phase decreased in intensity. Simultaneously, new sets of reflections appeared at  $2\theta = 10.93, 16.10$  and  $43.72^\circ$  and increased in intensity during the upper discharge plateau at the expense of those belonging to the parent  $\text{Na}_2\text{Ti}_3\text{O}_7$  phase (see patterns collected at points A, B and C in Fig. 5.5). At the end of the upper discharge plateau with the transformation of  $\text{Na}_2\text{Ti}_3\text{O}_7$  to  $\text{Na}_{3-x}\text{Ti}_3\text{O}_7$ , the reflections of  $\text{Na}_2\text{Ti}_3\text{O}_7$  disappeared (point C). Hence, it appears that the  $\text{Na}_2\text{Ti}_3\text{O}_7 \rightleftharpoons \text{Na}_{3-x}\text{Ti}_3\text{O}_7$  pathway proceeds through a two-phase reaction mechanism and that  $\text{Na}_{3-x}\text{Ti}_3\text{O}_7$  is a stable phase that forms at the end of the upper discharge plateau. Further discharge from point C (onto the lower discharge plateau represented by points D and E) systematically gave rise to a new set of reflections at  $2\theta = 12.2, 16.23, 39.56$  and  $41.17^\circ$  while those belonging to  $\text{Na}_{3-x}\text{Ti}_3\text{O}_7$  decreased progressively before disappearing. These new reflections are consistent with those reported for  $\text{Na}_4\text{Ti}_3\text{O}_7$ <sup>44, 58</sup> implying that the  $\text{Na}_{3-x}\text{Ti}_3\text{O}_7 \rightarrow \text{Na}_4\text{Ti}_3\text{O}_7$  transformation is also two-phase in nature. Therefore, in the course of sodium intercalation,  $\text{Na}_2\text{Ti}_3\text{O}_7$  exhibits two

different voltage plateaus, with each plateau associated with a different two-phase reaction mechanism. The fact that two discharge plateaus are witnessed upon deep discharge (to 0.01 V) corresponding to the  $\text{Na}_2\text{Ti}_3\text{O}_7 \rightarrow \text{Na}_{3-x}\text{Ti}_3\text{O}_7$  and  $\text{Na}_{3-x}\text{Ti}_3\text{O}_7 \rightarrow \text{Na}_4\text{Ti}_3\text{O}_7$  two-phase reactions respectively, but only the 0.44 V charge plateau (corresponding to that for the established  $\text{Na}_4\text{Ti}_3\text{O}_7 \rightarrow \text{Na}_2\text{Ti}_3\text{O}_7$  two-phase reaction) is witnessed during charge, implies an irreversible phase transformation during deep discharge to 0.01 V which causes the  $\text{Na}_2\text{Ti}_3\text{O}_7 \rightleftharpoons \text{Na}_{3-x}\text{Ti}_3\text{O}_7$  pathway to be lost in the subsequent cycles. If this was not the case, the charge cycle of a deep discharged  $\text{Na}_2\text{Ti}_3\text{O}_7$  electrode should have also displayed two separate charge plateaus. In summary, during deep discharge,  $\text{Na}_2\text{Ti}_3\text{O}_7$  forms the distinct phases of  $\text{Na}_{3-x}\text{Ti}_3\text{O}_7$  and  $\text{Na}_4\text{Ti}_3\text{O}_7$ , but during charge,  $\text{Na}_4\text{Ti}_3\text{O}_7$  transforms to  $\text{Na}_2\text{Ti}_3\text{O}_7$  directly without the formation of the  $\text{Na}_{3-x}\text{Ti}_3\text{O}_7$  phase. Hence, to witness the  $\text{Na}_2\text{Ti}_3\text{O}_7 \rightleftharpoons \text{Na}_{3-x}\text{Ti}_3\text{O}_7$  pathway over many cycles, it is imperative that the irreversible transformation of  $\text{Na}_{3-x}\text{Ti}_3\text{O}_7$  to  $\text{Na}_4\text{Ti}_3\text{O}_7$  is avoided by appropriately limiting the extent of sodiation during discharge (by limiting the voltage window).

This irreversibility explains the cause and subsequent loss of the 0.25 V charge plateau witnessed by us previously in chapter 3.<sup>88</sup> In the previous study, the lower cut-off voltage of 0.1 V caused the cycling to stop around the middle-end region of the lower discharge plateau. Hence, the first charge cycle displayed an incomplete plateau for the  $\text{Na}_{3-x}\text{Ti}_3\text{O}_7 \rightarrow \text{Na}_2\text{Ti}_3\text{O}_7$  transition at 0.25 V (for the partial  $\text{Na}_{3-x}\text{Ti}_3\text{O}_7$  that had not yet irreversibly transformed to  $\text{Na}_4\text{Ti}_3\text{O}_7$ ) as well as the expected charge plateau around 0.44 V of the  $\text{Na}_4\text{Ti}_3\text{O}_7 \rightarrow \text{Na}_2\text{Ti}_3\text{O}_7$  pathway (for the majority of  $\text{Na}_{3-x}\text{Ti}_3\text{O}_7$  that had irreversibly transformed to  $\text{Na}_4\text{Ti}_3\text{O}_7$ ). However, with each such discharge, the  $\text{Na}_2\text{Ti}_3\text{O}_7 \rightleftharpoons \text{Na}_{3-x}\text{Ti}_3\text{O}_7$  pathway was progressively lost due to the structural irreversibility causing a gradual vanishing of 0.25 V charge plateau.<sup>88</sup> The different phases ( $\text{Na}_2\text{Ti}_3\text{O}_7$ ,  $\text{Na}_{3-x}\text{Ti}_3\text{O}_7$  and  $\text{Na}_4\text{Ti}_3\text{O}_7$ ) involved in the sodium storage in  $\text{Na}_2\text{Ti}_3\text{O}_7$  may give rise to different sodium migration routes which would likely

affect the chemical diffusion of sodium in them. This may help explain the large difference seen in the polarization of the  $\text{Na}_2\text{Ti}_3\text{O}_7 \rightleftharpoons \text{Na}_{3-x}\text{Ti}_3\text{O}_7$  and the  $\text{Na}_2\text{Ti}_3\text{O}_7 \rightleftharpoons \text{Na}_4\text{Ti}_3\text{O}_7$  pathways. Atomistic simulation studies on the resolved crystal structure of  $\text{Na}_{3-x}\text{Ti}_3\text{O}_7$  obtained from the *in-situ* XRD experiments would help in resolving this point. However, based on the similarity of the XRD reflection positions of  $\text{Na}_2\text{Ti}_3\text{O}_7$  and  $\text{Na}_{3-x}\text{Ti}_3\text{O}_7$ , two speculations about the crystal structure of  $\text{Na}_{3-x}\text{Ti}_3\text{O}_7$  can be drawn from the *ex-situ* XRD studies. Firstly, it can be speculated that these phases ( $\text{Na}_2\text{Ti}_3\text{O}_7$  and  $\text{Na}_{3-x}\text{Ti}_3\text{O}_7$ ) may be very similar to each other in terms of crystallographic parameters. This may perhaps result in similar sodium migration routes in them which may explain the ease of sodium insertion/extraction between these two phases contributing to the minimal polarization of this pathway. Secondly, it can also indicate minimal volume variation experienced by the crystal structure in going from  $\text{Na}_2\text{Ti}_3\text{O}_7$  to  $\text{Na}_{3-x}\text{Ti}_3\text{O}_7$ , a fact which would help explain the long cycle life of the  $\text{Na}_2\text{Ti}_3\text{O}_7 \rightleftharpoons \text{Na}_{3-x}\text{Ti}_3\text{O}_7$  sodium storage pathway.

### 5.4.3 Safety of $\text{Na}_2\text{Ti}_3\text{O}_7 \rightleftharpoons \text{Na}_{3-x}\text{Ti}_3\text{O}_7$ Pathway

A very important requirement for the commercial prospects of this reaction pathway would be the thermal stability of the sodiated material, i.e.,  $\text{Na}_{3-x}\text{Ti}_3\text{O}_7$ . The risks of thermal runaway in a battery would be compounded if there are any exothermic reactions abetting it. It is a known fact that a battery is most unstable at the fully charged state (the cathode would be de-sodiated and the anode would be sodiated). Hence, a DSC experiment was conducted on  $\text{Na}_{3-x}\text{Ti}_3\text{O}_7/\text{C}$  (electrochemically stopped at this composition) to search for the onset of an exothermic peak and the result is shown in Fig. 5.6a.  $\text{Na}_{3-x}\text{Ti}_3\text{O}_7/\text{C}$  demonstrates its first exothermic peak at a relatively safe temperature of 376 °C. The inherent high degree of safety for the  $\text{Na}_2\text{Ti}_3\text{O}_7 \rightleftharpoons \text{Na}_{3-x}\text{Ti}_3\text{O}_7$  sodium storage pathway is also an attractive feature since NIBs incorporating this pathway may afford to have no strict battery management systems

which would possibly reduce their cost. Of equal importance is that the sodium storage performance of  $\text{Na}_2\text{Ti}_3\text{O}_7 \rightleftharpoons \text{Na}_{3-x}\text{Ti}_3\text{O}_7$  pathway is similar in different electrolytes that use salts other than the explosive  $\text{NaClO}_4$  which is the most widely used salt in NIB research currently (refer to Fig. 5.6b). This flexibility in switching to safer salts without a drop in performance is an added benefit. Further electrolyte optimization is currently in progress.

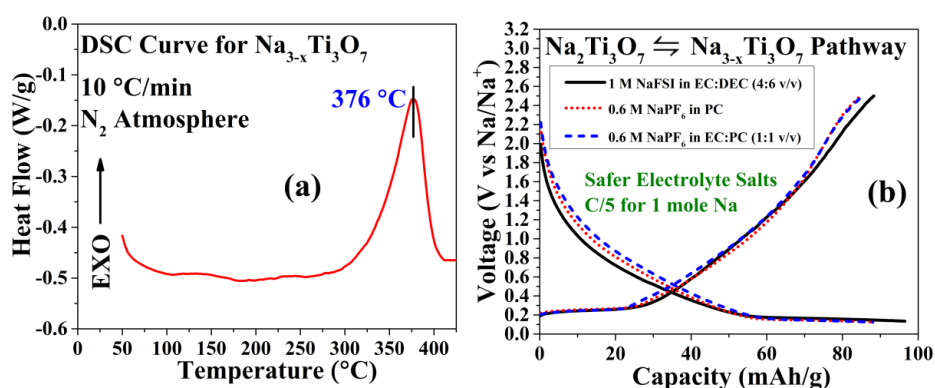


**Figure 5.6** | Illustration of the high degree of safety exhibited by the  $\text{Na}_2\text{Ti}_3\text{O}_7 \rightleftharpoons \text{Na}_{3-x}\text{Ti}_3\text{O}_7$  sodium storage pathway. (a) DSC curves on  $\text{Na}_2\text{Ti}_3\text{O}_7/\text{C}$  that was sodiated to  $\text{Na}_{3-x}\text{Ti}_3\text{O}_7/\text{C}$ . To eliminate influences from the binder and carbon black,  $\text{Na}_2\text{Ti}_3\text{O}_7/\text{C}$  was coated on an aluminium current collector without the binder and conductive additive and made to cycle in a half cell. The DSC curve shows good thermal stability exhibited by  $\text{Na}_{3-x}\text{Ti}_3\text{O}_7/\text{C}$  with the first exothermic peak appearing only at  $376^{\circ}\text{C}$ . (b) Galvanostatic cycling of as-prepared  $\text{Na}_2\text{Ti}_3\text{O}_7/\text{C}$  composite electrode in different electrolytes, illustrating that the  $\text{Na}_2\text{Ti}_3\text{O}_7 \rightleftharpoons \text{Na}_{3-x}\text{Ti}_3\text{O}_7$  pathway can be reversible in a host of different and safer electrolytes. This versatility means the use of the explosive  $\text{NaClO}_4$  salt would not be necessary. Please note that a representative C/5 cycle is presented.

#### 5.4.4 $\text{Na}_2\text{Ti}_3\text{O}_7 \rightleftharpoons \text{Na}_{3-x}\text{Ti}_3\text{O}_7$ Anode Application to NIBs

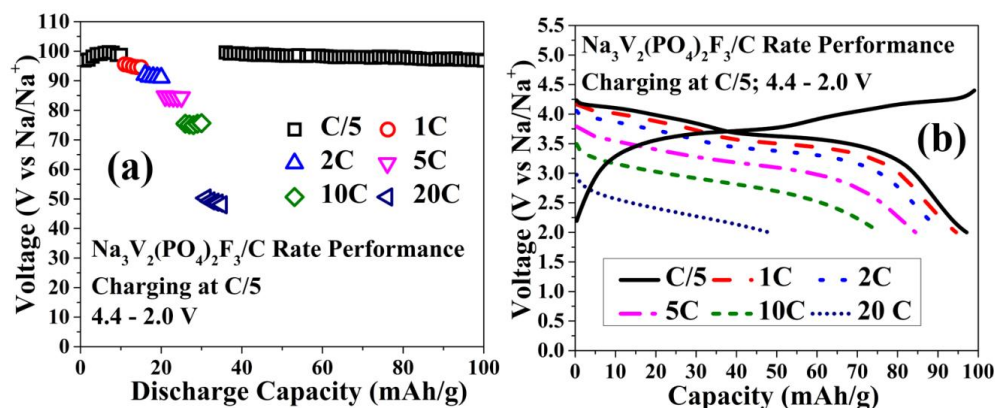


**Figure 5.7** | Sodium storage performance of  $\text{Na}_3\text{V}_2(\text{PO}_4)_2\text{F}_3/\text{C}$  cathode in a sodium half cell. (a) Rate capability test from C/5 to 20 C with charging performed at C/5. Excellent capacity retention is obtained at all rates. (b) The corresponding discharge curves at the various rates with a sample C/5 charging curve. Due to the high polarization, the material discharges at lower voltage values as the C rate increases. Due to the imposed lower cut-off voltage at 2.0 V, the material is not allowed to fully store sodium at high rates as the high polarization causes premature stoppage of cycling.

The major advantage of the reaction pathway proposed in this article is its very low voltage plateau. This would translate into a high voltage NIB if paired with an appropriate cathode. To this end,  $\text{Na}_3\text{V}_2(\text{PO}_4)_2\text{F}_3$  was chosen as a suitable cathode since it has been shown to possess two plateaus in its galvanostatic cycling at high voltages of 3.7 and 4.2 V vs  $\text{Na}/\text{Na}^+$ , storing sodium through a solid-solution mechanism.<sup>12</sup> We have synthesized  $\text{Na}_3\text{V}_2(\text{PO}_4)_2\text{F}_3$  through a soft-template method and the resulting carbon coated  $\text{Na}_3\text{V}_2(\text{PO}_4)_2\text{F}_3$ , termed “ $\text{Na}_3\text{V}_2(\text{PO}_4)_2\text{F}_3/\text{C}$ ”, demonstrates excellent cycling stability over 100 cycles and good rate capability as presented in Fig. 5.7. A full cell in a three-electrode set-up was hence constructed with  $\text{Na}_3\text{V}_2(\text{PO}_4)_2\text{F}_3/\text{C}$  as the cathode,  $\text{Na}_2\text{Ti}_3\text{O}_7/\text{C}$  as the anode and a sodium metal ring serving as the RE.

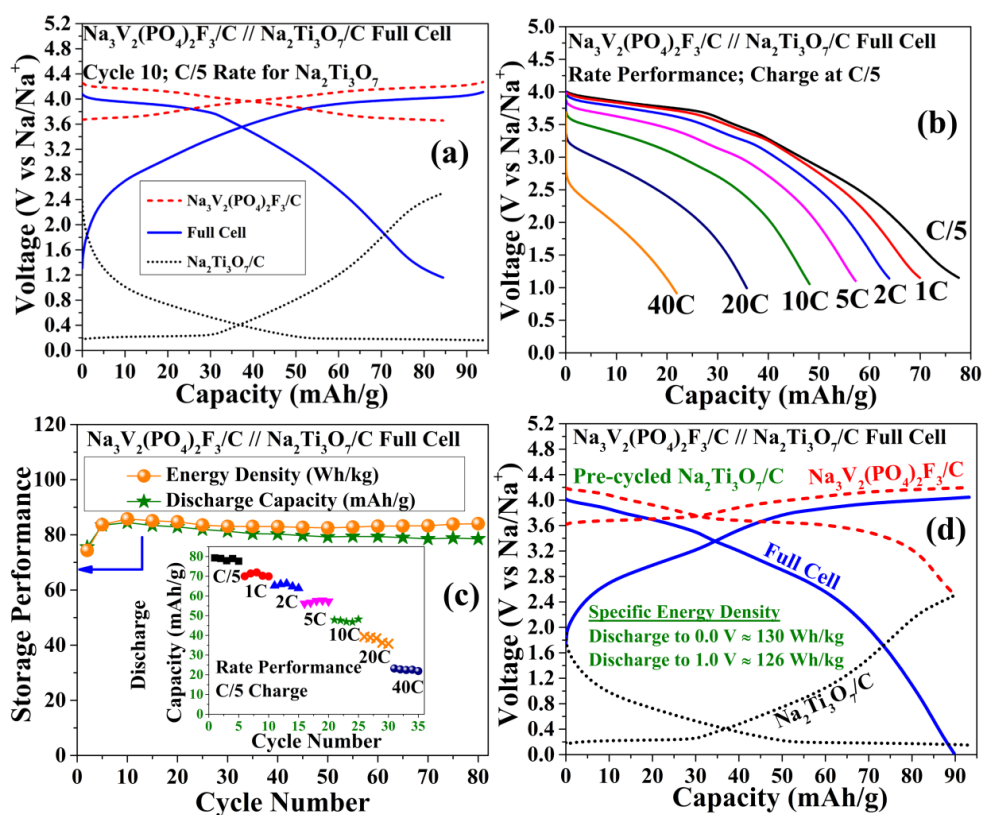


**Figure 5.8** | Sodium storage performance of a full cell employing the  $\text{Na}_2\text{Ti}_3\text{O}_7 \rightleftharpoons \text{Na}_{3-x}\text{Ti}_3\text{O}_7$  sodium storage pathway in a three-electrode cell. (a) The C/5 cycling of a full NIB with  $\text{Na}_3\text{V}_2(\text{PO}_4)_2\text{F}_3/\text{C}$  as the cathode and the  $\text{Na}_2\text{Ti}_3\text{O}_7 \rightleftharpoons \text{Na}_{3-x}\text{Ti}_3\text{O}_7$  pathway as the anode with sodium metal as the RE in a three-electrode cell. (b) Discharge profiles of such a full cell at various rates with the charging performed at C/5. (c) Illustration of stable cycling of this full cell over 80 cycles. The inset depicts stable cycling at various rates, whose profiles were shown in (b). (d) The full cell's cycling profile at C/5 rate (calculated for  $\text{Na}_2\text{Ti}_3\text{O}_7$ ) if  $\text{Na}_2\text{Ti}_3\text{O}_7/\text{C}$  is pre-cycled prior to full cell cycling. Please note: all capacity values are with respect to the weight of  $\text{Na}_2\text{Ti}_3\text{O}_7$ , while all energy density values are with respect to the cumulative weight of  $\text{Na}_3\text{V}_2(\text{PO}_4)_2\text{F}_3$  and  $\text{Na}_2\text{Ti}_3\text{O}_7$ .



A representative cycle at  $C/5$  rate (calculated for the anode) is presented in Fig. 5.8a. One can notice that due to the high discharge plateau of  $\text{Na}_3\text{V}_2(\text{PO}_4)_2\text{F}_3/\text{C}$  and the very low charge plateau of  $\text{Na}_2\text{Ti}_3\text{O}_7/\text{C}$ , the full cell's discharge plateau starts from 4.0 V and continues to about 3.7 V accounting for 35 mAh/g (or 42 % of the total discharge capacity) before displaying a sloping profile. This NIB exhibited excellent and stable high rate performance. As shown by Fig. 5.8b and inset of Fig. 5.8c, a full NIB incorporating this  $\text{Na}_2\text{Ti}_3\text{O}_7 \rightleftharpoons \text{Na}_{3-x}\text{Ti}_3\text{O}_7$  reaction pathway could be cycled up to 40 C with the polarization becoming a significant factor only from 20 C, chiefly due to the large polarization of the  $\text{Na}_3\text{V}_2(\text{PO}_4)_2\text{F}_3/\text{C}$  cathode (see Fig. 5.7b). Furthermore, this fabricated NIB could cycle with essentially no capacity fade in 80 cycles at a slow  $C/5$  rate (refer to Fig. 5.8c). Owing to the very high voltage plateau, this full cell demonstrated a stable energy density of 85 Wh/kg based on the weights of the active materials in the anode as well as the cathode. The specific energy density of this full cell could have been much higher had the first cycle  $\text{CE}_{\text{ff}}$  of the anode been 100 % as more than double the amount of cathode had to be used to compensate for the first cycle ICL of the anode. To demonstrate this, a similar full cell was fabricated but with the  $\text{Na}_2\text{Ti}_3\text{O}_7/\text{C}$  anode pre-cycled previously versus Na metal and a correspondingly lighter  $\text{Na}_3\text{V}_2(\text{PO}_4)_2\text{F}_3/\text{C}$  cathode used. With this arrangement, the full cell delivered an impressive 130 Wh/kg upon discharge to 0.0 V (refer to Fig. 5.8d).

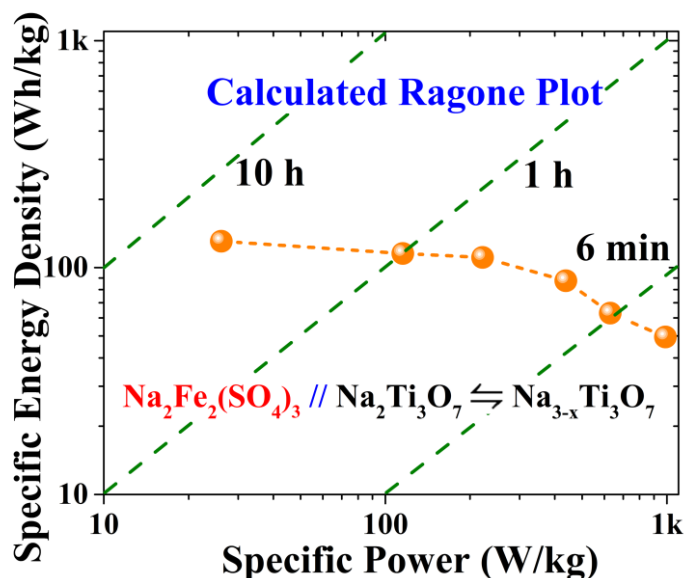


**Figure 5.9** | Calculated Ragone plot if the  $\text{Na}_2\text{Ti}_3\text{O}_7 \rightleftharpoons \text{Na}_{3-x}\text{Ti}_3\text{O}_7$  pathway were to be paired with the  $\text{Na}_2\text{Fe}_2(\text{SO}_4)_3$  cathode in a full NIB. The calculations assume no first cycle ICL of the anode and the values are based on the active material weights in the cathode and anode (the weights being correspondingly balanced). One can see that such an NIB, composed of earth-abundant elements, would not only be inexpensive, but would have the potential for excellent performance especially at high rates where the full benefit of the low and flat charge plateau of the  $\text{Na}_2\text{Ti}_3\text{O}_7 \rightleftharpoons \text{Na}_{3-x}\text{Ti}_3\text{O}_7$  pathway can be experienced. The Ragone plots were calculated from the discharge curves of  $\text{Na}_2\text{Fe}_2(\text{SO}_4)_3$  given in reference 16 and the charge curves of this pathway (shown in Fig. 5.3a).

Due to inevitable electrolyte decomposition forming a SEI<sup>29, 42, 43</sup> on the anode at such reducing voltages close to 0 V vs  $\text{Na}/\text{Na}^+$ , a low first cycle  $\text{CE}_{\text{ff}}$  can always be expected for any NIB anode operating close to 0 V as electrons (and hence, sodium ions) are consumed towards reducing the electrolyte. If an appropriate method can be devised to achieve a first cycle  $\text{CE}_{\text{ff}}$  of 100 % for low voltage NIB anodes, the energy density of a full cell incorporating this pathway as an anode can be quite impressive (demonstrated in Fig. 5.8d), especially at high rates where the full impact of its low voltage plateau is experienced. To showcase the pathway's potential as a high performance NIB anode, a calculated Ragone plot of this pathway against the recently discovered  $\text{Na}_2\text{Fe}_2(\text{SO}_4)_3$  cathode<sup>16</sup> is presented in Fig. 5.9 using the assumption of the first cycle  $\text{CE}_{\text{ff}}$  to be 100 %. In this way, the true performance of this new pathway would be captured without the ICL due to electrolyte decomposition decreasing the energy and power densities. These results, highlighted by a high 1000

W/kg and 50 Wh/kg response within a very fast 3 min, point to the potential use of this pathway not just for grid storage NIB application, but also perhaps in electric vehicles, provided the first cycle  $CE_{ff}$  is increased to near 100 %. Partial success has been achieved in this endeavour, with the use of CMC as binder instead of the traditional binder PVDF; the first cycle  $CE_{ff}$  increased from just 27 % to almost 50 % if CMC is adopted as the binder instead of PVDF (refer to Fig. 5.10), mirroring the positive impact of CMC in reducing the first cycle ICL on antimony electrodes.<sup>42</sup> It is hoped that the research progress in NIBs can mimic that of LIBs with respect to the important issue of eliminating this first cycle ICL: by appropriate modifications, the first cycle  $CE_{ff}$  in the low voltage graphite anode for LIBs has been improved from just 22 % to over 89 %.<sup>93</sup>

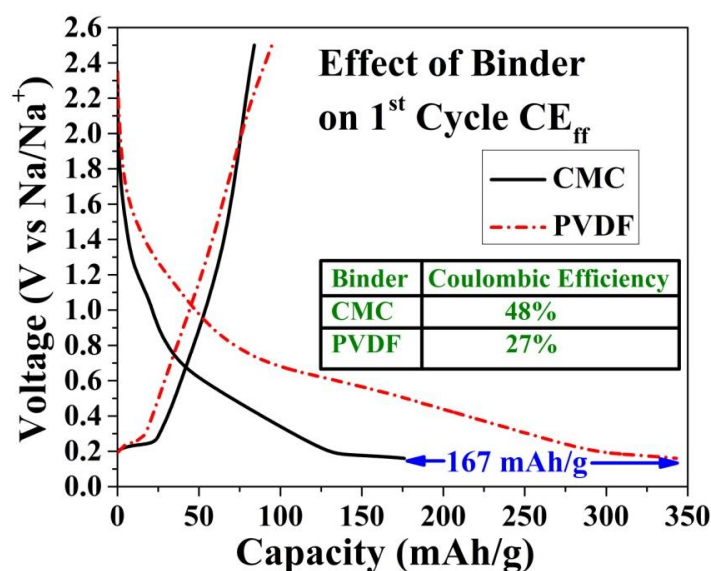


**Figure 5.10** | Comparison of the first cycle coulombic efficiency ( $CE_{ff}$ ) with different binders (CMC or PVDF). Use of CMC results in a dramatic improvement in the first cycle  $CE_{ff}$  with a huge reduction in the first cycle ICL by 167 mAh/g. For both electrodes, the same loading was used between  $Na_2Ti_3O_7/C$ , Super P carbon black and binder in the same electrode weight ratio between these components (80:10:10).

#### 5.4.5 Potential of the $Na_2Ti_3O_7 \rightleftharpoons Na_{3-x}Ti_3O_7$ Pathway in Grid Storage NIBs

In this chapter, the  $Na_2Ti_3O_7 \rightleftharpoons Na_{3-x}Ti_3O_7$  sodium storage pathway has been shown to fulfil all qualities expected of an electrode material to be employed in grid storage

batteries, except for one: an ultra-long cycle life exceeding 4,000 cycles. Actually, a cycle life of 4,000 cycles can be expected for this pathway not only due to the expected minimal volume variation, but also due to the fact that at such low voltages, the stability and passivating ability of the SEI is a critical parameter towards achieving a long cycle life.<sup>21, 94</sup> Further research needs to be expended towards optimizing the stability of the SEI. This would be a crucial factor as ultra-long cycle life has been displayed by NIB anode materials in half cells which were not discharged to such low voltages. For example, the sodium titanate phase  $\text{Na}_2\text{Ti}_6\text{O}_{13}$  discussed in chapter 2 also experienced minimal volume variation in the course of sodium storage and displayed a cycle life in excess of 5,000 cycles.<sup>72</sup> In that case, the voltage window of 2.5 – 0.5 V limited the growth of the SEI and hence, it was not as crucial of a factor in long-term cycling as it was in this case.

In addition, care has to be taken towards interpreting electrochemical cycling results in a half cell, that is, cycling against sodium metal. This is because while sodium may be a good reference electrode, it is not a good counter electrode as it is covered with passivation layers in the carbonate-based electrolytes commonly used in lithium/sodium based batteries, as mentioned in chapter 4.<sup>89</sup> Moreover, it has been demonstrated recently that this passivation layer interface of sodium metal adversely affects long term cycling due to decomposition of the electrolyte.<sup>95</sup> Hence, the same anode could be expected to cycle with much improved capacity retention if cycled in a full cell which does not contain the unstably passivated sodium metal. This stable cycling in a full NIB was already demonstrated for the  $\text{Na}_2\text{Ti}_3\text{O}_7 \rightleftharpoons \text{Na}_{3-x}\text{Ti}_3\text{O}_7$  sodium storage pathway (refer to Fig. 5.8c).

## 5.5 Summary

A new anode for NIB application is reported based on  $\text{Na}_2\text{Ti}_3\text{O}_7$ . By restricting the voltage window such that  $\text{Na}_2\text{Ti}_3\text{O}_7$  is made to store  $\leq$  one mole of sodium as opposed

to the conventionally-used two mole sodium storage of this material, a reversible charge capacity of 89 mAh/g can be obtained with the lowest charge plateau ever reported for any non-carbon based NIB anode at 0.2 V vs Na/Na<sup>+</sup>. This Na<sub>2</sub>Ti<sub>3</sub>O<sub>7</sub> ⇌ Na<sub>3-x</sub>Ti<sub>3</sub>O<sub>7</sub> sodium storage pathway demonstrates minimal polarization, excellent rate capability with stable cycling up to an ultra-fast 80 C rate (45 s response) and good thermal stability in the sodiated state with no exothermic peaks below 350 °C. *Ex-situ* XRD analysis revealed that Na<sub>2</sub>Ti<sub>3</sub>O<sub>7</sub> undergoes two separate two-phase reactions, with each such reaction eliciting a voltage plateau during discharge. Furthermore, it was discovered that the second mole of sodium storage causes an irreversible phase transformation which causes the loss of the Na<sub>2</sub>Ti<sub>3</sub>O<sub>7</sub> ⇌ Na<sub>3-x</sub>Ti<sub>3</sub>O<sub>7</sub> pathway in subsequent cycles. EIS studies surprisingly showed no major kinetic differences between the Na<sub>2</sub>Ti<sub>3</sub>O<sub>7</sub> → Na<sub>3-x</sub>Ti<sub>3</sub>O<sub>7</sub> and Na<sub>3-x</sub>Ti<sub>3</sub>O<sub>7</sub> → Na<sub>4</sub>Ti<sub>3</sub>O<sub>7</sub> sodium storage transitions, indicating the role of the structure in the large polarization of the Na<sub>2</sub>Ti<sub>3</sub>O<sub>7</sub> ⇌ Na<sub>4</sub>Ti<sub>3</sub>O<sub>7</sub> pathway (> 0.2 V). The Na<sub>2</sub>Ti<sub>3</sub>O<sub>7</sub> ⇌ Na<sub>3-x</sub>Ti<sub>3</sub>O<sub>7</sub> pathway's utilization in a full cell paired with the high voltage cathode Na<sub>3</sub>V<sub>2</sub>(PO<sub>4</sub>)<sub>2</sub>F<sub>3</sub> was shown to lead to a NIB displaying the highest voltage plateau for any non-carbon based NIB (between 4.0 – 3.7 V) ever reported along with high energy density, good rate performance and cycling stability. It is believed that the Na<sub>2</sub>Ti<sub>3</sub>O<sub>7</sub> ⇌ Na<sub>3-x</sub>Ti<sub>3</sub>O<sub>7</sub> sodium storage pathway utilizing earth-abundant elements holds great promise for a low cost, safe and stable NIB meant for diverse applications demonstrating high energy and power densities especially at high rates and high RTEE, if paired with an appropriate cathode and the first cycle CE<sub>ff</sub> is improved. In particular, this pathway's application to grid storage batteries for both load levelling and frequency regulation seems very appealing even with the existing first cycle CE<sub>ff</sub>.



## **Chapter 6 | Conclusions and Future Research**

### **Directions**

## 6.1 Conclusions

The research described in the thesis mainly aims to find a suitable anode material optimized for grid storage NIB application, to complement promising NIB cathodes. Since cost is a big driving factor for grid storage batteries, an approach towards utilizing earth-abundant elements in these anodes was taken. In this regard, two different phases of the sodium titanates were studied:  $\text{Na}_2\text{Ti}_6\text{O}_{13}$  and  $\text{Na}_2\text{Ti}_3\text{O}_7$ . Efforts were made towards achieving the following important performance metrics for these NIB anodes for grid storage applications: low cost, long cycle life (in excess of 4,000 cycles), high RTEE and a high degree of safety. Simultaneously, the desire to increase the specific energy densities of these anodes by increasing their specific capacities and reducing their operating voltages guided the research to explore various synthesis and optimization strategies. With this in mind, the major conclusions of this thesis are as follows:

1.  $\text{Na}_2\text{Ti}_6\text{O}_{13}$  is an extremely stable NIB anode capable of responding within 2 *min*. Storing sodium through a solid-solution mechanism, it was shown to experience negligible volume variation in the course of sodium storage. This fact is undoubtedly responsible for it demonstrating an ultra-long cycle life of 5,000 cycles with excellent efficiency. It was also shown to be very stable in the sodiated phase up to 500 °C, a fact that is important from a safety point of view. Furthermore, it exhibited a fairly low average voltage of 0.85 V vs Na/Na<sup>+</sup>. In a full NIB, this low voltage of anode resulted in a relatively high voltage battery when coupled with an appropriately high voltage cathode which could similarly cycle in a very stable manner with high efficiency for over 400 cycles with good retention. While its low capacity of 50 mAh/g would most probably preclude it from being used in batteries where the weight and size matter, it should not be a major factor for its utilization in



grid storage batteries. Its inexpensive and high yield synthesis described in this thesis is also a favourable quality which should help in decreasing costs.  $\text{Na}_2\text{Ti}_6\text{O}_{13}$  makes for an attractive grid storage NIB anode, especially for frequency regulation.

2. During deep discharge (up to 0.01 V vs Na/Na<sup>+</sup>),  $\text{Na}_2\text{Ti}_3\text{O}_7$  can store two moles of sodium per mole of  $\text{Na}_2\text{Ti}_3\text{O}_7$  (corresponding to a specific capacity of 178 mAh/g) at a very low average voltage of 0.3 V vs Na/Na<sup>+</sup>. However, it displayed inadequate cycling stability required for grid storage application. Furthermore, it showed a high polarization (> 0.2 V) which would limit its RTEE if utilized in a full NIB. Kinetic studies indicated a relatively high sodium chemical diffusion coefficient of  $3.48 \times 10^{-12} \text{ cm}^2/\text{s}$  which should translate to good high rate performance. In this regard, the morphology of the as-synthesized  $\text{Na}_2\text{Ti}_3\text{O}_7$  is important. It was demonstrated that sub-micrometric sized  $\text{Na}_2\text{Ti}_3\text{O}_7$  embedded within a conductive carbon matrix prepared by a novel solvothermal synthesis approach is capable of responding at 40 C rates (1.5 min response). However, it still displayed poor capacity retention which is believed to arise due to the instability of the deep discharged material ( $\text{Na}_4\text{Ti}_3\text{O}_7$ ), a fact that may limit the potential use of the  $\text{Na}_2\text{Ti}_3\text{O}_7 \rightleftharpoons \text{Na}_4\text{Ti}_3\text{O}_7$  sodium storage pathway in a NIB.
3. An intermediate phase has been discovered and isolated in the galvanostatic cycling of  $\text{Na}_2\text{Ti}_3\text{O}_7$  in a sodium battery. This new anode reaction for  $\text{Na}_2\text{Ti}_3\text{O}_7$  results in it storing sodium via a two-phase reaction mechanism between the phases  $\text{Na}_2\text{Ti}_3\text{O}_7 \rightleftharpoons \text{Na}_{3-x}\text{Ti}_3\text{O}_7$ . *Ex-situ* XRD analysis revealed that  $\text{Na}_2\text{Ti}_3\text{O}_7$  undergoes two separate two-phase reactions in its very first discharge which results in two separate discharge plateaus separated by a faint voltage step. The lower discharge plateau causes an irreversible transformation which leads to the loss of the  $\text{Na}_2\text{Ti}_3\text{O}_7 \rightleftharpoons \text{Na}_{3-x}\text{Ti}_3\text{O}_7$  sodium storage pathway in subsequent cycles. If this is avoided by restricting the

voltage window, then the  $\text{Na}_2\text{Ti}_3\text{O}_7 \rightleftharpoons \text{Na}_{3-x}\text{Ti}_3\text{O}_7$  pathway may display lesser capacity ( $\approx 89 \text{ mAh/g}$ ) compared to the conventional  $\text{Na}_2\text{Ti}_3\text{O}_7 \rightleftharpoons \text{Na}_4\text{Ti}_3\text{O}_7$  pathway, however, it demonstrates tremendous improvements in all other performance metrics. Firstly, the charge profile exhibited a flat plateau at  $0.2 \text{ V vs Na/Na}^+$ . This is the lowest reported redox voltage for any non-carbon based NIB anode. Secondly, the polarization of this pathway was found to be negligible. Thirdly, it was very stable in the sodiated state till a relatively safe temperature of  $376 \text{ }^\circ\text{C}$ . Fourthly, its cycle life was drastically improved to 1,500 cycles, in comparison to the  $\sim 100$  cycle life for the  $\text{Na}_2\text{Ti}_3\text{O}_7 \rightleftharpoons \text{Na}_4\text{Ti}_3\text{O}_7$  sodium storage pathway. Lastly, it demonstrated excellent high rate performance with stable cycling even up to  $80 \text{ C}$  ( $45 \text{ s}$  response). At all rates, the charge plateau was witnessed which is very advantageous as it would promote high energy and power densities in a NIB even at high rates.

4. Utilizing the  $\text{Na}_2\text{Ti}_3\text{O}_7 \rightleftharpoons \text{Na}_{3-x}\text{Ti}_3\text{O}_7$  sodium storage pathway, a high voltage NIB was fabricated demonstrating its discharge plateau between  $4.0 - 3.7 \text{ V}$ , which is the highest reported value for any non-carbon based NIB. Such an NIB displayed a stable energy density of around  $85 \text{ Wh/kg}$ , with this value increasing to  $130 \text{ Wh/kg}$  if the first cycle ICL of  $\text{Na}_2\text{Ti}_3\text{O}_7$  is eliminated by pre-cycling the anode prior to full cell testing. Furthermore, this NIB delivered excellent performance at high rates owing to the extremely low voltage plateau of the pathway. Hence, this  $\text{Na}_2\text{Ti}_3\text{O}_7 \rightleftharpoons \text{Na}_{3-x}\text{Ti}_3\text{O}_7$  sodium storage pathway has tremendous potential as a high energy and power density grid storage NIB anode. Its utilization in both frequency regulation and load levelling could be feasible, making it potentially an all-purpose anode material for grid storage NIBs. Moreover, if its first cycle  $\text{CE}_{\text{ff}}$  can be increased to near  $100 \%$  (through appropriately modifying the SEI formed on it or by discovering alternate electrolytes which do not decompose at highly

reducing potentials), then this pathway could even be used in electric vehicles owing to the expected high energy and power density of a NIB incorporating it if paired with an appropriate cathode.

5. The unique voltage step observed when cycling flat voltage electrode materials such as  $\text{NaTi}_2(\text{PO}_4)_3$ ,  $\text{Na}_2\text{Ti}_3\text{O}_7$  and  $\text{Na}_3\text{V}_2(\text{PO}_4)_3$  in a sodium battery during discharge at high rates but not at low rates, and not during the corresponding charge profiles, was found to be caused by electrolyte interaction with the Na CE. Surprisingly, this voltage step phenomenon only occurred in electrolyte solutions comprised of EC:PC solvent, but was not witnessed if the solvent was just PC. With a three-electrode arrangement, it was discovered that such a misleading phenomenon occurred due to an increase in the polarization of the Na CE during discharge. Such effects were shown to not arise at all due to the WE. Furthermore, the phenomenon was not witnessed in full sodium-ion cells indicating that the presence of EC:PC solutions as well as Na metal acting as the CE are essential towards witnessing the voltage step. The Na CE is evidently covered with passivation layer(s) when placed in alkyl carbonate solutions and it is this passivation layer(s) that is responsible for the observed phenomenon. A new physical and chemical explanation needs to be developed to understand it.
6. Sodium metal may be a good RE but it is not a good CE. Apart from the voltage step phenomenon that it can cause, the Na CE's polarization increases by a huge factor as the  $C$  rate of cycling (*i.e.* the current density it experiences) increases such that its voltage is not close to 0.0 V vs Na/Na<sup>+</sup> at high rates as one might expect. For example, during cycling at 10  $C$  for  $\text{NaTi}_2(\text{PO}_4)_3$  or  $\text{Na}_2\text{Ti}_3\text{O}_7$  as WE, the Na CE may operate as high as 0.20 V vs Na/Na<sup>+</sup> or perhaps even higher. Hence, if a researcher is evaluating the performance of a low voltage anode whose discharge plateau lies below 0.2 V (such as  $\text{Na}_2\text{Ti}_3\text{O}_7$ ) in a traditional half cell approach, then at high  $C$  rates, the

increased polarization of the Na CE would cause the cycling to reach the stated cut-off voltage (such as 0.01 V) prematurely. It is premature as the WE did not reach 0.01 V, only the WE-CE reached 0.01 V; if sodium was never inserted into  $\text{Na}_2\text{Ti}_3\text{O}_7$  in the first place, its charge capacity would be correspondingly lower. This is erroneous as the same electrode material would perform much better in a full NIB at high rates, hence, the stated goal of accurately evaluating the electrode material's sodium storage performance by utilizing a half cell approach would not be achieved. It should be mentioned that such results seem to be unique to sodium batteries as such drastic increased polarization of Li CE in lithium batteries is not seen. These results highlight the importance of using a three-electrode cell while evaluating the sodium storage performance of electrode materials, as Na is a good RE but not a good CE.

## 6.2 Future Research Directions

Based on the conclusions drawn from this thesis, some future research directions can be outlined. These are as follows:

1. Resolve the crystal structure of  $\text{Na}_{3-x}\text{Ti}_3\text{O}_7$  through Rietveld refinement of *in-situ* synchrotron XRD data. This knowledge would be helpful in understanding how much sodium is present in the newly discovered phase  $\text{Na}_{3-x}\text{Ti}_3\text{O}_7$  and hence, what is the theoretical capacity of this  $\text{Na}_2\text{Ti}_3\text{O}_7 \rightleftharpoons \text{Na}_{3-x}\text{Ti}_3\text{O}_7$  pathway. Accurate knowledge of its crystal structure will also help in analyzing the sodium migration routes present in  $\text{Na}_{3-x}\text{Ti}_3\text{O}_7$  (acquired through atomistic simulation studies on the resolved crystal structure) which would provide an answer as to why this pathway demonstrates such minimal polarization with regards to the  $\text{Na}_2\text{Ti}_3\text{O}_7 \rightleftharpoons$

$\text{Na}_4\text{Ti}_3\text{O}_7$  pathway. The resolved crystal structure will also reveal the volume change experienced by  $\text{Na}_2\text{Ti}_3\text{O}_7$  in going to  $\text{Na}_{3-x}\text{Ti}_3\text{O}_7$  which would help in understanding the good cycle life displayed by this pathway.

2. A key component for achieving long cycle life in low voltage anodes is the stability of the SEI. Hence, there is much scope for engineering a stable SEI through appropriate selections of binder/electrolyte/electrolyte additives. Some efforts were undertaken in this thesis already (use of CMC as a binder), however, more progress would be needed.
3. To obtain high energy densities in full NIBs, the anode should ideally display no first cycle ICL. If it does display a large first cycle ICL, much more cathode may be needed to supply the excess sodium, decreasing the energy density of a full NIB. For low voltage anodes such as  $\text{Na}_2\text{Ti}_6\text{O}_{13}$  and  $\text{Na}_2\text{Ti}_3\text{O}_7$ , this would be a challenge as the ICL is not caused by any fault of the actual anode material; it is due to electrolyte decomposition at highly reducing voltages to form a stable SEI thus allowing further cycling. Hence, different strategies should be explored to reduce this ICL as much as possible. Again, the type of binder may be quite important to minimize SEI as CMC has already shown to almost halve the first cycle ICL in the  $\text{Na}_2\text{Ti}_3\text{O}_7 \rightleftharpoons \text{Na}_{3-x}\text{Ti}_3\text{O}_7$  pathway with respect to the use of the traditional binder PVDF. Since SEI formation requires electron conduction from the electrode into the electrolyte solution, engineering strategies which prevent this from taking place, such as by coating the electrode with an electronic insulator yet sodium ion conductor, may prove useful.
4.  $\text{Na}_2\text{Ti}_6\text{O}_{13}$  has been demonstrated to function very well and in a reliable fashion in lab-scale NIBs. Hence, it would be desirable to attempt constructing industry-sized NIBs (the so called “18650” batteries) with  $\text{Na}_2\text{Ti}_6\text{O}_{13}$  as the anode as a proof-of-concept to see if its performance at the 18650 level is as reliable as that observed at the coin-cell level.

5. If the above endeavour is successful, then it would be desirable to conduct a thorough safety evaluation of such 18650 NIBs using  $\text{Na}_2\text{Ti}_6\text{O}_{13}$  utilizing various techniques the industry uses for evaluating batteries meant for the market. In this regard, thermal studies would also need to be conducted. If the outcome of all these studies indicates that  $\text{Na}_2\text{Ti}_6\text{O}_{13}$  is indeed as safe at the 18650 level as it is at the lab-scale, then, it could be ready to enter the market as a serious contender for frequency regulation grid storage NIB anode.

## References

1. IPCC, *Climate Change 2013: The Physical Science Basis. Contribution of Working Group I to the Fifth Assessment Report of the Intergovernmental Panel on Climate Change*, Cambridge University Press, Cambridge, United Kingdom and New York, NY, USA, 2013.
2. B. Dunn, H. Kamath and J.-M. Tarascon, *Science*, 2011, 334, 928-935.
3. Z. Yang, J. Zhang, M. C. W. Kintner-Meyer, X. Lu, D. Choi, J. P. Lemmon and J. Liu, *Chem. Rev.*, 2011, 111, 3577-3613.
4. D. Larcher and J. M. Tarascon, *Nat Chem*, 2015, 7, 19-29.
5. H. Vikström, S. Davidsson and M. Höök, *Applied Energy*, 2013, 110, 252-266.
6. N. Yabuuchi, K. Kubota, M. Dahbi and S. Komaba, *Chem. Rev.*, 2014, 114, 11636-11682.
7. R. Huggins, *Advanced batteries: materials science aspects*, Springer, 2008.
8. A. R. West, *Solid State Chemistry and its Applications*, John Wiley & Sons, 1984.
9. L. David and B. R. Thomas, *Handbook of batteries*, McGraw-Hill, Third edn., 2001.
10. S.-W. Kim, D.-H. Seo, X. Ma, G. Ceder and K. Kang, *Adv. Energy Mater.*, 2012, 2, 710-721.
11. V. Palomares, P. Serras, I. Villaluenga, K. B. Hueso, J. Carretero-Gonzalez and T. Rojo, *Energy Environ. Sci.*, 2012, 5, 5884-5901.
12. R. A. Shakoor, D.-H. Seo, H. Kim, Y.-U. Park, J. Kim, S.-W. Kim, H. Gwon, S. Lee and K. Kang, *J. Mater. Chem.*, 2012, 22, 20535-20541.
13. K. Chihara, A. Kitajou, I. D. Gocheva, S. Okada and J.-i. Yamaki, *J. Power Sources*, 2013, 227, 80-85.
14. M. Bianchini, N. Brisset, F. Fauth, F. Weill, E. Elkaim, E. Suard, C. Masquelier and L. Croguennec, *Chem. Mater.*, 2014, 26, 4238-4247.
15. K. Saravanan, C. W. Mason, A. Rudola, K. H. Wong and P. Balaya, *Adv. Energy Mater.*, 2013, 3, 444-450.
16. P. Barpanda, G. Oyama, S.-i. Nishimura, S.-C. Chung and A. Yamada, *Nat. Commun.*, 2014, 5.
17. L. Wang, J. Song, R. Qiao, L. A. Wray, M. A. Hossain, Y.-D. Chuang, W. Yang, Y. Lu, D. Evans, J.-J. Lee, S. Vail, X. Zhao, M. Nishijima, S. Kakimoto and J. B. Goodenough, *J. Am. Chem. Soc.*, 2015, 137, 2548-2554.
18. J. Song, L. Wang, Y. Lu, J. Liu, B. Guo, P. Xiao, J.-J. Lee, X.-Q. Yang, G. Henkelman and J. B. Goodenough, *J. Am. Chem. Soc.*, 2015, 137, 2658-2664.
19. N. Yabuuchi, M. Kajiyama, J. Iwatate, H. Nishikawa, S. Hitomi, R. Okuyama, R. Usui, Y. Yamada and S. Komaba, *Nat. Mater.*, 2012, 11, 512-517.
20. Y.-U. Park, D.-H. Seo, H.-S. Kwon, B. Kim, J. Kim, H. Kim, I. Kim, H.-I. Yoo and K. Kang, *J. Am. Chem. Soc.*, 2013, 135, 13870-13878.
21. M. Dahbi, N. Yabuuchi, K. Kubota, K. Tokiwa and S. Komaba, *Phys. Chem. Chem. Phys.*, 2014, 16, 15007-15028.
22. A. Ponrouch, D. Monti, A. Boschini, B. Steen, P. Johansson and M. R. Palacin, *J. Mater. Chem. A*, 2015, 3, 22-42.
23. A. Darwiche, C. Marino, M. T. Sougrati, B. Fraise, L. Stievano and L. Monconduit, *J. Am. Chem. Soc.*, 2012, 134, 20805-20811.
24. J. Qian, X. Wu, Y. Cao, X. Ai and H. Yang, *Angew. Chem.*, 2013, 125, 4731-4734.
25. J. Park, J.-S. Kim, J.-W. Park, T.-H. Nam, K.-W. Kim, J.-H. Ahn, G. Wang and H.-J. Ahn, *Electrochimica Acta*, 2013, 92, 427-432.

26. A. Abouimrane, W. Weng, H. Eltayeb, Y. Cui, J. Niklas, O. Poluektov and K. Amine, *Energy Environ. Sci.*, 2012, 5, 9632-9638.
27. Y. Park, D.-S. Shin, S. H. Woo, N. S. Choi, K. H. Shin, S. M. Oh, K. T. Lee and S. Y. Hong, *Adv. Mater.*, 2012, 24, 3562-3567.
28. M. Doeff, J. Cabana and M. Shirpour, *J. Inorg. Organomet. Polym.*, 2014, 24, 5-14.
29. S. Komaba, W. Murata, T. Ishikawa, N. Yabuuchi, T. Ozeki, T. Nakayama, A. Ogata, K. Gotoh and K. Fujiwara, *Adv. Funct. Mater.*, 2011, 21, 3859-3867.
30. A. Ponrouch, E. Marchante, M. Courty, J.-M. Tarascon and M. R. Palacin, *Energy Environ. Sci.*, 2012, 5, 8572-8583.
31. X. Xia, M. N. Obrovac and J. R. Dahn, *Electrochem. Solid-State Lett.*, 2011, 14, A130-A133.
32. C. Delmas, F. Cherkaoui, A. Nadiri and P. Hagenmuller, *Mater. Res. Bull.*, 1987, 22, 631-639.
33. Y. Sun, L. Zhao, H. Pan, X. Lu, L. Gu, Y.-S. Hu, H. Li, M. Armand, Y. Ikuhara, L. Chen and X. Huang, *Nat. Commun.*, 2013, 4, 1870.
34. K.-T. Kim, G. Ali, K. Y. Chung, C. S. Yoon, H. Yashiro, Y.-K. Sun, J. Lu, K. Amine and S.-T. Myung, *Nano Lett.*, 2014, 14, 416-422.
35. H. Xiong, M. D. Slater, M. Balasubramanian, C. S. Johnson and T. Rajh, *J. Phys. Chem. Lett.*, 2011, 2, 2560-2565.
36. J. C. Perez-Flores, C. Baehtz, A. Kuhn and F. Garcia-Alvarado, *J. Mater. Chem. A*, 2014, 2, 1825-1833.
37. M. Shirpour, J. Cabana and M. Doeff, *Chem. Mater.*, 2014, 26, 2502-2512.
38. M. Shirpour, J. Cabana and M. Doeff, *Energy Environ. Sci.*, 2013, 6, 2538-2547.
39. Y. Wang, X. Yu, S. Xu, J. Bai, R. Xiao, Y.-S. Hu, H. Li, X.-Q. Yang, L. Chen and X. Huang, *Nat. Commun.*, 2013, 4.
40. H. Yu, Y. Ren, D. Xiao, S. Guo, Y. Zhu, Y. Qian, L. Gu and H. Zhou, *Angew. Chem.*, 2014, 126, 9109-9115.
41. M. A. Muñoz-Márquez, M. Zarrabeitia, E. Castillo-Martínez, A. Eguía-Barrio, T. Rojo and M. Casas-Cabanas, *ACS Appl. Mater. Interfaces*, 2015, 7, 7801-7808.
42. L. Bodenes, A. Darwiche, L. Monconduit and H. Martinez, *J. Power Sources*, 2015, 273, 14-24.
43. B. Philippe, M. Valvo, F. Lindgren, H. Rensmo and K. Edström, *Chem. Mater.*, 2014, 26, 5028-5041.
44. J. Xu, C. Ma, M. Balasubramanian and Y. S. Meng, *Chem. Commun.*, 2014, 50, 12564-12567.
45. S. Andersson and A. D. Wadsley, *Acta Crystallographica*, 1962, 15, 194-201.
46. J. C. Perez-Flores, F. Garcia-Alvarado, M. Hoelzel, I. Sobrados, J. Sanz and A. Kuhn, *Dalton Trans.*, 2012, 41, 14633-14642.
47. R. Dominko, E. Baudrin, P. Umek, D. Arčon, M. Gaberšček and J. Jamnik, *Electrochem. Commun.*, 2006, 8, 673-677.
48. N. D. Trinh, O. Crosnier, S. B. Schougaard and T. Brousse, *ECS Trans.*, 2011, 35, 91-98.
49. J. C. Pérez-Flores, A. Kuhn and F. García-Alvarado, *J. Power Sources*, 2011, 196, 1378-1385.
50. J. Sangster, *J. Phase Equilib. Diffus.*, 2007, 28, 571-579.
51. S. Andersson and A. D. Wadsley, *Acta Crystallogr.*, 1961, 14, 1245.
52. Y. An, Z. Li, H. Xiang, Y. Huang and J. Shen, *Cent. Eur. J. Phys.*, 2011, 9, 1488-1492.
53. K. Chiba, N. Kijima, Y. Takahashi, Y. Idemoto and J. Akimoto, *Solid State Ionics*, 2008, 178, 1725-1730.



54. C.-Y. Xu, J. Wu, P. Zhang, S.-P. Hu, J.-X. Cui, Z.-Q. Wang, Y.-D. Huang and L. Zhen, *CrystEngComm*, 2013, 15, 3448-3454.
55. Z. Zhang, J. B. M. Goodall, S. Brown, L. Karlsson, R. J. H. Clark, J. L. Hutchison, I. U. Rehman and J. A. Darr, *Dalton Trans.*, 2010, 39.
56. D. Yang, H. Liu, Z. Zheng, S. Sarina and H. Zhu, *Nanoscale*, 2013, 5, 2232-2242.
57. P. Senguttuvan, G. I. Rousse, V. Seznec, J.-M. Tarascon and M. R. Palacín, *Chem. Mater.*, 2011, 23, 4109-4111.
58. G. Rousse, M. E. Arroyo-de Dompablo, P. Senguttuvan, A. Ponrouch, J.-M. Tarascon and M. R. Palacín, *Chem. Mater.*, 2013, 25, 4946-4956.
59. H. Pan, X. Lu, X. Yu, Y.-S. Hu, H. Li, X.-Q. Yang and L. Chen, *Adv. Energy Mater.*, 2013, 3, 1186-1194.
60. Y. Zhang, L. Guo and S. Yang, *Chem. Commun.*, 2014, 50, 14029-14032.
61. W. Wang, C. Yu, Y. Liu, J. Hou, H. Zhu and S. Jiao, *RSC Adv.*, 2013, 3, 1041-1044.
62. W. Zou, J. Li, Q. Deng, J. Xue, X. Dai, A. Zhou and J. Li, *Solid State Ionics*, 2014, 262, 192-196.
63. H.-H. Ou and S.-L. Lo, *Separation and Purification Technology*, 2007, 58, 179-191.
64. Y. Guo, N.-H. Lee, H.-J. Oh, C.-R. Yoon, K.-S. Park, H.-G. Lee, K.-S. Lee and S.-J. Kim, *Nanotechnology*, 2007, 18, 295608.
65. W. Wang, C. Yu, Z. Lin, J. Hou, H. Zhu and S. Jiao, *Nanoscale*, 2013, 5, 594-599.
66. K. Saravanan, K. Ananthanarayanan and P. Balaya, *Energy Environ. Sci.*, 2010, 3, 939-948.
67. H. Song, H. Jiang, T. Liu, X. Liu and G. Meng, *Mater. Res. Bull.*, 2007, 42, 334-344.
68. S. Mathur, R. Vyas, R. Jain, P. Kumar, K. Sachdev and S. K. Sharma, *J. Non-Cryst. Solids*, 2011, 357, 3084-3087.
69. C. Sun, L. Liu, L. Qi, H. Li, H. Zhang, C. Li, F. Gao and L. Dong, *J. Colloid Interface Sci.*, 2011, 364, 288-297.
70. D. D. Sun and P. F. Lee, *Sep. Purif. Technol.*, 2011.
71. A. J. Du, D. D. Sun and J. O. Leckie, *J. Hazard. Mater.*, 2011, 187, 401-406.
72. A. Rudola, K. Saravanan, S. Devaraj, H. Gong and P. Balaya, *Chem. Commun.*, 2013, 49, 7451-7453.
73. M. Park, X. Zhang, M. Chung, G. B. Less and A. M. Sastry, *J. Power Sources*, 2010, 195, 7904-7929.
74. K. Tang, X. Yu, J. Sun, H. Li and X. Huang, *Electrochim. Acta*, 2011, 56, 4869-4875.
75. W. Weppner and R. A. Huggins, *J. Electrochem. Soc.*, 1977, 124, 1569-1578.
76. S. Upreti, N. A. Chernova, J. Xiao, J. K. Miller, O. V. Yakubovich, J. Cabana, C. P. Grey, V. L. Chevrier, G. Ceder, J. L. Musfeldt and M. S. Whittingham, *Chem. Mater.*, 2012, 24, 166-173.
77. R. A. Huggins, in *Advanced Batteries: Materials Science Aspects*, Springer, New York, 2009, ch. 2, p. 38.
78. Y. Cao, L. Xiao, W. Wang, D. Choi, Z. Nie, J. Yu, L. V. Saraf, Z. Yang and J. Liu, *Adv. Mater.*, 2011, 23, 3155-3160.
79. Y. H. Jung, C. H. Lim and D. K. Kim, *J. Mater. Chem. A*, 2013, 1, 11350-11354.
80. Z. Jian, L. Zhao, H. Pan, Y.-S. Hu, H. Li, W. Chen and L. Chen, *Electrochem. Commun.*, 2012, 14, 86-89.
81. S.-W. Kim, D.-H. Seo, X. Ma, G. Ceder and K. Kang, *Adv. Energy Mater.*, 2012, 2, 710-721.
82. Z. Jian, W. Han, X. Lu, H. Yang, Y.-S. Hu, J. Zhou, Z. Zhou, J. Li, W. Chen, D. Chen and L. Chen, *Adv. Energy Mater.*, 2013, 3, 156-160.

83. D. Aurbach, *J. Power Sources*, 2000, 89, 206-218.
84. D. Aurbach, M. D. Levi, E. Levi, H. Teller, B. Markovsky, G. Salitra, U. Heider and L. Heider, *Journal of The Electrochemical Society*, 1998, 145, 3024-3034.
85. J. Y. Song, H. H. Lee, Y. Y. Wang and C. C. Wan, *J. Power Sources*, 2002, 111, 255-267.
86. J. Hong, C. Wang and U. Kasavajjula, *J. Power Sources*, 2006, 162, 1289-1296.
87. M. J. Aragón, C. Vidal-Abarca, P. Lavela and J. L. Tirado, *J. Power Sources*, 2014, 252, 208-213.
88. A. Rudola, K. Saravanan, C. W. Mason and P. Balaya, *J. Mater. Chem. A*, 2013, 1, 2653-2662.
89. A. Rudola, D. Aurbach and P. Balaya, *Electrochem. Commun.*, 2014, 46, 56-59.
90. V. Palomares, M. Casas-Cabanas, E. Castillo-Martinez, M. H. Han and T. Rojo, *Energy Environ. Sci.*, 2013, 6, 2312-2337.
91. M. D. Levi and D. Aurbach, *J. Phys. Chem. B*, 1997, 101, 4630-4640.
92. J. Maier, *Physical chemistry of ionic materials: ions and electrons in solids*, John Wiley & Sons, 2004.
93. Y. Hu, W. Kong, Z. Wang, H. Li, X. Huang and L. Chen, *Electrochem. Solid-State Lett.*, 2004, 7, A442-A446.
94. M. Dahbi, T. Nakano, N. Yabuuchi, T. Ishikawa, K. Kubota, M. Fukunishi, S. Shibahara, J.-Y. Son, Y.-T. Cui, H. Oji and S. Komaba, *Electrochem. Commun.*, 2014, 44, 66-69.
95. T. D. Hatchard and M. N. Obrovac, *J. Electrochem. Soc.*, 2014, 161, A1748-A1752.